**Showcasing a review by Dr Hend Omar Mohamed and Prof. Pedro Castaño, Multiscale Reaction Engineering (MuRE), King Abdullah University of Science and Technology (KAUST), Saudi Arabia.**

MXene-based electrocatalysts for CO_2 reduction: advances, challenges, and perspectives

MXene-based electrocatalysts, with tunable surface terminations and abundant active sites, enable efficient CO_2 reduction by facilitating rapid electron transfer and stabilizing key intermediates for high Faradaic efficiencies and enhanced C_2^+ selectivity. This review provides mechanistic insights and structure–function correlations that guide the rational design of next-generation MXene catalysts for scalable CO_2 valorization and sustainable energy conversion.

Image reproduced by permission of Dr Hend Omar Mohamed and Prof. Pedro Castaño, King Abdullah University of Science and Technology (KAUST) from *Mater. Horiz*., 2025, **12**, 7648.

As featured in:
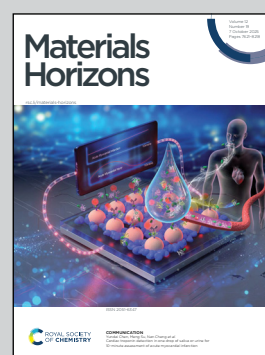
See Pedro Castaño,
Hend Omar Mohamed *et al*.,
Mater. Horiz., 2025, **12**, 7648.

ROYAL SOCIETY
OF **CHEMISTRY**

rsc.li/materials-horizons

Check for updates

MXene-based electrocatalysts for CO$_2$ reduction: advances, challenges, and perspectives

Sawsan Abo Talas,†[a] Pewee D Kolubah,†[b] Rushana Khairova,[b] Manal Alqahtani,[c] Soliman I. El-Hout, [ID][d] Faisal M. Alissa, [ID][e] Jehad K. El-Demellawi,[ef] Pedro Castaño [ID] *[bg] and Hend Omar Mohamed*[b]

The electrochemical reduction of carbon dioxide (CO$_2$) is a crucial step toward a sustainable carbon economy, enabling the conversion of greenhouse gases into valuable fuels and chemicals. Among the emerging materials for this transformation, two-dimensional (2D) MXenes comprising transition-metal carbides, nitrides, and carbonitrides are notable due to their tunable surface chemistry and high conductivity. This review comprehensively analyzes recent advancements in MXene-based electrocatalysis for the CO$_2$ reduction reaction (RR) and explores the unique electronic properties of MXenes that drive their catalytic performance. Composition, surface terminations, defect engineering, and interfacial dynamics dictate activity and selectivity and are analyzed to contextualize the structure–function correlations. This work discusses state-of-the-art strategies to enhance the performance of MXene-based electrocatalysts, including compositional modifications, heteroatom doping, and heterostructure integration. Mechanistic insight into the CO$_2$RR is examined to pinpoint the advantages and challenges of MXenes in the overall reaction network. Finally, this work presents a forward-looking perspective, outlining challenges and emerging opportunities for MXenes in driving sustainable CO$_2$ electrocatalytic conversion technology.

Wider impact

This review discusses key advances in the application of MXene-based materials as electrocatalysts for CO$_2$ reduction, emphasizing their tunable surface chemistry, high conductivity, and structural robustness. This field has witnessed notable progress in understanding the role of composition, defect engineering, surface terminations, and heterostructure integration in tailoring catalytic performance and selectivity. These developments are of broad significance, as CO$_2$ electroreduction presents a direct link between greenhouse gas mitigation and renewable energy utilization, enabling the production of value-added chemicals and fuels under mild conditions. The study of MXenes intersects materials science, electrochemistry, and environmental engineering, making it of compelling interest for both fundamental research and industrial applications. As global energy and climate goals intensify, the demand for efficient, scalable, and sustainable catalytic platforms is set to rise. Insights from this review—especially those concerning the molecular-level mechanisms and synthetic strategies—will help guide the rational design of next-generation 2D catalysts with enhanced activity and stability. Ultimately, these contributions will influence the development of modular and deployable CO$_2$ utilization systems, shaping the future of materials science toward low-carbon technologies and circular economy models.

[a] *Department of Chemical Engineering, Faculty of Engineering, Minia University, Minia, 61111, Egypt*

[b] *Multiscale Reaction Engineering (MuRE), King Abdullah University of Science and Technology (KAUST), Thuwal, 23955-6900, Saudi Arabia. E-mail: pedro.castano@kaust.edu.sa, hend.mohamed@kaust.edu.sa*

[c] *Biological and Environmental Science and Engineering (BESE) Division, Water Desalination and Reuse Center, King Abdullah University of Science and Technology, Thuwal 23955-6900, Saudi Arabia*

[d] *Nanostructured Materials and Nanotechnology Department, Advanced Materials Institute, Central Metallurgical Research and Development Institute, CMRDI, P.O. Box 87, Helwan, 11421, Cairo, Egypt*

[e] *Saudi Aramco, EXPEC Advanced Research Center, P.O. Box 5000, Dhahran, 31311, Saudi Arabia*

[f] *Center of Excellence for Renewable Energy and Storage Technologies (CREST), King Abdullah University of Science and Technology (KAUST), Thuwal, 23955-6900, Saudi Arabia*

[g] *Chemical Engineering Program, Physical Science and Engineering (PSE) Division, King Abdullah University of Science and Technology (KAUST), Thuwal, 23955-6900, Saudi Arabia*

† These authors contributed equally.

1. Introduction

Energy and environmental sustainability is essential for the continuation of life on the planet and has recently risen to the forefront of global concerns.[1,2] The overutilization of natural resources, combined with unsustainable production and consumption practices such as fossil-fuel combustion, deforestation, and industrial processes, has led to extensive environmental degradation and the emergence of climate change *via* CO_2 emissions.[3–5]

Global energy consumption is projected to increase by about 80% by 2030, potentially driving CO_2 levels and associated warming even higher without proactive mitigation.[6] According to the Intergovernmental Panel on Climate Change (IPCC),

anthropogenic greenhouse gas emissions raised average surface temperatures by 1.1 °C above the pre-industrial levels from 2011 to 2020, with more severe impacts to follow without substantial emission reduction.[7] As shown in Fig. 1A, global temperatures have increased and are expected to continue rising throughout the lifespans of three representative generations born in 1950, 1980, and 2020. Projections indicate that, without proactive mitigation measures, global surface temperatures could rise by up to 4 °C by 2100, underscoring the urgent need for collective action across governments, industry, and society.

CO_2 capture, storage, and utilization (CCSU) strategies aim to mitigate these emissions by capturing CO_2 from major point sources (power plants, gas-processing facilities, and industrial sites) and purifying, compressing, and injecting it into deep
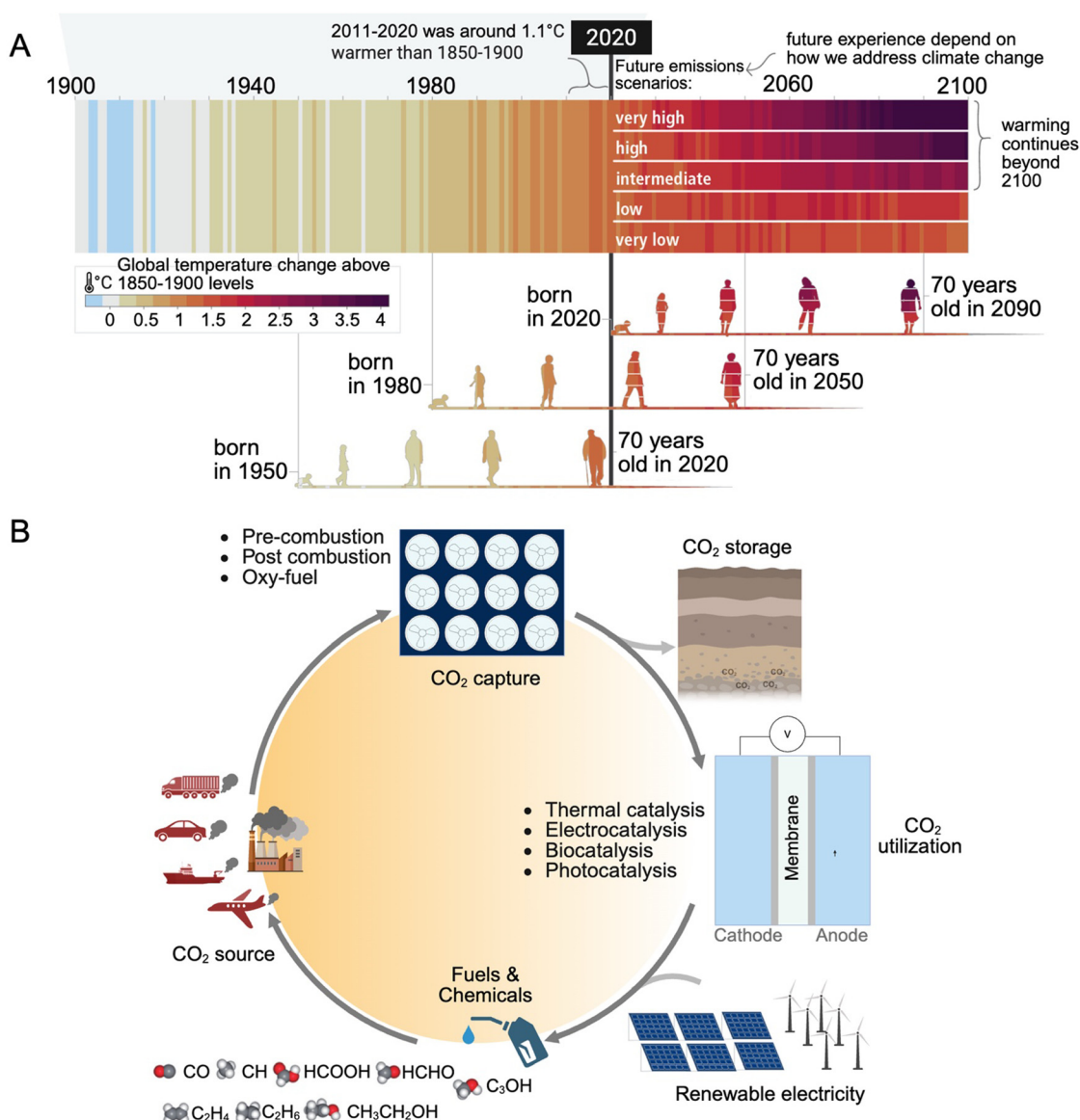

Fig. 1 Circular economy: (A) observed (1900–2020) and projected (2021–2100) changes in global surface temperature (relative to 1850–1900), which are linked to changes in climate conditions and effects, illustrating how the climate has already changed and will change along the lifespan of three representative generations (born in 1950, 1980 and 2020). Reproduced from ref. 7 with permission from IPCC, Copyright [2023]. (B) Schematic of CO_2 capture, storage, and utilization for fuel and chemical production.

geological formations (depleted reservoirs, saline aquifers, and coal seams) for long-term sequestration. The choice of capture method (pre-combustion, post-combustion, or oxy-fuel combustion) depends on the CO_2 concentration, required purity, and pressure of the emission stream. Those strategies are considered vital tools to reduce global CO_2 emissions by up to 32% by 2050 (Fig. 1B).[8–15] The CCS provides the CO_2 feedstock for utilization pathways, enhanced oil recovery, construction materials, chemical and fuel synthesis, and agricultural applications, creating value and supporting a circular-carbon economy.[16] However, the thermodynamic stability of CO_2 requires high energy input for the chemical activation and conversion of the O=C=O molecule into hydrocarbons, alcohols, or oxygenates.

Four primary catalytic approaches have been explored for CO_2 conversion: thermal, electrochemical, photocatalytic, and photothermal catalysis. In thermal catalysis, CO_2 is converted through high-temperature reactions such as hydrogenation and dry reforming with methane (CH_4), typically conducted at elevated pressures and under above-atmospheric conditions.[17] Photocatalysis mimics natural photosynthesis, using solar energy to generate electron–hole pairs that migrate to the catalyst surface and drive redox reactions with adsorbed CO_2 species.[18] Photothermal catalysis combines photochemical and thermochemical pathways to enhance reaction rates. This approach operates at lower temperatures than conventional thermal methods by harnessing the synergistic effects of semiconductor excitation and localized heating induced by plasmonic or nonplasmonic nanostructures.[19,20]

Among these approaches, electrocatalysis offers a uniquely advantageous route for CO_2 utilization by directly coupling with renewable electricity. Unlike thermal processes that depend on externally produced H_2 (e.g., via water electrolysis), the electrochemical CO_2 reduction reaction (CO_2RR) proceeds via a proton-coupled electron transfer (PCET) mechanism. This enables CO_2 conversion under mild operating conditions, typically at room or moderately elevated temperatures ($<100\ ^{\circ}C$) and ambient pressure, making it energy-efficient and scalable.[21] The CO_2RR can generate a wide range of high-value products, including carbon monoxide (CO), formic acid (HCOOH), ethylene (C_2H_4), ethanol (C_2H_6O), and propanol (C_3H_8O).[22] However, the competing hydrogen evolution reaction (HER), which reduces product selectivity by diverting electrons toward H_2 production, remains a key challenge.

Most of the CO_2RR products possess commercial relevance, and their selectivity can be tailored through rational design of the reaction environment, which involves optimizing electrolyte composition and reactor configuration, and, most critically, catalyst engineering.[23,24] By tuning catalyst morphology, elemental composition, exposed crystal facets, and defect structures, researchers aim to enhance catalytic activity, boost selectivity for specific products, and improve long-term durability.[25]

Despite rapid progress in the electrocatalytic CO_2RR, many conventional catalyst systems, such as transition metals, metal oxides, and carbides, suffer from low selectivity, poor product formation rates, and rapid deactivation.[26] As a result, significant research has focused on engineering more effective catalytic architectures, including alloy catalysts, metal–support hybrids, and heterostructures, that enhance CO_2 activation, suppress the competing HER, and improve stability.[27–29]

Recent years have seen a few breakthrough studies that define the current performance frontier for the CO_2RR. For instance, Wang et al.[30] developed a fluorine-modified copper (Cu) catalyst integrated into a flow-cell reactor, achieving an unprecedented current density of 1.6 A cm^{-2}, $>80\%$ C_2^+ faradaic efficiency (FE), and 16.5% single-pass yield under ambient conditions. The fluorine surface functionalization was shown to enhance water activation and stabilize key CHO intermediates, thus promoting C–C coupling and boosting multicarbon product selectivity. Sargent et al.[31] demonstrated that pairing a strong-acid electrolyte with an atomically sputtered planar Cu catalyst yields $>90\%$ C_2^+ FE, 78% single-pass CO_2 utilization, and 30% energy efficiency for C_2^+ products, with an exceptionally low energy cost of 249 GJ t^{-1} for ethanol production. While promising, the synthesis approach is complex and cost-intensive, posing scalability challenges. Yang et al.[32] achieved 97% CO selectivity at -0.5 V vs. RHE and a specific current of 350 A g^{-1} using nickel (Ni) single atoms supported on N, S-co-doped graphene. A 100 h durability test confirmed long-term operational stability, and DFT calculations revealed that the non-centrosymmetric ligand environment around Ni(I) significantly enhanced adsorption strength for CO_2 and key intermediates. These breakthroughs illustrate how combining precise atomic-level design, reactor integration, and advanced surface engineering can collectively overcome long-standing CO_2RR challenges. Yet despite such advances, broader challenges remain in scalability, cost, and long-term performance, motivating exploration of new catalyst platforms.

Among the most promising emerging materials are two-dimensional (2D) systems, including graphene, transition-metal dichalcogenides (TMDs), layered double hydroxides (LDHs),[23] and the newest class—MXenes. MXenes are a family of 2D transition-metal carbides, nitrides, or carbonitrides, known for their high electrical conductivity, tunable surface chemistry, excellent mechanical integrity, and abundant redox-active sites, making them particularly attractive for CO_2RR applications.[25,33–40] For instance, their metallic conductivity facilitates electron transport for complex proton-coupled electron transfer (PCET) steps. Surface terminations (e.g., –O, –OH, and –F) can be engineered to steer intermediate adsorption and reaction pathways, while their robustness supports long-term operation under electrochemical conditions. However, despite these promising features, most experimental MXene-based CO_2RR studies focus on $Ti_3C_2T_x$, due to the ease of synthesis and well-established chemistry.[41] This field remains in its early stages: over 80% of reported studies are theoretical, relying on quantum mechanical calculations to evaluate CO_2 binding, activation energies, and selectivity trends.[42] Experimental progress lags due to synthesis challenges, such as controlling etching, delamination, defect density, and surface terminations, affecting catalytic performance and reproducibility.

This review provides a comprehensive overview of recent progress in MXene-based catalysts for the CO_2RR. A brief
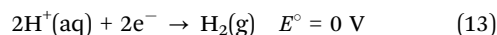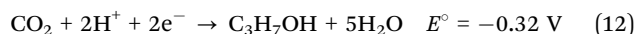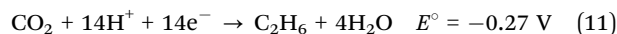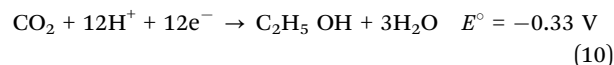
overview of the CO_2RR covers general reaction mechanisms, pathways for various product groups (*e.g.*, hydrocarbons, alcohol, and oxygenates), critical intermediates governing product formation, and the internal and external factors influencing the overall system architecture. Next, this work explores the distinctive chemical and structural properties of MXenes that enhance their catalytic potential for the CO_2RR, highlighting how they differ from conventional CO_2RR catalysts.

A critical assessment of recent developments in catalyst design and modification strategies follows, particularly on progress in operational parameters that significantly affect catalytic activity and selectivity. Then, this work explores the electrocatalytic mechanisms of the CO_2RR using MXene-based catalysts, highlighting how these mechanisms can be tailored to enhance CO_2 conversion efficiency and steer product selectivity, underscoring the novelty and promise of MXene-based catalysts. Additionally, critical factors affecting CO_2RR performance, including e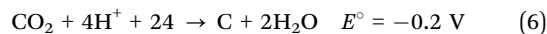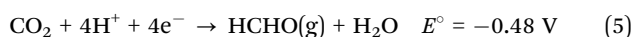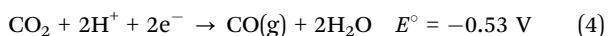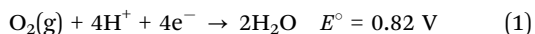lectronic properties, surface chemistry, and electrolyte interactions, are reviewed. Finally, this work provides a forward-looking perspective, emphasizing the necessity of a systematic approach to developing cost effective MXene-based catalysts for practical applications.

2. Fundamentals of CO_2 reduction

In a CO_2 electrolyzer, the anode and cathode reactions occur in separate chambers, divided by an ion-conducting membrane. The CO_2RR electrolyzers have distinct configurations, including H-cells, membrane electrode assembly (MEA), and microfluidic cells.[43] These reactor configurations have an anode and a cathode. At the anode, water is oxidized to produce molecular oxygen (O; eqn (1)), whereas at the cathode, CO_2 is reduced into C-containing species (Fig. 2a). An external energy input is required to drive the overall reaction. From a thermodynamic perspective, the potential required to drive the one-electron reduction of CO_2 to the CO radical is −1.9 V *vs.* the standard Hydrogen electrode (SHE) (eqn (2)), making the reaction highly energy-intensive and thermodynamically unfavorable in the absence of an appropriate catalyst.[44] The formation of CO_2RR products is influenced by the PCET process involving electron transfer ranging from 2 to 18 e^- per CO_2 molecule (eqn (3)–(12)).[45–47]

Although the proton-assisted process enables the formation of a wide range of products, achieving the selective production of the desired compounds remains a significant challenge due to the similar redox potentials of competing reaction pathways. Selectivity limitations are exacerbated in aqueous electrolyte-based CO_2 electrolyzers, where the HER occurs at a comparable potential (eqn (13)), directly competing with the CO_2RR:

$$O_2(g) + 4H^+ + 4e^- \rightarrow 2H_2O \quad E^\circ = 0.82 \text{ V} \quad (1)$$

$$CO_2 + e^- \rightarrow CO_2^{\bullet-} \quad E^\circ = -1.9 \text{ V} \quad (2)$$

$$CO_2 + 2H^+ + 2e^- \rightarrow HCOOH(aq) \quad E^\circ = -0.61 \text{ V} \quad (3)$$

$$CO_2 + 2H^+ + 2e^- \rightarrow CO(g) + 2H_2O \quad E^\circ = -0.53 \text{ V} \quad (4)$$

$$CO_2 + 4H^+ + 4e^- \rightarrow HCHO(g) + H_2O \quad E^\circ = -0.48 \text{ V} \quad (5)$$

$$CO_2 + 4H^+ + 24 \rightarrow C + 2H_2O \quad E^\circ = -0.2 \text{ V} \quad (6)$$

$$CO_2 + 6H^+ + 6e^- \rightarrow CH_3OH(aq) + H_2O \quad E^\circ = -0.38 \text{ V} \quad (7)$$

$$CO_2 + 8H^+ + 8e^- \rightarrow CH_4(g) + 2H_2O \quad E^\circ = -0.24 \text{ V} \quad (8)$$

$$CO_2 + 12H^+ + 12e^- \rightarrow C_2H_4 + 4H_2O \quad E^\circ = -0.34 \text{ V} \quad (9)$$

$$CO_2 + 12H^+ + 12e^- \rightarrow C_2H_5OH + 3H_2O \quad E^\circ = -0.33 \text{ V} \quad (10)$$

$$CO_2 + 14H^+ + 14e^- \rightarrow C_2H_6 + 4H_2O \quad E^\circ = -0.27 \text{ V} \quad (11)$$

$$CO_2 + 2H^+ + 2e^- \rightarrow C_3H_7OH + 5H_2O \quad E^\circ = -0.32 \text{ V} \quad (12)$$

$$2H^+(aq) + 2e^- \rightarrow H_2(g) \quad E^\circ = 0 \text{ V} \quad (13)$$
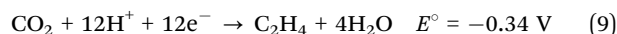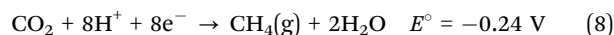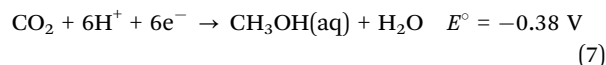
Depending on the available catalyst surface during the reaction, O_2 is activated and converted into intermediates. These intermediates transform into final products *via* distinct mechanistic pathways (Fig. 2B).[49] The paths are classified into C_1 products (CO, HCOOH, methanol (CH_3OH), and CH_4), C_2 products (C_2H_4 and C_2H_6O), and a C_3 product (C_3H_8O).[46,50,51] For instance, HCOOH formation includes the creation of an *OCHO intermediate *via* the activation and reduction of CO_2.[52] This step requires catalysts with high O affinity, such as p-block metals (*e.g.*, tin [Sn], bismuth [Bi], indium [In], and lead [Pb]), facilitating the reduction of *OCHO to form HCOOH.[53–57]

In contrast, producing CO involves two proton–electron steps that generate a *COOH intermediate. Catalysts (*e.g.*, gold [Au], silver [Ag], and zinc [Zn]) known for their lower affinities for O and H reduce *COOH to CO.[46] The selectivity of the overhead product in the aqueous CO_2RR can be explained by the ability of various catalyst surfaces to bind reaction intermediates, in which catalyst surface properties play a critical role in determining the reaction pathway and product selectivity (Fig. 2C).[58] Moreover, CO serves as a crucial intermediate for higher hydrocarbons and oxygenates, including formaldehyde (HCHO), CH_3OH, and CH_4, involving four, six, and eight electron transfer, respectively.[46] In addition, CO is widely considered an intermediate for forming C_2H_4 and C_2H_5OH. Table 1 shows the classification of value-added products and significant intermediates.

The formation of these C_{2+} products involves the dimerization of two CO molecules or the combination of CO with *CHO. Copper (Cu)-based catalysts are effective in these reactions because they facilitate C–C coupling, achieving high selectivity and activity for C_{2+} products.[59] In addition, Cu-based materials are among the most promising catalysts for CO_2 reduction because they exhibit relatively low activity toward the HER while demonstrating unique intrinsic catalytic activity for the CO_2RR, forming a wide range of hydrocarbons, alcohols, and oxygenates. Although the elemental composition of the CO_2RR catalyst is crucial in determining reaction pathways, the overall reaction mechanism is considerably influenced by several factors, including operating conditions, such as electrolyte pH and concentration, cation/anion size, applied potential, cell configuration, and catalyst surface characteristics (*e.g.*, facets,
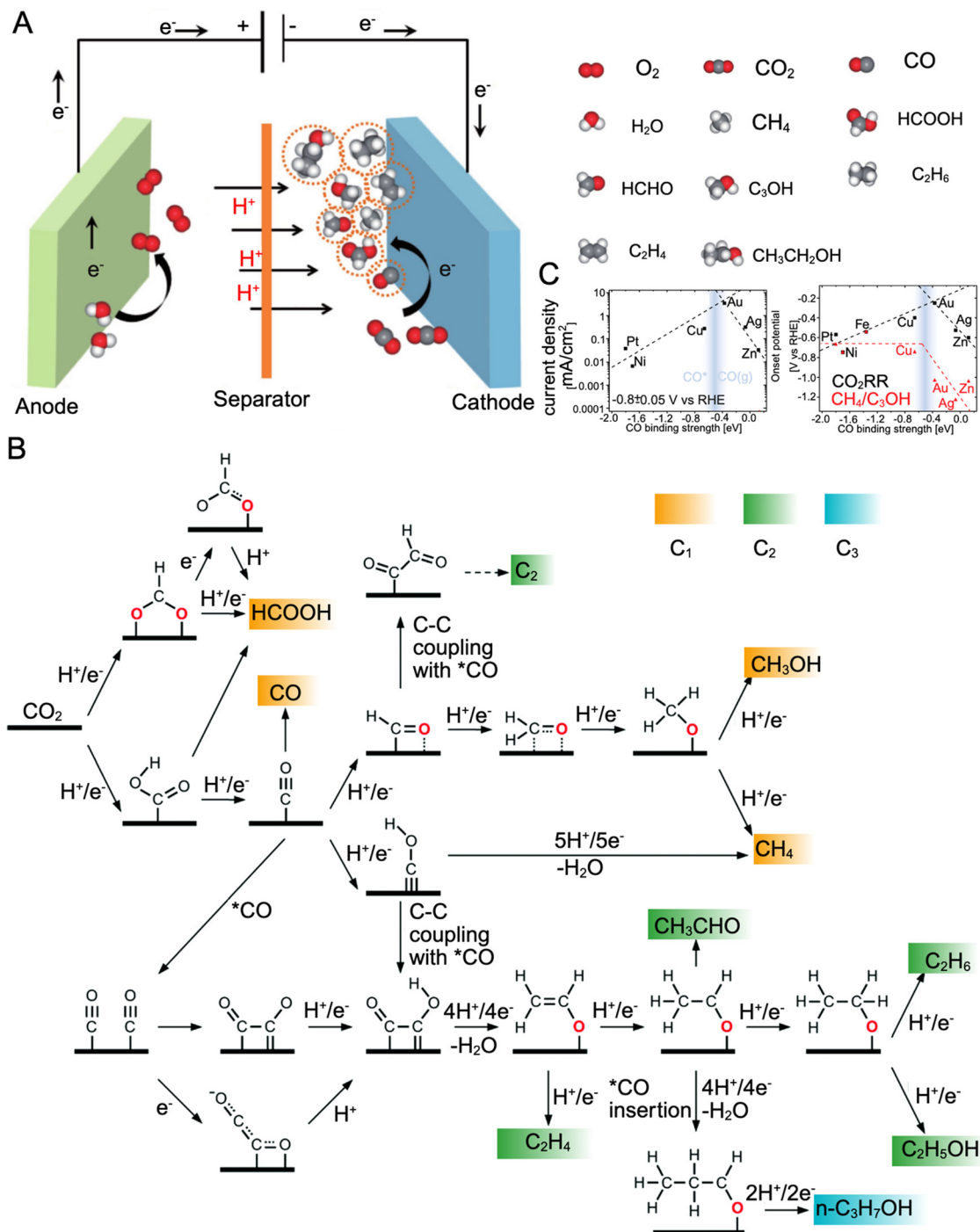
Fig. 2 (A) Schematic of the electrochemical CO_2 reduction reaction system. Reproduced from ref. 47, with permission from John Wiley and Sons, copyright [2017]. (B) Reaction mechanism, product distribution from CO_2 reduction (C1–C3). Reproduced from ref. 48, with permission from Royal Society of Chemistry, Copyright [2021]. (C) Left: volcano plot of the partial current density for the CO_2RR at 0.8 V *vs.* the CO binding strength. Right: two onset potentials plotted *vs.* CO binding energy, the overall CO_2RR, and the conversion of CO_2 to methane or methanol (Reprinted with permission from *Am. Chem. Soc.* 2014, 136, 40, 14107–14113. Copyright [2014] American Chemical Society).

defects, structure, morphology, and surface adsorbates).[60–63] These physical and chemical parameters strongly influence the thermodynamic adsorption energies of critical intermediates and the kinetic barriers of the reactions, leading to alternative reaction pathways. The following section examines the crucial factors influencing the CO_2RR mechanism in greater detail.

2.1. Factors affecting the CO_2 electroreduction process

The efficiency of the CO_2RR is governed by the interrelation of internal and external factors in the overall system architecture (Fig. 3A). Internal factors include the electrode configuration and electrolyte characteristics, whereas external factors include the applied potential and electrolyzer design. Significant

Table 1 Classification of value-added products and significant intermediates.[48]

	Products	Critical intermediates
Two-electron products	Formate ($HCOO^-$), formic acid (HCOOH)	*OCHO/HCOO*
	Carbon monoxide (CO)	*COOH
Deeply reduced C1 products	Methane (CH_4)	CH_3O*, *OH
	Methanol (CH_3OH)	CH_3O*, *OH
Multicarbon products	Ethylene (C_2H_4)	CH_2CHO*
	Acetaldehyde (CH_3CHO)	CH_2CHO*
	Ethanol (C_2H_5OH)	CH_2CHO*, CH_3CHO*, CH_3CH_2O*
	Ethane (C_2H_6)	CH_3CH_2O*
	n-Propanol (n-C_3H_7OH)	CH_3CHO*, CH_3CH_2O*

research has been focused on computational modeling and the experimental analysis of the electrode/electrolyte (E/E) interface to clarify electrochemical processes, such as reaction dynamics, product selectivity, and overall electrochemical performance.[64–66] The E/E interface is influenced by the constant potential during CO_2RR processes, inducing negative surface charges and promoting the formation of the electrical double layer (EDL),[67–69] as depicted in Fig. 3B.

The EDL comprises charged species and oriented dipoles, organized into three distinct layers: the inner Helmholtz plane (IHP), the outer Helmholtz plane, and the diffuse layer.[68] The IHP is closest to the electrode surface where the electrochemical reaction occurs, whereas cations gather in the outer Helmholtz plane region in response to the applied potential. According to the classical Gouy–Chapman–Stern model, the EDL and bulk electrolytes have a distinctly different composition. Therefore, they are considered two distinct phases separated by the diffuse layer.[70] Ions form the diffuse layer due to electrostatic repulsion and thermodynamic diffusion. The concentration of the diffuse layer decreases progressively outward toward the bulk electrolyte. In the electrochemical system, the species in the EDL are widely accepted to be in equilibrium with the bulk electrolyte in the absence of any faradaic processes.[67]

The CO_2RR is an inner-sphere process in the IHP involving adsorption and bond rearrangement of CO_2 and intermediates. When the CO_2 molecule adsorbs onto the electrode surface, it binds through chemisorption, a process involving electron redistribution and chemical bond formation.[71] The CO_2 binding process at the surface is influenced by the highest occupied and lowest unoccupied molecular orbitals. The orientation of these orbitals relative to the surface determines the nature of the binding. Such a CO_2-binding process on MXenes is expected to be effective due to the tunable surface chemistry. According to the computational investigations, their surface chemistry influences the diffusion and adsorption of species and metal ions on MXene surfaces.[72] Therefore, understanding the molecular-level interaction between CO_2 and MXenes at the E/E interface is crucial to evaluating intermediates' adsorption/
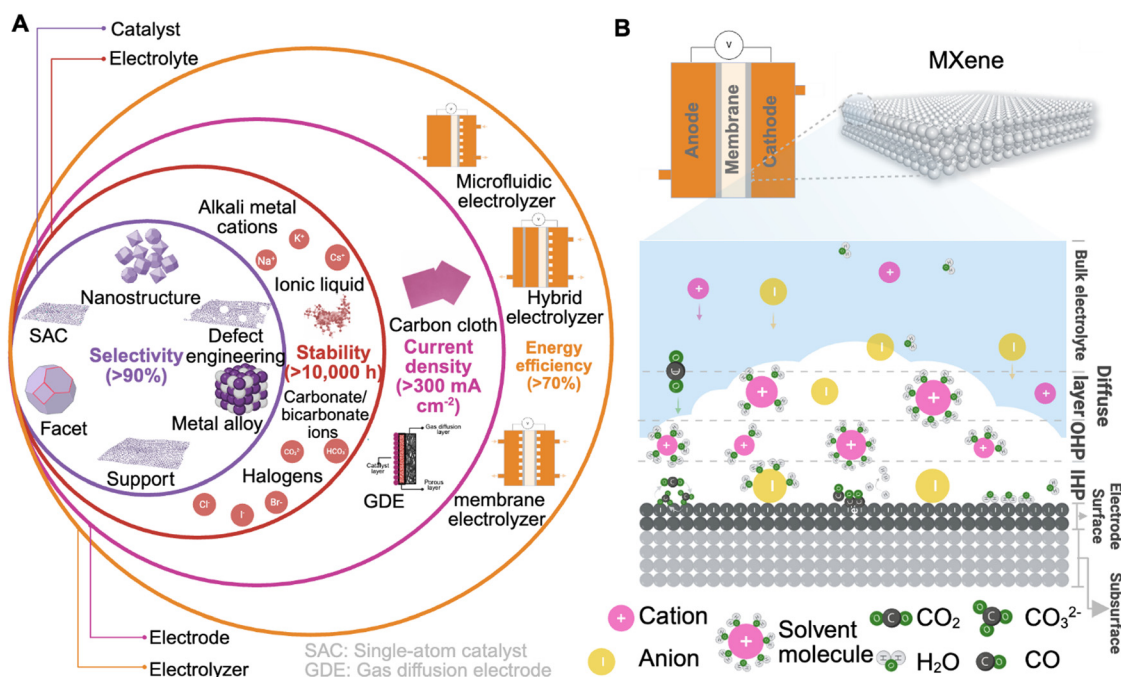

Fig. 3 (A) Factors affecting the CO_2 electroreduction process. (B) Schematic of the electrode–electrolyte interface for the CO_2RR, accounting for the electric double layer and bulk electrolyte.

desorption process, reaction kinetics, and dynamic behavior and designing highly active, selective, and durable catalysts.

Harris et al.[73] employed multinuclear magnetic resonance experiments to elucidate the strong H-bonded water molecule to the terminal hydroxyl (–OH) group on the MXene surface, providing key insights for estimating Gibbs free energy profiles and the reaction-limiting potential (U_L) of spontaneous electrochemical reactions.

Later, Cheng et al.[74] employed the density functional theory (DFT) to model EDL properties and proposed an intermediate electronic structure and reaction pathways of the CO_2RR on modified Nb_2CO_2 surfaces while considering the effect of water. The results indicated that pure Nb_2CO_2 is unsuitable as a catalyst for the CO_2RR; nonmetal-doped MXenes can lower the U_L of the CO_2RR and does not significantly change the reaction products. In contrast, MXene surface modification with TMs reduced the U_L of the CO_2RR and altered the reaction products. The V-modified Nb_2CO_2 system was identified as the most effective CO_2RR catalyst, favoring HCOOH as the primary product with a U_L of −0.11 V (Fig. 4A). The presence of d-levels in TMs provides a diverse range of electronic configurations, which can participate in bonding with CO_2 molecules, enhancing the electron transfer processes essential for the CO_2RR. The interaction between the d-levels of the metal and the π^* orbitals of CO_2 can lead to a more efficient electron transfer, which is crucial for breaking strong C=O bonds in CO_2.[75,76]

The EDL properties of MXenes modified by TMs as single-atom catalysts (SACs) have been extensively explored.[79–82] Li et al.[77] investigated the Mo_3C_2 MXene modified with a series of Group IVB, VB, and VIB TMs and explored the mechanism behind the breaking of linear scaling relationships between TMs and the adsorption energies of critical intermediates OCH_2O^* and $HOCH_2O^*$ (Fig. 4B). Their findings revealed that substituting TMs on the MXene surface induces an upshift in the d-band center of the molybdenum (Mo) layer surface, selectively tuning the adsorption strength of OCH_2O^* and $HOCH_2O^*$, further lowering U_L from −0.651 V for Mo_3C_2 to −0.350 V for Mo_2TiC_2 (Fig. 4C). The electron localization function analysis indicated the strong localization of lone electrons on the surface Mo layer upon TM substitution, enhancing its chemical activity due to electronic coupling between the valence states of adsorbates and the TM states, resulting in splitting the bonding and antibonding states (Fig. 4D). In addition, Mo_2TiC_2 demonstrated the highest conversion performance of CO_2 to CH_4 among the studied MXenes.

Although electrode properties play a crucial role, the E/E interface is significantly influenced by the electrolyte medium. Aqueous solutions, organic solvents, and ionic liquids (ILs) can stabilize the solid–electrolyte interphase, enhance CO_2 solubility, and facilitate efficient ionic transport, all essential for optimizing electrochemical reactions. Among these, aqueous $KHCO_3$ solutions (0.1 to 0.5 M) are widely employed to evaluate the performance of MXene-based catalysts due to their cost-effectiveness, nontoxicity, and buffering capacity, making them the preferred medium for CO_2RR investigations. A recent experimental study[83] demonstrated that the performance of $Ti_3C_2T_x$ on a glassy carbon electrode improved for mono- and multicarbon products, achieving selectivity toward CO (42.2%), CH_3OH (23.6%), C_2H_6O (20.1%), and acetone (10.1%) as the $KHCO_3$ concentration in the electrolyte increased from 0.1 to 0.5 M. The authors attributed this performance to the enhanced CO_2 adsorption capacity of 0.16 mmol g^{-1}, facilitating a higher current density.

Otgonbayar et al.[84] demonstrated enhanced selectivity toward alcohols, such as CH_3OH and C_2H_6O, using a 2D MXene coupled with cuprous oxide (Cu_2O)/magnetite (Fe_3O_4) nanocomposites using various electrolytes, including sodium carbonate (Na_2CO_3), potassium carbonate (K_2CO_3), potassium chloride (KCl), and sodium chloride (NaCl). A strong interaction between the catalyst surface and the electrolyte, particularly with alkali metals and halide ions (chlorine [Cl^-]), enabled faster adsorption/desorption dynamics, influencing their ability to donate or retain a negative charge. This interaction generated a dipole moment, modified the local surface environment, and enhanced the catalytic activity.

Qu et al.[85] demonstrated CO_2 electrolysis using seawater as the cost-effective electrolyte. This strategy achieved 92% faradaic efficiency (FE) for CO production using synthesized nitrogen (N)-doped Ti_3C_2 MXene nanosheets with abundant V_{Ti} defects. Mechanistic studies have revealed that N dopants and V_{Ti} synergistically modulate the electronic structure of the active titanium (Ti) site, significantly lowering the free energy barriers for *COOH formation and *CO desorption.

Notably, pH is pivotal in influencing aspects of PCET processes in the CO_2RR. The local pH at the E/E interface can change during the CO_2RR, significantly affecting the selectivity and activity of the catalyst.[86,87] For example, Varela et al.[88] investigated the influence of the electrolyte concentration and the importance of local pH in controlling the selectivity of the CO_2RR on Cu. The study demonstrated that the buffer capacity of the electrolyte is critical in influencing catalytic activity and product selectivity. In dilute $KHCO_3$, the lower proton concentration near the electrode surface suppresses the formation of H_2 and CH_4, whereas the production rates of CO and C_2H_4 remain largely unaffected.

Xie et al.[78] employed lateral-type in situ surface-enhanced Raman spectroscopy combined with computational simulations using COMSOL to investigate the effect of local pH variations at the E/E interface on CO_2RR selectivity and activity (Fig. 4E). The study revealed that, in the diffusion layer, the local pH gradually decreases as the distance from the catalyst surface increases, with a sharp pH drop indicating limited proton mass transport (Fig. 4F–H). As reported, these local pH variations are influenced by the buffering capacity of the electrolyte and can have a considerable influence on the selectivity of C_2^+ products during the CO_2RR (Fig. 4I).[89]

The pH dependence of CO_2 activation differs from that of the competing HER. For example, previous work has demonstrated that the overall product selectivity of graphite-immobilized coprotoporphyrin is highly pH sensitive. At a pH of 1, H_2 is the dominant product, whereas at a pH of 3, CO
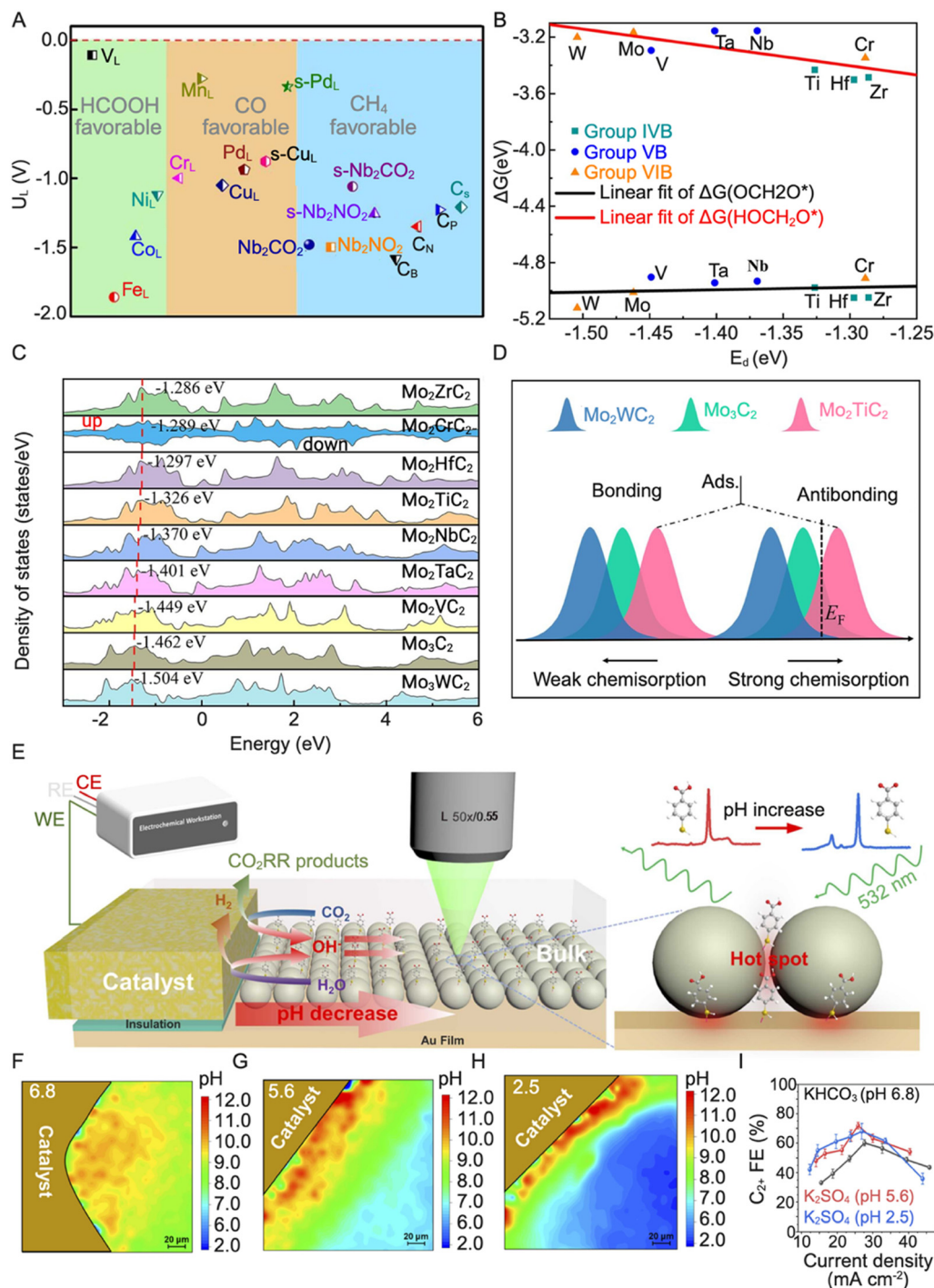
Fig. 4 (A) Potential limiting the U_L of NbCO$_2$ and modified Nb$_2$CO$_2$. Reproduced from ref. 74, with permission from Elsevier, Copyright [2021]. (B) Linear relation of adsorption free energy $\Delta G(OCH_2O^*)$ and $\Delta G(HOCH_2O^*)$ vs. the d-band center E_d. (C) Projected density of state plots for the d orbital of surface Mo atoms in MXenes, in which the Fermi level was set to 0, and the calculated d-band centers are denoted by dashed vertical red lines. (D) Schematic of the bond formation between the adsorbate (Ads.) and reaction surface of MXenes, represented by Mo$_2$WC$_2$, Mo$_3$C$_2$, and Mo$_2$TiC$_2$. (B)−(D) Reproduced from ref. 77, with permission from Elsevier, Copyright [2021]. (E) Schematic of the L-SERS system for in situ local pH measurement and illustration of pH-sensitive molecules (4-MBA) in the SERS. (F)−(H) Local pH images around the catalyst surface in CO$_2$-saturated electrolytes of (F) KHCO$_3$ (pH 6.8), (G) K$_2$SO$_4$ (pH 5.6), (H) K$_2$SO$_4$ (pH 2.5) with the applied current density of 10 mA cm^{-2}, and (I) C$_{2+}$ faradaic efficiency influenced by pH. (E)−(I), Reproduced from ref. 78 with permission from Elsevier, Copyright [2024].

becomes the primary product, illustrating the strong influence of pH on reaction pathways.[90] The DFT calculations indicate that the critical intermediate is anionic hydride, which

undergoes a nucleophilic attack on CO$_2$ to yield HCOO$^-$. The reaction is facilitated by potential-induced changes in the oxidation state of the catalyst, with the hydride typically

residing on the ligand for In and Sn porphyrins. The stability of the resulting species is vital for reactions leading to CO or HCOOH/HCOO⁻ formation.

Pourbaix diagrams, analogous to standard pressure–volume phase diagrams, offer insight into the thermodynamic equilibrium surface structure under varying pH and applied potential (U) conditions. According to the Pourbaix diagram of MXenes with various surface termination groups (Fig. 5),[91] MXenes do not exhibit a bare surface at any pH-U conditions in an aqueous environment. At a U value below −0.6 V, the MXene surface is fully hydrogenated, with all reaction sites occupied by H*. As U increases, the surface undergoes progressive oxidation, with OH* gradually replacing H*, highlighting the strong U sensitivity of the process. The intricate relationship between U and MXene functionalization, as demonstrated for other electrochemical reactions, such as the HER[92] and N reduction reaction,[93] is significant because it directly influences catalytic activity. This understanding can guide the design of MXene-based catalysts for the CO₂RR, facilitating the selection of optimal surface terminations for enhanced performance. Future studies should develop Pourbaix diagrams for MXene compositions under CO₂RR-relevant pH and U conditions, offering deeper insight into their electrochemical stability and reactivity.

The electrolyte's metal cation/anion composition is another critical factor influencing the product distribution of the CO₂RR. Alkaline–metal cations facilitate CO₂ adsorption in aqueous solutions and stabilize critical intermediates, such as COOH*, via noncovalent interactions with adsorbed species or a field effect.[94] For instance, Hori et al.[95] observed that C₂H₄ formation increased relative to CH₄ as the cation size increased (lithium [Li⁺] < sodium [Na⁺] < potassium [K⁺] < cesium [Cs⁺]).[96] This variation in hydrocarbon selectivity was attributed to differences in specific adsorption or the preferential hydrolysis of various cations. Among anions, halide ions (F⁻, Cl⁻, bromine [Br⁻], and iodine [I⁻]) could modulate the geometry and electronic structure of metal-based electrocatalysts, stabilize active species, regulate the adsorption and desorption of reaction intermediates, and reduce the overpotential to enhance the selectivity and activity of the CO₂RR for multi-carbon products.[97–99] This finding is attributed to halide ions donating electrons to the empty orbitals of CO₂.[100]

Ni et al.[101] synthesized fluorine (F)-doped caged porous C, achieving an FE of 88.3% for CO production at −1.0 V vs. RHE, with a corresponding current density of −37.5 mA cm⁻². The microporous structure of the F-doped C shells, particularly at edge positions, induces localized high electric fields, lowering the thermodynamic energy barrier for CO₂ reduction. Similarly,
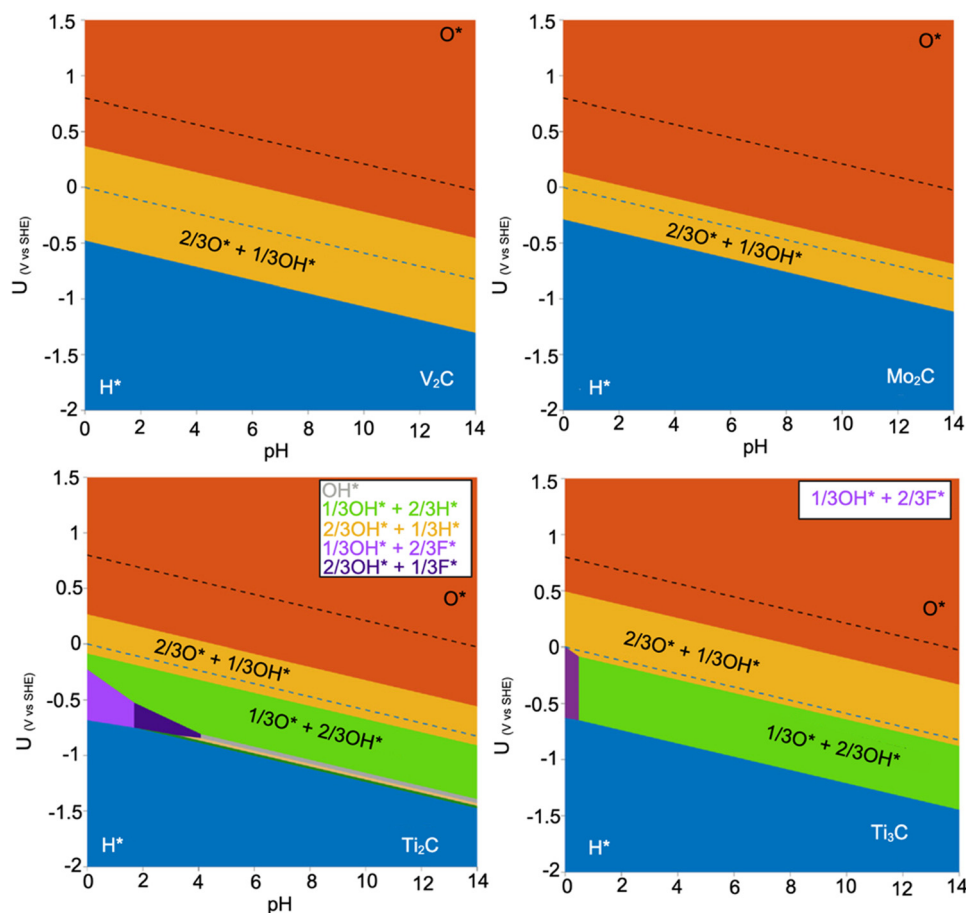

Fig. 5 Pourbaix diagrams of Mo₂C, V₂C, Ti₂C, and Ti₃C₂. Reproduced from ref. 91 with permission from Wiley and Sons, Copyright [2022].

Gao et al.[102] demonstrated that O_2-plasma-activated Cu catalysts, combined with electrolyte design, exhibited enhanced CO_2RR activity and selectivity toward multicarbon hydrocarbons and alcohols, achieving a FE of $\sim69\%$ and a partial current density of -45.5 mA cm^{-2} for C_{2+} products at -1.0 V vs. RHE. Their findings indicated that larger alkali-metal cations and subsurface O species promoted cation adsorption, facilitating C–C coupling on CuO_x electrodes. Furthermore, using an electrolyte containing Cs^+ and I^- induced a significant reorganization of the CuO_x surface, forming well-defined Cu species, and enhanced the intermediate stabilization and C_{2+} product selectivity.

Considering the well-documented positive influence of halide ions on CO_2RR performance, MXenes, with abundant halide surface terminations, present a promising platform for enhancing the selectivity of multicarbon products. Halogen-based etching using molecular Cl, Br, or I can introduce halide terminations onto MXene surfaces, potentially modulating active species and regulating the adsorption–desorption dynamics of reaction intermediates during the CO_2RR.[103–105] For instance, a Cu-immobilized $Ti_3C_2Cl_x$ MXene demonstrated over 58% selectivity for CH_3OH, with dominant Cl functional groups residing on the outermost Ti layers.[106] Synchrotron-based X-ray absorption spectroscopy and DFT calculations attributed the exceptional performance of the catalyst to single-atom Cu species with an unsaturated electronic structure ($Cu^{\delta+}$, $0 < \delta < 2$), facilitating a low-energy-barrier conversion from HCOOH* to the CHO* intermediate.

However, despite confirming the abundant Cl terminations, the study did not explicitly address their role in the activity and selectivity of the catalyst. Given the widely accepted understanding that halide ions influence reaction mechanisms by modulating intermediate adsorption and desorption, further investigation of the Cu-immobilized $Ti_3C_2Cl_x$ catalyst is necessary to clarify the role of Cl termination groups. Future research should systematically explore the effects of –Cl, –Br, –F, and –I terminations on MXene-based catalysts, offering deeper insight into their influence on CO_2RR performance and product distribution.

The electrolyte employed during the CO_2RR can also influence product distribution and overall performance. Despite being the most applied electrolyte systems in the CO_2RR, aqueous solutions have limited CO_2 solubility (about 0.034 M), constraining their application in the H-cell. Research efforts have been directed toward using dipolar aprotic solvents, such as acetonitrile (about 0.27 M)[107] and ILs, which can serve as mediators that prevent the HER and as cocatalysts that form complexes with CO_2 molecules to overcome this problem and improve CO_2 solubility. In one of the earliest studies on MXenes using ILs, Handoko et al.[108] combined experimental and theoretical approaches to investigate Ti- and Mo-based MXenes for HCOOH production, achieving a 56% FE in an electrolyte system containing IL 3-butyl-1-methyl-1H-imidazol-3-ium tetrafluoroborate dissolved in an acetonitrile–water solution. This work highlighted the crucial role of –O surface termination groups in suppressing the HER while revealing the limitations of

acetonitrile as an electrolyte due to its volatility, causing fluctuations in HCOOH selectivity.

Attanayake et al.[109] suppressed the competing HER using the IL 1-ethyl-2-methylimidazolium tetrafluoroborate as an electrolyte in acetonitrile. Under these conditions, Ti_3C_2 and Mo_2C demonstrated a remarkable FE of 90% for CO production. Despite the favorable solubility of CO_2 in ILs, their relatively high viscosity compared to conventional solvents poses challenges, including a lower CO_2 adsorption rate and increased pumping costs in industrial applications. Cosolvents, such as water or CH_3OH, can be introduced to reduce viscosity while maintaining CO_2 solubility to mitigate viscosity-related limitations.[110]

Previous studies on energy storage devices have demonstrated strong synergy between surface terminations of MXenes and IL functional groups, significantly influencing supercapacitor performance.[111–114] Applying insight from MXene-IL interactions in energy storage devices to the CO_2RR could enhance interfacial interactions, improving product selectivity and addressing stability challenges. This approach presents a promising strategy for applying the complementary properties of MXenes and ILs to enable efficient and scalable CO_2 conversion into a diverse range of valuable products.

The catalyst structure can also affect the activity and selectivity of the CO_2RR. A Cu-based catalyst is highly capable of producing multicarbon products. However, selectivity toward a specific product is challenging. Nanostructured Cu, including nanoparticles, nanowires, and hierarchical structures with varying compositions, sizes, morphologies, and crystal orientations, has gained considerable research attention due to its ability to enhance the selectivity of the CO_2RR.[115,116] The exposed crystal facets of the nanostructured Cu play a crucial role in determining the reaction pathway and controlling product distribution. Adjusting the exposed facet on the Cu crystals can change the specific atom arrangements, reaction intermediate affinity, and surface energy, influencing the CO_2RR pathway and product distribution.[117]

Luo et al.[118] investigated the facet-dependent selectivity of Cu_2O nanocrystals, demonstrating that tailoring the exposed facets enhanced selectivity toward C_2H_4. Star-shaped Cu_2O nanocrystals with (332) facets achieved over 74% selectivity for C_2H_4. This high selectivity was attributed to a reduction in Gibbs free energy, with the (332) facets exhibiting the lowest energy barrier (0.13 eV) in the initial step of gaseous CO_2 hydrogenation, compared to (111) at 0.20 eV and (100) at 0.22 eV. Furthermore, the in situ Raman spectroscopy of star-shaped Cu_2O (332) nanocrystals revealed the presence of *COOH and *CHO intermediates, indicative of C–C coupling, facilitating C_2H_4 formation.

The nanocrystal structure influences the facet dependence of the selectivity of Cu nanocrystals in the CO_2RR. An investigation of Cu single crystals in an H-cell has revealed that (100) is suitable for C_2H_4 formation, whereas (111) favors CH_4 formation. For example, Gregorio et al.[119] developed a colloidal method to synthesize Cu cubes, spheres, and octahedral nanocrystals and tested them for the CO_2RR in flow cells. The study

revealed that the Cu octahedral nanocrystals dominantly produced CH_4, in line with the presence of the exposed (111) facets. In contrast, the Cu cubes with dominant (100) facets exhibited much higher selectivity (55%) toward C_2H_4. These studies demonstrated the facet-structure dependence of the selectivity of Cu-based nanocrystals. The influence of external factors, such as temperature and applied voltage (constant and pulse/dynamic), remains underexplored in optimizing MXene performance for the CO_2RR. Most studies have focused on ambient temperature conditions,[120] either *via* DFT predictions or experimental investigations, aiming to maintain temperature as a constant parameter to ensure catalyst stability and durability. Conversely, the applied potential is a dynamic factor essential for activating the catalyst surface and forming an E/E interface. Changes in applied voltage alter the charge density on the MXene surface, affecting the organization of ions and solvent molecules in the EDL and affecting CO_2 adsorption and intermediate stabilization. Moreover, potential variations can modify the oxidation state of the catalyst, changing its electronic structure and overall surface properties and influencing reaction pathways and product selectivity.

For example, Han *et al.*[121] used *in situ* X-ray analysis to monitor changes in Sn species' oxidation states and the local chemical environment in the SnO_2/MXene catalyst under various applied potentials ranging from −0.6 to −1.2 V *vs.* RHE. The authors observed a gradual shift toward lower energy on Sn K-edge X-ray absorption near-edge structure (XANES) profiles with a more negative applied potential. They reported a progressive reduction in the oxidation valence state in the CO_2RR. The excellent performance and selectivity of the CO_2RR to

HCOOH in a 0.1 M $KHCO_3$ aqueous solution reached a maximum of 94% at −0.8 V, attributed to the intermediate/mixed Sn oxidation state between metallic Sn^0 and Sn^{4+}.

Furthermore, Govindan *et al.*[122] highlighted the influence of the applied potential on MXene-based catalysts, where tuning the cell potential enabled a palladium (Pd)–MXene nanocomposite to achieve a FE of 67.8% for CH_3OH at −0.5 V *vs.* RHE. Moreover, CO and H_2 became the dominant products at higher potentials, attributed to CO serving as a crucial intermediate in CH_3OH formation. However, as the potential increased, CO desorption from the catalyst surface intensified, restricting its further conversion to CH_3OH and shifting the selectivity toward CO and H_2 evolution. This observation highlights the vital role of the applied potential in determining product selectivity and reaction pathways. However, despite its importance, no studies have investigated using a pulsed potential for MXenes in the CO_2RR, highlighting a notable research gap for future investigation.

The system configuration is a critical factor in determining the overall catalytic performance of MXene-based electrocatalysts in the CO_2RR. This configuration encompasses electrode type (*e.g.*, carbon paper, glassy carbon, and gas diffusion electrodes) and reactor design (*e.g.*, H-cells, microfluidic cells, and membrane electrode assemblies, MEAs). Each component plays a distinct role in controlling mass transport behavior, product selectivity, energy efficiency, and scalability (Fig. 6).

While H-cells are the most widely used reactors for fundamental CO_2RR studies, they frequently underrepresent real-world performance due to low CO_2 solubility ($\sim$34 mM), mass transport limitations, and high ohmic resistance from large
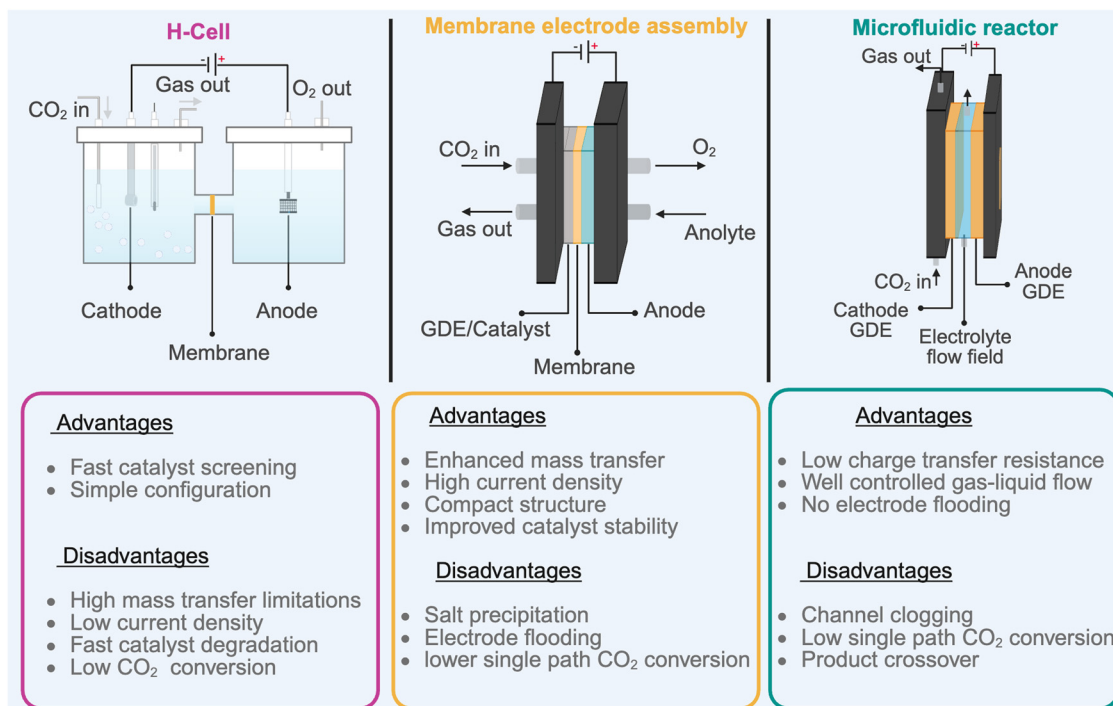

Fig. 6 Schematic of the typical electrochemical flow cells for CO_2 reduction.

inter-electrode spacing (>2 cm). As a result, H-cells typically achieve modest current densities (<50 mA cm^{-2}) and produce faradaic efficiencies that are difficult to reproduce under industrial conditions.[123,124] In contrast, flow-cell reactors, particularly those employing gas diffusion electrodes (GDEs), directly expose the catalyst to a continuous CO_2 gas stream, dramatically improving CO_2 mass transport and achieving reliable partial current densities between 50 and 300 mA cm^{-2}. For instance, a SnO_2 quantum dot/MXene composite attained 57.8 mA cm^{-2} with 94% faradaic efficiency for formate in a flow-cell GDE/MEA configuration, significantly outperforming the H-cell benchmark. Similarly, an FePc/MXene composite tested in a flow cell demonstrated $\sim$98% FE for CO with stability over 24 h, highlighting improved mass transport and HER suppression compared to the H-cell configuration.[125]

MEA-based reactors integrate solid-state ion-exchange membranes, enabling compact reactor designs, ion-specific transport control, and minimal reactant/product crossover. A Bi_2O_3/MXene composite demonstrated continuous operation at 300 mA cm^{-2} with >90% formate selectivity over 60 h in an MEA.[126]

Abdinejad et al.[127] evaluated a Cu–Pd/MXene composite catalyst using both configurations. In an H-cell, the catalyst achieved a CO_2-to-formate conversion with a FE of 79% at -0.5 V vs. RHE. In contrast, when tested in a zero-gap MEA reactor, the same catalyst achieved an enhanced FE of 93% at -2.8 V and a full-cell energy efficiency of 47%, showcasing the MEA's ability to sustain higher current densities and reduce resistance. These comparisons underscore that while H-cells are valuable for mechanistic insights, they are limited in reflecting the behavior of MXene catalysts under realistic, high-throughput conditions. MEAs offer enhanced gas transport, stable interfaces, and minimized side reactions, allowing MXenes to achieve higher selectivity, greater stability, and industrially relevant current densities. This reinforces the need to assess MXene catalysts under MEA configurations to realize and report their catalytic potential. Table 2 shows comparison of MXene catalyst performance across different reactor configurations.

3. MXene fabrication, structure, and characteristics

3.1. MAX phase synthesis and etching

The MAX phase is a layered carbide, nitride, or carbonitride with the formula $M_{n+1}AX_n$. The A layers (group 11 to 16 elements) are weakly bonded to the M layers via metallic bonds, making them selectively etchable, whereas strong covalent bonds hold together the M and X layers. Fig. 7A presents the chemical composition of MAX phase precursors and their MXene derivatives. Since MXenes were first discovered, over 150 MAX phases have been predicted via computational investigations.[129] The diversity of MAX phases is presented through the possible MAX chemical compositions and the ability to form various n structures, including MAX precursors (M_2AX, M_3AX_2, M_4AX_3, and M_5AX_4).[130] Recently, out-of-plane ($M_2M'AX_2$ and $M_2M'_2AC_3$) and in-plane (e.g., $(M_{2/3}M'_{1/3})_2AlC$) ordered structure MXenes have been reported.[131]

The MAX phases are synthesized at elevated temperatures (800 °C to 1800 °C) in an inert atmosphere. The process involves mixing elemental powders (M and A) or carbide/nitride mixtures, followed by sintering. The precursor selection, stoichiometry, and heating rate strongly influence the properties and purity of the MAX phase. Since the discovery of MXenes, extensive research has focused on optimizing MAX phase synthesis, refining etching protocols and improving delamination methods. The addition of excess Ti and aluminum (Al) beyond the stoichiometric ratio during the reactive sintering of Ti_3AlC_2 enhances the stability and conductivity of the resulting MXene.[134,135] This improvement is attributed to the excess Al, which reacts with O in the system, promoting the formation of more stoichiometric Ti_3AlC_2 with fewer defects, including O substitution in the C sublattice.

Recently, Michałowski et al.[136] employed atomic-resolution ultralow-energy secondary-ion mass spectrometry to detect O incorporation in the C sublattice. The study revealed that when a stoichiometric Ti : Al : C ratio is used, Ti_3AlC_2 can contain up to 30% O in the C sublattice, forming an oxycarbide MXene upon etching. In contrast, using excess metals in synthesis led to Ti_3AlC_2 with no detectable O. Excessive A-layer content during the MAX phase synthesis reduces O substitution and C vacancies, improving MXene stability and electronic properties.[134] Similarly, the composition of X in the MAX phase can influence MXene properties.

For example, Shuck et al.[137] used three C sources, graphite, TiC, and C lampblack, to synthesize the MAX phase. The produced MXene exhibited distinct stability and conductivity depending on the composition and morphology. Therefore, choosing elemental precursors, mixing ratios, and sintering conditions is crucial to achieving desirable MAX phase characteristics for

Table 2 Comparative performance of MXene-based electrocatalysts in H-cell, flow-cell, and MEA configurations, showing the same material under different reactor designs, associated current densities, product selectivities, and literature references

| MXene catalyst	Cell configuration	Current density (mA cm^{-2})	Product & FE (%)	Ref.
Au/$Ti_3C_2T_x$ MXene	H-cell	17.3	CO (48.3%), H_2 (25.6%)	128
Cu–Pd/MXene aerogel	H-cell	$\sim$20	Formate ($\sim$79%)	127
Cu–Pd/MXene aerogel	MEA	150	Formate (>90%)	127
FePc/MXene composite	Flow-cell	>100–200+	CO ($\sim$98%) stable	125
FePc/MXene composite	MEA	200+	CO ($\sim$98%), 96% stability	125
Pd–$Ti_3C_2T_x$ MXene	H-cell	$\sim$10–20	CO ($\sim$48%), H_2 ($\sim$26%)	122
SnO_2 QD/MXene composite	H-cell	<30	Formate (<70%)	121
SnO_2 QD/MXene composite	Flow-cell	57.8	Formate ($\sim$94%)	121
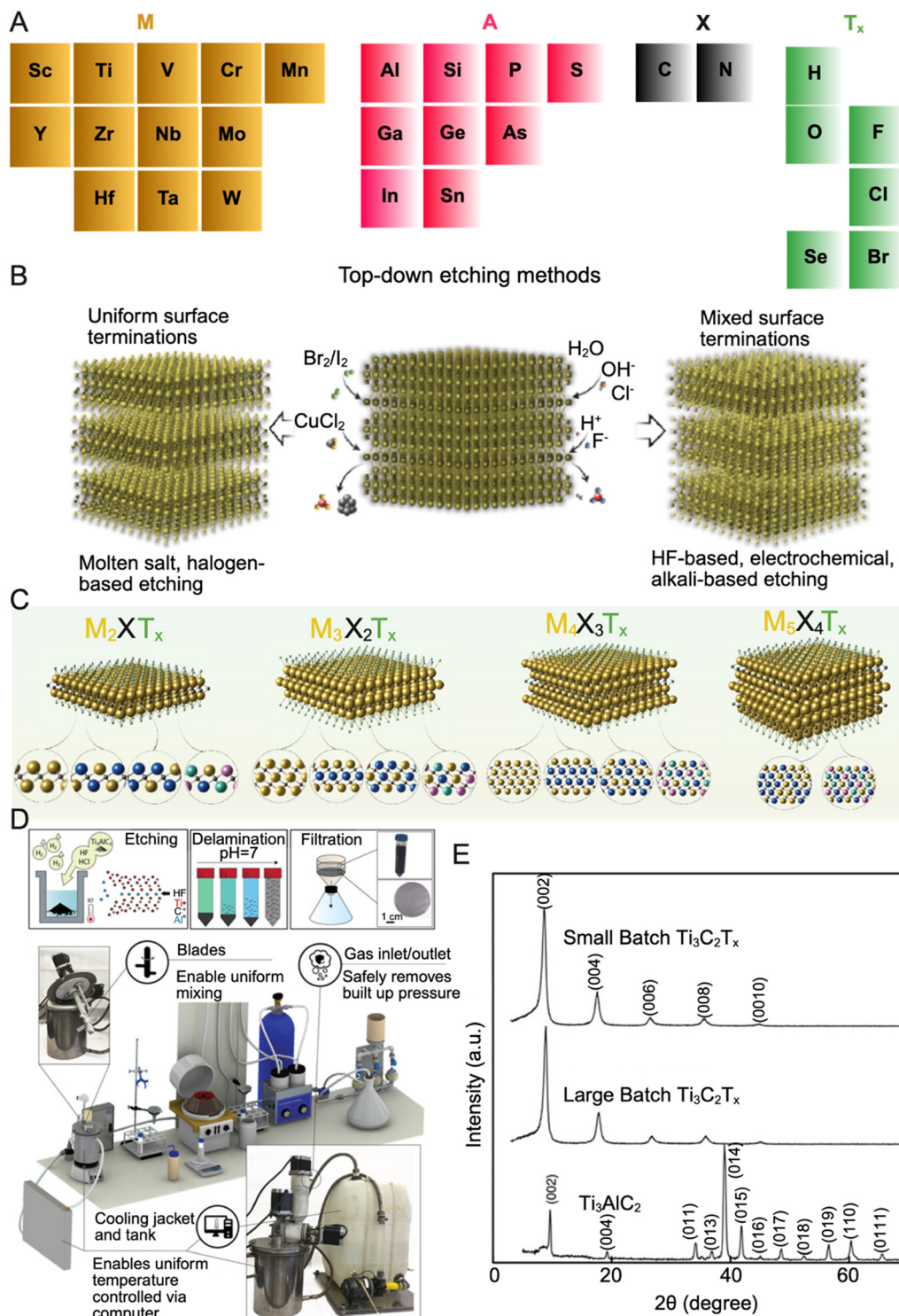
Fig. 7 (A) Periodic tables presenting MAX phase and MXene compositions. (B) Top-down etching methods for MXene synthesis. (C) MXene forms synthesized using top-down etching methods. (B) and (C) Reproduced from ref. 132 with permission from Springer Nature, Copyright [2025]. (D) Schematic demonstrating the large-scale synthesis of MXenes using the HCl:HF:H$_2$O etching method. (E) X-ray diffraction pattern of MXenes synthesized *via* a large-scale process and a small batch. No notable change in structure is observed. (D) and (E) Reproduced from ref. 133 with permission from Wiley and Sons, Copyright [2020].

CO$_2$RR applications. Future research should explore the influence of these factors, particularly the M, A, and X compositions, on the electrocatalytic performance of MXenes.

MXene synthesis involves the removal of the A layer from the MAX phase to form multilayered MXenes, with the reaction's Gibbs free energy determining the etching effectiveness. This

approach is called the top-down approach for MXene synthesis (Fig. 7B). MXenes produced using this approach come in M_2XT_x, $M_3X_2T_x$, $M_4X_3T_x$, and $M_5X_4T_x$ forms (Fig. 7C). Naguib et al.[138] synthesized the first MXene by etching Ti_3AlC_2 with concentrated hydrofluoric acid (HF), selectively weakening Ti–Al bonds while preserving Ti–C bonds. During etching, the initial adsorption of H and F atoms onto Ti atoms selectively weakens the less stable Ti–Al bonds, leaving the stronger Ti–C bonds intact. This process creates interlayer spacing, facilitating the intercalation of HF and H_2O for sequential layer-by-layer etching.[139] This process exposed undercoordinated Ti metallic surfaces, which were saturated with termination groups, such as –O, –OH, and –F, denoted as T_x.[140,141] Since the first reported synthesis of MXenes, significant efforts have been directed toward optimizing synthesis protocols and minimizing the use of hazardous HF. Therefore, numerous alternative methods have been developed, including low HF etching, electrochemical, alkaline, molten salt, and halogen etching approaches.

Low concentrations or reduced quantities of HF yield high-quality MXenes with fewer defects. Acid mixtures have been explored as alternative etching solutions to minimize HF usage while maintaining efficient MAX-phase etching. For example, a comparative study evaluated HF/HCl and HF/H_2SO_4 etching systems to remove the Al layer from Ti_3AlC_2 and reported that MXenes synthesized via HF/HCl displayed larger interlayer spacing and higher structural water compared to HF and HF/H_2SO_4, which might be due to the –Cl termination.[142] Recently, an optimized $HCl:HF:H_2O$ etching solution has gained widespread adoption due to its reduced HF content and ability to produce high-quality MXene sheets. This approach uses a 6:1:3 ratio of HCl, HF, and H_2O per gram of MAX powder.[143]

Shuck et al.[133] applied the $HCl:HF:H_2O$ etching method for the scalable synthesis of up to 50 g of $Ti_3C_2T_x$ MXene (Fig. 7D). Notably, the large-batch synthesized MXene exhibited identical structural and chemical characteristics to small-batch samples, demonstrating that this approach enables scaling up without compromising material quality (Fig. 7E), making it a promising route for commercialization.

In a three-electrode configuration, the electrochemical etching method selectively removes the A atomic layer by applying a potential while using the MAX phase as an electrode. The applied potential disrupts the M–A bond using electrolyte solutions, such as NaCl, HCl, or HF.[144] Effective control over the etching potential and time ensures selective A atom removal, enabling precise control over MXene synthesis. An uncontrollable increase in the applied potential can eliminate the M-layer, yielding amorphous C materials.[145,146]

Chen et al.[147] synthesized $Ti_3C_2T_x$ via electrochemical etching in a mixed lithium hydroxide (LiOH) and lithium chloride (LiCl) aqueous solution, achieving over 90% etching efficiency. The synthesis was performed at 5.5 V for 5 h, using two identical Ti_3AlC_2 blocks as symmetric electrodes. As the etching progressed, the Ti_3AlC_2 cathode remained intact, whereas the Ti_3AlC_2 anode was partially consumed. The presence of Li^+ ions in the etching solution facilitated the etching process by intercalating into the layers and promoting the delamination of the MXene with –Cl surface termination.

Similarly, Shen et al.[148] prepared an F-free $Ti_3C_2Cl_2$ MXene using a molten-salt-assisted electrochemical etching technique. During the electrochemical etching process, the surface termination was modified from –Cl to –O and sulfur (–S), considerably shortening the modification steps and enriching the variety of surface terminations.

Electrochemical etching is a green and safe synthesis method with low energy consumption. However, challenges remain, including forming an amorphous C layer under uncontrolled etching conditions and the relatively low yield of the MXene. Although the MAX phase electrode can be reused multiple times, the typical etching process results in limited MXene production, making it unsuitable for large-scale synthesis. Despite these limitations, this approach can potentially prepare MXenes for the CO_2RR.

Alkaline etching is a nonacid etching method for synthesizing MXenes with functional groups, such as –OH and –O, making it hydrophilic and suitable for fabricating electrodes for aqueous applications, such as the CO_2RR. Despite the limited toxicity of this method, MXene synthesis using this approach is challenging because the reaction is spontaneous at elevated temperatures, making it difficult to control oxidation at elevated temperatures and low concentrations. The fast oxidation is attributed to –OH termination groups that oxidize MXenes quickly.

For example, Li et al.[149] successfully prepared $Ti_3C_2(OH)_2$ MXenes using KOH in a hydrothermal reactor. Replacing the Al atoms with –OH groups allows the formation of 2D $Ti_3C_2(OH)_2$. Similarly, NaOH-assisted hydrothermal alkali etching at 270 °C yielded $Ti_3C_2T_x$ with a yield of 92% and improved interlayer spacing.[150] The primary reaction pathway involves converting Al into Al(oxide) hydroxides, followed by their dissolution in an alkaline medium. Elevated reaction temperatures and concentrated NaOH facilitate the rapid dissolution of Al(oxide) hydroxides, forming F-free MXenes with abundant –OH and –O surface terminations. The abundant –OH terminations on MXenes synthesized using this method may enhance C_2 product formation.

Literature reports indicate that the presence of –OH terminations on Cu catalysts can lower the binding energy of CO and improve the charge equilibrium between C atoms in the adsorbed OCCO intermediate. This interaction reduces the energy barrier for C_2H_4 formation by facilitating CO dimerization.[151–153]

Molten salt etching can be divided into fluoride-containing and fluoride-free molten salt etching.[154] The fluoride-containing approach allows the in situ formation of HF during synthesis. By combining a strong acid (e.g., HCl or H_2SO_4) and fluoride salts (e.g., LiF, NaF, KF, NH_4F, and FeF_3) or using bifluoride salts (e.g., NH_4HF_2, $NaHF_2$, and KHF_2), HF can be formed in situ during the etching process.[154,155] During synthesis, metal cations (Li^+, Na^+, and K^+) enter negatively charged MXene layers and increase interlayer spacing, eliminating the need for an extra intercalation step. The etching temperature
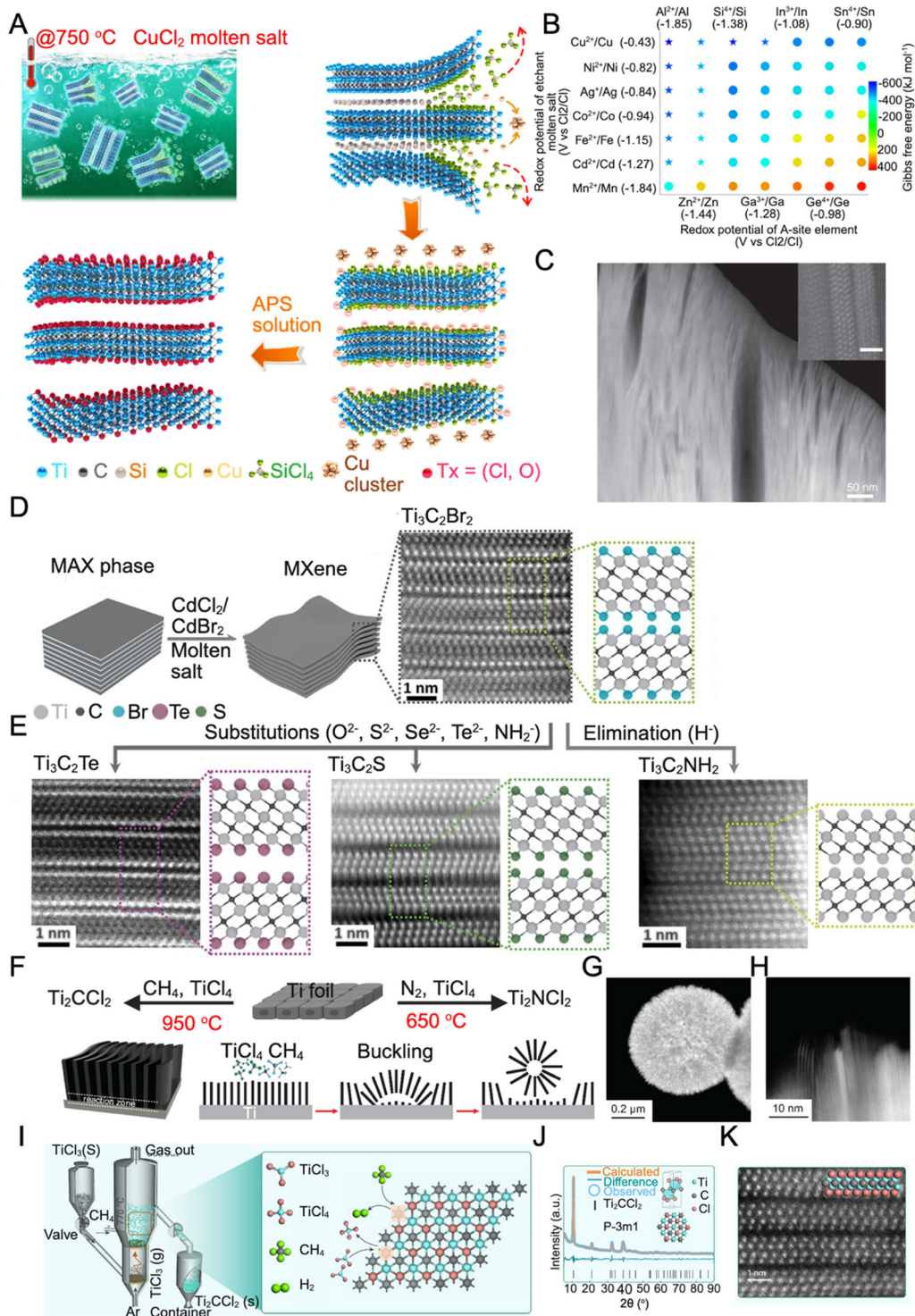
Fig. 8 (A) Schematic of $Ti_3C_2Cl_2$ synthesis *via* the Lewis acid etching route. (B) Gibbs free energy mapping (700 °C) guiding the selection of Lewis acid Cl salts based on the electrochemical redox potential. (C) High-resolution transmission electron microscopy imaging of an MXene. (A)–(C) Reproduced from ref. 158 with permission from Springer Nature, Copyright [2020]. (D) Etching MAX phases in Lewis acidic molten salts and atomic-resolution high-angle annular dark-field (HAADF) image of $Ti_3C_2Br_2$. (E) HAADF images of Ti_3C_2Te, Ti_3C_2S, and $Ti_3C_2NH_2$ MXenes. (B) and (E) Reproduced from ref. 159 with permission from American Association for the Advancement of Science, Copyright [2020]. (F) Schematic of the reaction zone and proposed mechanisms of CVD-Ti_2CCl_2. (G) Scanning transmission electron microscopy (STEM) images of spherical MXenes. (H) High-resolution image of spherical MXenes. (F)–(H) Reproduced from ref. 160 with permission from American Association for the Advancement of Science, copyright [2023]. (I) Schematic of a fluidized reactor bed for the CVD process. (J) X-ray diffraction pattern of Ti_2CCl_2 obtained using FBR-CVD before delamination. (K) Cross-sectional HAADF-STEM image of the (0001) plane of Ti_2CCl_2 flakes. (I)–(K) Reproduced from ref. 161 with permission from Elsevier, Copyright [2024].

and concentration of the acid and fluoride salt can significantly affect the quality of MXene sheets.

Wang et al.[156] reported the synthesis of an MXene with an accordion-like structure by introducing LiF into a NaCl–KCl molten salt etchant with $CuCl_2$. The reaction was kept for 5 h at 750 °C, and monolayer flakes of MXene nanosheets were synthesized by incorporating the prepared MXene into a tetra-butylammonium hydroxide (TBAOH) solution during agitation, achieving an MXene yield of $\approx$ 15% to 20%.

The Lewis acidic molten salt etching approach is proposed to prepare fluoride-free MXenes by adjusting MAX precursors with various Lewis acid salts at elevated temperatures. For example, Li et al.[157] used an element replacement approach that replaces the A-layer atom in the MAX phase with Zn atoms in molten $ZnCl_2$. This approach synthesizes and etches several MAX phases, including Ti_3ZnC_2, Ti_2ZnC, Ti_2ZnN, and V_2ZnC, to achieve their respective MXene derivatives. The MXene synthesis was achieved by the MXene Al-MAX with $ZnCl_2$ in a 1 : 6 molar ratio and heating at 550 °C for 5 h to achieve pure Cl-terminated MXene sheets.

Li et al.[105] expanded this approach using Lewis acidic etching to synthesize MXenes from the MAX phase precursors containing A elements, such as Si, Zn, and gallium (Ga; Fig. 8A). As illustrated in Fig. 8B, this approach can prepare MXenes with other types of A-layer atoms. By tuning the chemistry of the MAX precursor and the composition of the Lewis acid melt, a direct redox interaction between the A element and the cation of the Lewis acid molten salt enables the prediction of MAX phase reactivity in the molten salt, facilitating MXene synthesis. For instance, Ti_3SiC_2 was immersed in molten $CuCl_2$ at 750 °C. During the reaction, the exposed Si atoms, which are weakly bonded to Ti in the Ti_3C_2 sublayers, were oxidized to silicon (Si^{4+}) cations using Lewis acid Cu^{2+}, forming volatile $SiCl_4$ and the concomitant reduction of Cu^{2+} to metallic Cu. The metallic Cu was removed by immersing the $Ti_3C_2Cl_2$ product in an ammonium persulfate solution. High-resolution scanning transmission electron microscopy (STEM) revealed that the resulting MXene exhibited a lamellar microstructure similar to that of the MXene synthesized using the HF etching approach (Fig. 8C). Considering the high activity of Cu for the CO_2RR, this research should optimize this approach to preserve Cu metallic particles in the resulting MXene structure and test it for the CO_2RR.

Kamysbayev et al.[159] employed substitution and elimination reactions in molten organic salts to synthesize MXenes with varied surface termination groups using $CdCl_2$ or $CdBr_2$ molten salts (Fig. 8D). The study demonstrated that Cl^- or Br^- terminated MXenes can actively participate in surface reactions, where halide ion exchange enables precise control over the surface chemistry and properties of MXene sheets. The surface terminations of the synthesized MXenes were further modified by dispersing them in molten alkali-metal halides, such as Li_2Te, Li_2S, Li_2Se, Li_2O, and $NaNH_2$ (Fig. 8E), allowing for tailored functionalization and enhanced material properties.

Recently, Liu et al.[162] prepared $Ti_3C_2T_x$ (T_x: Cl^- and O^-) via a molten-salt-etching route in acetonitrile-based electrolyte.

Moreover, $CuCl_2$ was applied as the main molten salt etching, and NaCl/KCl was employed as a supporting electrolyte. The synthesis was performed at 680 °C for 24 h in an argon (Ar)-filled furnace. The obtained MXene displayed enhanced electrochemical stability.

The literature has reported several new top-down MXene synthesis approaches, including hydrothermal-assisted HCl etching[163] and microwave-assisted molten salt etching.[164–166] These methods are still in their early stages and require more investigation to optimize them to produce high-quality MXenes.

Most studies on MXene synthesis are based on a top-down approach. Three bottom-up synthesis approaches, chemical vapor deposition (CVD), the template method, and plasma-enhanced pulsed laser deposition, have been reported for synthesizing MXenes. The CVD method allows the growth of ultrathin MXene sheets at elevated temperatures and a non-terminated surface.

Xu et al.[167] produced defect-free molybdenum carbide (Mo_2C), tungsten carbide (WC), and tantalum carbide (TaC) thin films using CVD at elevated temperatures (1085 °C). Recently, Wang et al.[160] synthesized Ti_2CCl_2 using CVD. The reaction of CH_4 and $TiCl_4$ on a Ti surface enables direct CVD growth at 950 °C of Ti_2CCl_2 carpets and complex spherulite-like morphologies that form via buckling and the release of the MXene carpet to expose a fresh surface for further reactions (Fig. 8F). Scanning electron microscopy imaging revealed that the synthesized MXene evolved from bulges into spherical MXene vesicles (Fig. 8G) with sheets radiating from the center and oriented normally to the surface (Fig. 8H). The template method uses 2D TM oxide (TMO) nanosheets as templates. During the synthesis, the TMO nanosheets are carbonized or nitrided to form a carbide or nitride MXene, respectively.[168]

For example, Xiao et al.[169] produced molybdenum nitride (MoN) using 2D molybdenum trioxide (MoO_3) nanosheets as templates. MoN was synthesized by annealing the MoO_3 cover with NaCl at 280 °C for 2 h. MoN exhibited very uniform nanosheets with a thickness of about 0.71 nm. The 2D tungsten nitride and vanadium nitride nanosheets were also synthesized using this method. Plasma-enhanced CVD and pulse laser deposition can be combined to prepare 2D MXenes.

Zhang et al.[170] prepared an ultrathin large-area Mo_2C film on sapphire by combining plasma-enhanced CVD and pulse laser deposition. The sapphire substrate was heated to 700 °C for depositing the high-quality Mo_2C film using CH_4 plasma as the C source.

Xiang et al.[161] reported a scalable gas-phase technology for synthesizing Cl-terminated Ti_2CCl_2. The synthesis was conducted in a fluidized bed CVD reactor, where $TiCl_3$ was introduced into the reactor at 770 °C and was rapidly sublimated to form a gaseous precursor for nucleation (Fig. 8I). The gaseous precursors were transported by Ar gas to react with CH_4 in the upper region of the fluidized reactor bed, forming $TiCCl_2$ powders. The process yielded about 0.1 kg per batch, underscoring the high efficiency of the synthesis method. X-ray diffraction (Fig. 8J) and atomically resolved high-angle annular

dark-field (HAADF)-STEM images (Fig. 8K) revealed the typical characteristics of Ti_2CCl_2.

3.1.1. Intercalation and delamination. Top-down approaches for MXene synthesis typically yield multilayer MXenes, requiring intercalation and delamination to obtain monolayer MXene sheets, which have enhanced physical and chemical properties compared to their multilayer counterparts. Due to strong interlayer interactions in multilayer MXenes, the insertion of organic molecules or inorganic ions can weaken these interactions and increase interlayer spacing, facilitating delamination.[171] Common organic intercalants include dimethyl sulfoxide (DMSO), *N*-methyl-2-pyrrolidone, tetramethylammonium hydroxide (TMAOH), TBAOH, hydrazine monohydrate, *N,N*-dimethylformamide, and urea, whereas LiCl is widely used as an inorganic intercalant.[172]

Following the initial discovery of MXenes in 2011, Mashtalir *et al.*[173] demonstrated in 2013 that multilayer MXenes could be delaminated into monolayer MXene nanosheets *via* DMSO intercalation. After delamination, the X-ray diffraction analysis revealed that the interlayer spacing of the $Ti_3C_2T_x$ MXene increased from 1.95 to 3.50 nm, reducing van der Waals interactions and promoting exfoliation *via* ultrasonication. Delamination into the monolayer MXene increases surface terminations and enhances the hydrophilicity and the negatively charged surface of MXene nanosheets, facilitating their dispersion and the formation of stable colloidal solutions. Although DMSO has promising results as an intercalation molecule for $Ti_3C_2T_x$, it is not effective for delaminating other MXene types.

Hydrazine monohydrate, *N,N*-dimethylformamide, and urea have been explored as intercalation agents to exfoliate multilayer $Ti_3C_2T_x$ into a monolayer $Ti_3C_2T_x$ MXene.[173] However, these methods have demonstrated limited efficiency due to the aggregation of monolayers, resulting in thicker flakes (20 to 50 nm). Naguib *et al.*[174] demonstrated that TBAOH, hydroxyl choline, and *n*-butylamine could facilitate the delamination of V_2C_x and Ti_3CNT_x from their multilayered structures into single layers *via* simple handshaking in water. Following intercalation and delamination, the interlayer spacing increased from 2.14 to 3.86 nm for Ti_3CNT_x and from 1.99 to 3.86 nm for V_2CT_x. The similarity in interlayer spacing for both MXenes highlights the crucial role of intercalating molecules in determining the final interlayer spacing of delaminated MXenes.

Han *et al.*[175] demonstrated that hydrothermal-assisted intercalation of TMAOH can efficiently intercalate multilayer $Ti_3C_2T_x$, increasing the monolayer $Ti_3C_2T_x$ MXene yield to over 73% while achieving a thickness of 1.7 nm. The hydrothermal-assisted intercalation process facilitates diffusion and incorporation of TMAOH between layers. Ascorbic acid was introduced as a mild reductant to prevent the oxidation of the MXene at elevated temperatures.

With the continuous expansion of the 2D MXene family, alternative delamination solvents have been explored for various MXene compositions. Montazeri *et al.*[176] applied NaOH to intercalate Na^+ ions into Nb_2CT_x and $Mo_2Ti_2C_3T_x$ multilayers following a washing step with TBAOH. The resulting delaminated MXenes exhibited increased *d*-spacing values of 1.6 and

1.5 nm for Nb_2CT_x and $Mo_2Ti_2C_3T_x$, respectively. In addition to assisting with delamination, NaOH also reduced the surface oxidation of the flakes. Similarly, Mashtalir *et al.*[177] reported amine-assisted delamination of the Nb_2C MXene, where the intercalation of isopropylamine between the Nb_2CT_x layers followed by mild sonication in water for 18 h at room temperature led to successful exfoliation. X-ray diffraction analysis of the delaminated Nb_2CT_x revealed an increased interlayer spacing of 1.23 nm, which is sufficiently large to accommodate more than one isopropylamine molecule and water between layers.

In addition, LiCl can be employed as an intercalator for multilayer MXenes to enlarge their interlayer spacing by inserting Li^+.[143] Zhang *et al.*[178] applied LiCl as an etchant to delaminate $Ti_3C_2Cl_2$, synthesized *via* Lewis acid molten salt etching. A primary challenge associated with Lewis acid molten salt etching is the difficulty of achieving monolayer nanosheets due to the hydrophobic nature and strong interlayer interactions of halogen-terminated MXenes. Delamination was accomplished using a LiCl-assisted DMSO intercalation approach, where the sample was treated for 24 h followed by centrifugation. As $Ti_3C_2Cl_2$ is hydrophobic, hydrated cations struggle to intercalate between layers. The experiment was conducted in a moisture-free environment to avoid forming a hydration shell around Li^+, which could hinder intercalation.[179]

Notably, the HCl/LiF molten salt etching approach eliminates the need for additional intercalation because MXenes synthesized *via* this method can be directly delaminated. This result is attributed to the spontaneous insertion of Li^+ into interlayers, expanding and weakening interlayer interactions, facilitating separation into monolayers *via* ultrasonication or simple shaking by hand.[180]

Song *et al.*[181] proposed a freeze-sonication delamination strategy for exfoliating a multilayer MXene into a monolayer MXene with the yield exceeding 74%. This approach applies the synergistic effect of ultrasonic treatment and ionic intercalation, facilitating the penetration of numerous water molecules into the interlayer space. The volume expansion, followed by ultrasonic treatment in a frozen state, forms the monolayer MXene. The delaminated MXene demonstrated an excellent gravimetric capacitance of 261.1 F g^{-1} and satisfactory cycling stability. Many of the reported delamination approaches produced MXenes with smaller flakes, limiting their application for large MXene flakes.

3.1.2. Scalability and defect minimization. Large-scale synthesis of various MXenes, beyond the commonly reported Ti_3C_2, is essential to broaden their practical use in catalytic applications such as CO_2 reduction. Conventional top-down synthesis methods, particularly HF-based etching (including HF, $HCl/HF/H_2O$, and LiF/HCl mixtures), are widely adopted for MXene production due to their simplicity and relatively high throughput. However, these approaches suffer from significant limitations when applied to large-batch synthesis. Challenges include the toxicity of etchants, poor control over surface terminations (typically resulting in F-rich terminations), and considerable variability in flake morphology and chemistry,

Table 3 Comparative overview of top-down MXene synthesis methods

Method	Scalability and throughput	Termination control	Advantages	Industrial suitability	Key limitations
HF etching[141]	High (tens of grams per batch)	Poor (–F dominated)	Simple, fast, widely adopted	Mature, used in academic and lab-scale work	Highly toxic; uncontrolled terminations; defect formation
HCl–HF–H$_2$O/LiF–HCl[105,133]	Moderate (~5–15 g per batch)	Moderate (mixed –F/–OH)	Safer than pure HF; better delamination via Li$^+$	Feasible at lab and pilot scales (~50 g)	Involves fluoride; sensitive to processing parameters
Electrochemical etching[147]	Low (batch); moderate (flow reactors: ~10 g h^{-1})	High (tunable –O, –Cl)	Fluoride-free; selective and tunable; potential-controlled	Promising for industrial translation	Lower yield; possible defect formation; scaling challenges
Alkaline etching[149,150]	Moderate (gram-scale hydrothermal setups)	Good (–O, –OH rich)	Fluoride-free; environmentally benign; improved hydrophilicity	Feasible for specific MAX phases	Limited to few MAX phases; low efficiency
Molten salt etching[162,184]	Moderate to high (up to tens of grams per run)	Moderate (–Cl, –O, –S possible)	Fluoride-free; high crystallinity; controlled terminations	Pilot studies reported	Requires >600 °C; substrate dependent
Halogen etching[159,161]	Moderate–high (~0.1 kg per batch via a CVD or halide vapor route)	Tunable (–Cl, –Br, –I)	Unique terminations; dry etching; scalable in CVD setups	Emerging technique	Toxic gases; process maturity is low

including thickness, lateral dimensions, and termination groups, all of which adversely impact catalytic performance and batch-to-batch reproducibility.[182,183] Alternative etching techniques have emerged, including low-HF protocols, electrochemical etching, alkaline (e.g., NaOH/KOH) etching, molten salt, and halogen-based etching. Each offers different trade-offs regarding yield, safety, termination control, and structural preservation.[184] For instance, molten salt etching provides better control over surface terminations (e.g., –Cl and –O) without hazardous liquid acids, though it requires high temperatures (>600 °C).[184] Electrochemical etching in flow reactors enables tunable, fluoride-free synthesis under ambient pressure, but is limited by relatively low yields and the risk of defect formation from overpotential exposure.[182] These methods are summarized in Table 3, which compares key parameters including scalability, termination control, industrial suitability, and limitations.

As MXene synthesis scales toward industrial production, reducing structural defects and chemical impurities becomes vital for preserving material performance and enabling application-specific functionality.[133] Several complementary strategies have been proposed to mitigate these challenges throughout the synthesis workflow. Continuous-flow etching systems offer more homogeneous reaction environments than static batch processing, ensuring consistent exposure of MAX phases to etchants and minimizing local concentration gradients that can induce uneven etching.[185] This leads to improved uniformity in layer thickness and flake size.[133,185] Additionally, precursor engineering, such as stoichiometric optimization of MAX phases with slight excess of Ti or Al, can suppress intrinsic carbon vacancies and oxygen substitutions that degrade the final MXene quality.[134,137] The choice of etching media significantly affects structural integrity and termination control. Mixed-acid systems, such as the commonly used 6 : 1 : 3 HCl : HF : H$_2$O ratio, offer safer and more reproducible etching than pure HF, reducing structural collapse and enhancing monolayer yield.[186] Shuck et al.[187] demonstrated that this protocol could be scaled to synthesize up to 50 g of Ti$_3$C$_2$T$_x$ MXene per batch, while maintaining flake morphology and surface chemistry similar to those obtained in small-scale syntheses. Among the emerging approaches, soft delamination has shown significant promise.[188,189] This method eliminates ultrasonication, shaking, or centrifugation while separating MXene sheets. Instead, the intercalated MXene mixture is left undisturbed for ~30 minutes, allowing gravity-assisted flake separation and the formation of a dark colloidal suspension. Although this method tends to yield more bi- and tri-layered flakes and is relatively slow, it produces large, low-defect flakes ideal for catalytic applications where surface integrity is critical.[188,189]

Finally, storage and environmental stability must be considered, as freshly synthesized MXenes are highly susceptible to oxidation and hydrolysis when exposed to air or moisture. Best practices include storing MXenes under inert atmospheres (e.g., Ar or N$_2$), applying freeze-drying techniques to avoid hydrolysis, or using protective encapsulation (e.g., polymer or carbon coatings) to retain surface activity before electrochemical

deployment.[190,191] Collectively, these defect-mitigation strategies, spanning reactor design, etchant optimization, purification, delamination, and post-synthesis stabilization, are critical for producing high-quality, scalable MXenes suitable for the industrial CO_2RR and other energy applications.

3.2. MXene properties

MXenes possess a unique combination of physicochemical properties, making them promising materials for the CO_2RR. Their compositional diversity, derived from various transition metals (M), carbon or nitrogen X layers, and surface terminations, grants them exceptional tunability of electronic structure,[186] metallic electronic conductivity,[171] and mechanical robustness.[192] Pristine MXenes such as Ti_3C_2 are metallic, with reported conductivities as high as 24 000 S cm^{-1},[171,193,194] which facilitates rapid electron transfer kinetics critical for electrocatalysis.[132] Their surface termination groups (e.g., –O, –OH, –F, and –Cl) play a central role in modulating reactivity by stabilizing key intermediates (*COOH and *HCOO) and adjusting binding energies, thereby influencing product selectivity. These terminations also impart hydrophilic behavior,[195] enhance electrolyte accessibility, and affect mechanical properties, such as Young's modulus, which ranges from ∼0.33 to 0.50 TPa depending on surface chemistry, synthesis route, and defect density.[196,197] MXenes also demonstrate thermal stability under inert conditions (up to ≥500 °C)[198] and are structurally robust in acid electrolytes or under electrochemical cycling when surface terminations are well controlled. However, their susceptibility to oxidation and hydrolysis in ambient or aqueous environments is a well-documented challenge. Therefore, maintaining MXene stability during the CO_2RR requires appropriate synthesis methods, surface passivation, and environmental control. Several studies have explored strategies to mitigate this degradation, demonstrating long-term cycling stability and preserved morphology in a controlled environment. For example, Xie et al.[199] performed a comprehensive DFT analysis showing that Ti_2C and Ti_3C_2 MXenes retain their structural integrity and electronic conductivity during multivalent ion intercalation. Their findings suggest that MXenes can exhibit structural and electrochemical stability under conditions relevant to energy storage, provided that surface terminations and operating environments are carefully controlled. Also, Ghidiu et al.[154] demonstrated long-term electrochemical stability of $Ti_3C_2T_x$ synthesized via a LiF–HCl route, maintaining performance over thousands of cycles in 1 M H_2SO_4. This suggests that MXenes can exhibit high structural stability under specific aqueous electrochemical conditions. In contrast, Cao et al.[190] highlighted degradation pathways and proposed mitigation strategies including (i) defect-controlled synthesis, (ii) post-treatment (e.g., annealing or reduction), (iii) encapsulation with carbon or polymer coatings, and (iv) controlled storage under inert, low-moisture conditions. Soomro et al.[200] further reported that low-temperature, deoxygenated storage extended the stability of aqueous $Ti_3C_2T_x$ dispersions up to 60 days. Post-treatment techniques such as thermal annealing under an inert gas or chemical functionalization can be employed to remove labile terminations or introduce more stable groups, thereby improving MXene's catalytic performance. Ultimately,

the catalytic behavior of MXenes for the CO_2RR depends not only on their inherent properties but also on how they are processed and stabilized. Post-reaction and operando characterization (e.g., XPS, XRD, Raman, and XAS) will be crucial to track structural evolution and guide the rational design of durable, selective MXene-based electrocatalysts. Despite their known advantages, current understanding of MXenes in the CO_2RR remains largely based on computational studies. Experimental efforts are urgently needed to validate theoretical predictions, tune surface chemistry, enhance electrode–electrolyte interactions, and achieve long-term stability and selectivity under realistic reaction conditions.

4. Effect of surface chemistry

The surface chemistry of MXenes plays a pivotal role in governing CO_2 adsorption behavior, stabilization of key reaction intermediates, and product selectivity during electrochemical reduction. Computational investigations, especially density functional theory (DFT) studies, have demonstrated that specific surface terminations, such as –O and –OH, significantly lower the Gibbs free energy barriers for the formation of intermediates like *COOH and *HCOO, thereby favoring the production of CO and formic acid (HCOOH). In contrast, –F terminations typically exhibit weak binding with *CO_2 and *CO, leading to reduced catalytic activity but may promote *CHO intermediate formation, thereby shifting selectivity toward CH_3OH or CH_4 under specific conditions. More recently, halogen terminations (e.g., –Cl), introduced via molten salt or halogen etching, have been shown to alter surface charge distribution and electronic structure, potentially influencing intermediate adsorption and desorption dynamics. However, their direct influence on CO_2RR performance remains insufficiently explored and warrants further studies.

DFT calculations further indicate that CO_2 interacts with MXene surfaces via physisorption, driven by noncovalent interactions, or chemisorption, involving covalent bonds with surface metal sites. The computed Gibbs free energy (ΔG) for chemisorption varies substantially depending on the MXene composition, ranging from −3.19 to −1.29 eV, as summarized in Table 4. These energetic variations, combined with the electronic effects introduced by different surface terminations, underscore the importance of functional group engineering in tuning MXene-based catalyst activity and selectivity toward the targeted CO_2RR products.[120,201] These energetic variations and the electronic effects introduced by different surface terminations underscore the critical importance of tailoring MXene functional groups to direct specific CO_2RR pathways. Table 5 compares the effects of MXene surface terminations on CO_2RR intermediates and product selectivity.

Among TM-based MXenes, Group IV (e.g., Ti_3C_2, Zr_3C_2, and Hf_3C_2) exhibits a stronger binding affinity for CO_2 compared to Group V (e.g., V_2C and Nb_2C) or VI (e.g., Mo_3C_2 and Cr_3C_2).[120] This trend can be attributed to the TM atoms' electronic configuration and d-band center, influencing the overlap between metal orbitals and CO_2 antibonding orbitals.[202,211,212] For example, Mo_3C_2 and Cr_3C_2 MXenes preferentially interact

Table 4 Gibbs free energy of reaction (in eV) for CO_2RR intermediates calculated from the density functional theory[202]

Species/M_3C_2	Group IV Ti_3C_2	Group V Zr_3C_2	Group VI Hf_3C_2	V_3C_2	Nb_3C_2	Ta_3C_2	Cr_3C_2	Mo_3C_2
*CO_2	−0.59	0.17	0.18	0.29	0.35		0.25	0.15
**CO_2	−3.01	−3.19	−3.05	−1.47	−1.60	−2.30	−1.29	−2.11
**OCHO	−2.04	−2.25	−2.89	−1.40	−1.71	−1.58	−1.61	−1.74
**HOCO	−2.06	−2.49	−2.79	−1.41	−1.54	−1.92	−1.74	−1.91
**OCH_2O	−3.51	−4.08	−4.31	−1.93	−2.22	−2.86	−1.60	−1.64
**HCOOH	−1.01	−2.19	−2.47	−0.15	−0.12	−0.32	0.01	−0.78
**CO	−1.18	−1.11	−1.54	−1.45	−1.39	−1.80	−2.00	−2.27
**$HOCH_2O$	−2.47	−2.82	−3.11	−1.59	−1.88	−2.56	−1.85	−2.15
**$HOCH_2OH$	−1.09	−1.07	−3.56	−0.61	−0.68	−1.10	−0.69	−0.90
**H_2CO	−2.43	−3.21	−3.31	−1.81	−2.16	−2.39	−1.78	−1.86
**C_2OH	−1.58	−2.05	−1.89	−1.26	−1.36	−1.94	−1.51	−1.64
**CH_3O	−2.93	−3.12	−3.33	−2.20	−2.36	−2.98	−2.12	−2.53
**CH_2	−1.81	−1.88	−1.21	−0.97	−1.47	−2.33	−1.65	−2.11
**CH_3OH	0.06	0.07	0.01	0.33	0.08	0.22	0.33	0.17
**O	−4.80	−5.24	−5.23	−3.45	−3.95	−4.27	−3.53	−3.57
**CH_3	−2.04	−2.37	−2.86	−2.26	−2.47	−3.27	−2.52	−2.98
**OH	−4.59	−4.65	−4.80	−3.70	−3.90	−4.35	−3.73	−3.91
**CH_4	−1.18	−0.70	−0.94	−2.15	−0.77	−0.82	−0.55	−0.70
**H_2O	−3.03	−2.96	−3.04	−2.46	−2.37	−2.64	−2.55	−2.88

with CO_2 over H_2O, making them highly promising for the CO_2RR in aqueous environments. The mechanistic pathway for CH_4 formation on Mo_3C_2 involves successive hydrogenation steps of intermediates, such as OCHO*, •OCH_2O*, and $HOCH_2O$*, yielding CH_3O* and CH_4 as products (Fig. 9A). The DFT calculations suggest that CH_3O* is thermodynamically favored over H_2COH* during the fifth H^+/e^- addition, directing the reaction away from CH_3OH and toward CH_4 formation.

Moreover, M_2C MXenes, such as V_2C and Cr_2C, have demonstrated potential for HCOOH production, as evidenced by a volcano-type relationship between the adsorption strength and catalytic activity (Fig. 9B). This relationship suggests that intermediate adsorption strengths facilitate efficient CO_2-to-HCOOH conversion. Excessively strong adsorption impedes intermediate desorption, whereas weak adsorption hinders activation, demonstrating the critical role of adsorption energy in catalytic performance.[121,214–216]

The surface functionalization of MXenes significantly enhances their catalytic performance by modifying electronic properties, adsorption energies, and reaction pathways.[217,218] Oxygen-terminated MXenes (e.g., Ti_2CO_2 and V_2CO_2) are effective for the CO_2RR because the pathway to *HCOOH is preferred over the *CO pathway due to the stabilizing effect of –O groups on reaction intermediates (Fig. 9C).[211] Oxygen vacancies, forming during the reaction, further improve selectivity by stabilizing transition states and creating active sites for intermediate binding. For instance, O-terminated MXenes have been reported to preferentially catalyze CO_2 to HCOOH with reduced overpotentials, applying the accessibility of H-coordinated mechanisms over C-coordinated pathways.[219] In addition, $Sc_2C(OH)_2$ and $Y_2C(OH)_2$ are promising candidates for CH_4 production due to the reactive H atom in the –OH group. This reactive H atom facilitates stable intermediate formation, lowering overpotentials and enhancing selectivity for CH_4 formation.[205] Fluoride-containing terminations influence product pathways differently. Furthermore, Ti_3C_2 MXenes with –F terminations tend to favor a path involving formaldehyde intermediates, forming CH_3OH. In contrast, –F-free MXenes follow a distinct mechanism, producing HCOOH and methylene glycol, decomposing into CH_3OH and water.[220]

Sun et al.[213] used DFT to evaluate the activity and selectivity of a dual-atom-modified MXene catalyst for the CO_2RR to C_2H_6O. They demonstrated that the Co–Co dual-atom catalyst, with its asymmetric C–C coupling mechanism, achieves high catalytic activity due to its moderate d-band center, optimally balancing electron occupancy in antibonding orbitals, ensuring efficient adsorption of reaction intermediates. The d-band analysis revealed that vanadium (V)–V and chromium (Cr)–Cr dual-atom catalysts, characterized by higher d-band centers, exhibit stronger adsorption of intermediates (*CH_3CH_2O and

Table 5 Effects of MXene surface terminations on CO_2RR pathways and intermediates

| Termination	Representative MXenes	Key intermediaries	Favored product(s)	Mechanistic insight
–O[203,204]	$Ti_3C_2O_2$, Ti_2CO_2	*COOH, *HCOO	CO, HCOOH	Strong binding of O-bound species; promotes proton-coupled electron transfer
–OH[120,205,206]	$Ti_3C_2(OH)_2$	*COOH	CO	Increases local proton availability; improves surface hydrophilicity
–F[207–210]	$Ti_3C_2F_x$	*CHO, weak *CO_2	CH_3OH, CH_4 (low rate)	Weakens CO_2 adsorption; shifts path to *CHO; often lowers activity
–Cl[209]	$Ti_3C_2Cl_2$	Not fully studied; charge effects	(under study)	Alters electronic distribution; stabilizes some adsorbates; promising but immature
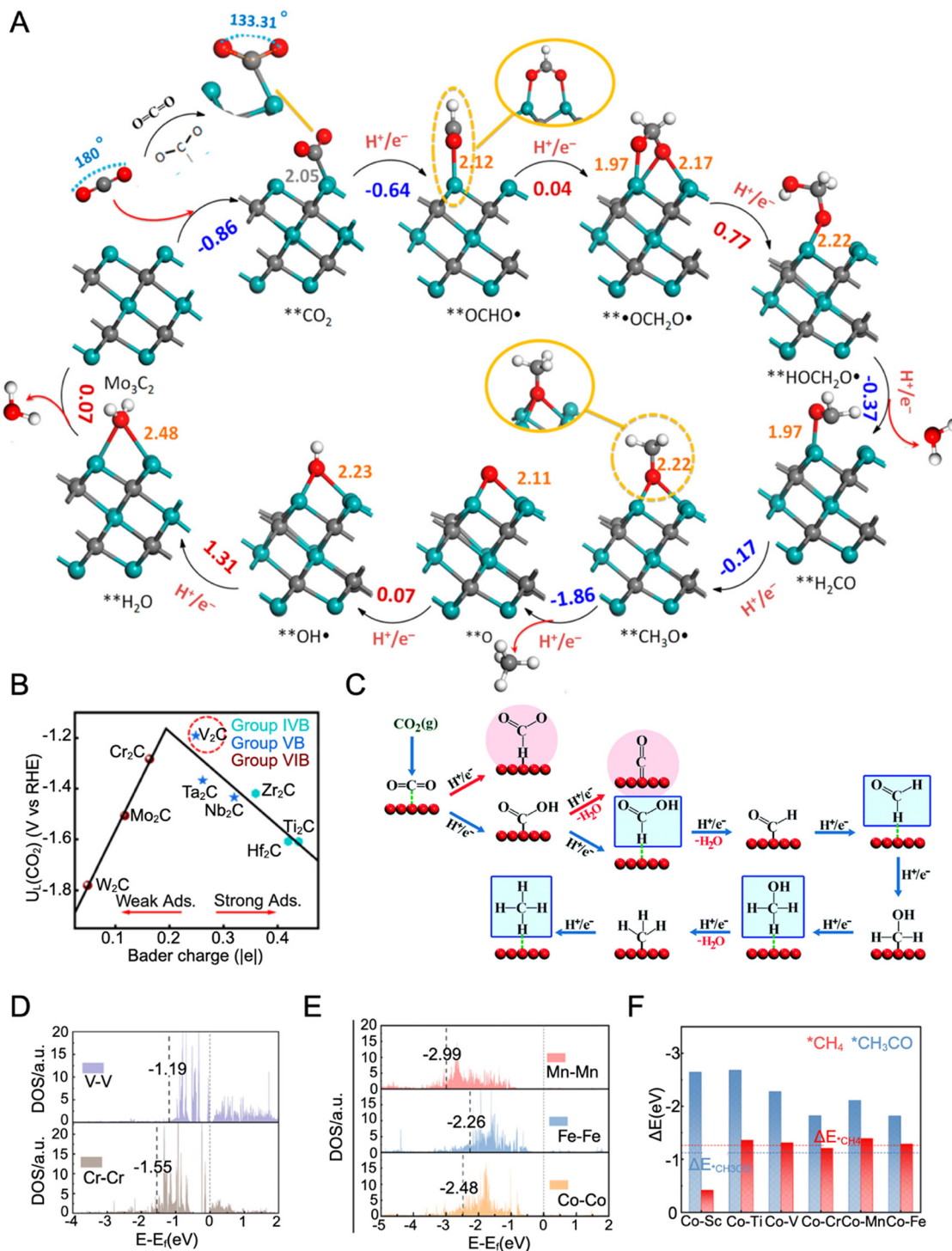
Fig. 9 (A) CO_2 conversion mechanism into $*CH_4$ and $**H_2O$ catalyzed by Mo_3C_2 (Reprinted with permission from *ACS Nano* 2017, 11, 11, 10825−10833. Copyright [2017] American Chemical Society). (B) Volcano-type relationship between U_L and the Bader charge of $*HCOOH$ on M_2C (Reprinted with permission from Ind. Eng. Chem. Res. 2023, 62, 48, 20716−20726. Copyright [2023] American Chemical Society). (C) Reaction mechanism of electrochemical reduction of CO_2 on O-terminated MXenes (Reproduced from ref. 211 with permission from Royal Society of Chemistry, Copyright [2022]). (D) and (E) Density of states (DOS) corresponding to d-orbitals of the adsorbed dual-atom, where the d-band center is denoted by dashed lines. (F) Adsorption energy of $*CH_3CO$ and $*CH_4$ intermediates on dual-atom catalysts/Ti_2CO_2. (D)−(F) Reproduced from ref. 213 with permission from Royal Society of Chemistry, Copyright [2025]).

$*CH_2OHCH_2O$), making hydrogenation steps energetically demanding, with energy barriers of 0.81 and 0.93 eV, respectively (Fig. 9D). In contrast, manganese (Mn)–Mn, iron (Fe)–Fe, and cobalt (Co)–Co dual-atom catalysts have d-band

Table 6 Summary of CO_2RR results using MXene-based electrocatalysts

Electrocatalyst	Potential	Current density (mA/cm^2)	Electrolyte	Faradaic efficiency (%)	Prod.	Ref.
Pd-MXene	0.5 V	17	CO_2-saturated 1.0 M $KHCO_3$	67.8	CH_3OH	122
SA-Cu-MXene	−1.4 V *vs.* RHE	−21.3	0.1 M $KHCO_3$	59.1	CH_3OH	106
CdS/Ti_3C_2	−1.0 V$_{RHE}$	∼6.4	0.1 M $KHCO_3$	94	CO	222
VS-CdS/Ti_3C_2	−1.0 V$_{RHE}$	∼−6	0.1 M $KHCO_3$	96	CO	
M_xO_y/MAX hybrid	−0.4 to −0.6 V	2.4	0.5 M $NaHCO_3$	67	CO	223
Ag–$ZnO/Ti_3C_2T_x$	−0.87 V$_{RHE}$	22.5	0.5 M $KHCO_3$	98	CO	224
d-$Ti_3C_2T_x$	−2.2 V *vs.* SCE	−1.5	Acetonitrile, 1 ethyl-3 methylimidazolium tetrafluoroborate EMIMBF4	65	CO	108
d-Mo_2CT_x	−2.2 V *vs.* SCE	−2.5	Acetonitrile, 1 ethyl-3 methylimidazolium tetrafluoroborate EMIMBF4	90	CO	108
Cu–Pd/MXene	−2.8 V	150	0.1 m $KHCO_3$	93	Formate	127
SnO_2/MXene	1.1 V	−57.8	CO_2-saturated 0.1 M $KHCO_3$	94	Formate	121
ZnO–Fe-MXene	1.0 V	18.745	0.5 M NaOH	—	Formate	225
Cu-/$Ti_3C_2T_x$	−1.5 V *vs.* Ag/AgCl	−1.08	0.1 M $NaHCO_3$	58.1	HCOOH	76
MXene ($Ti_3C_2T_x$) modified with boron-doped diamond	−1.3 V *vs.* Ag/AgCl		0.5 M KOH	97	HCOOH	226

centers positioned farther from the Fermi level (Fig. 9E), allowing antibonding orbitals to be more readily occupied by electrons. This positioning weakens the adsorption of intermediates (Fig. 9F), facilitating smoother reaction pathways without excessive energy barriers and increasing chemical reactivity.[221]

Table 6 presents innovative MXene-based electrocatalysts, their electrocatalytic activities, working electrolytes, performance, and CO_2RR products, further driving innovation in MXene-based electrocatalysts toward the CO_2RR.

5. Structural engineering

MXene-based catalysts are emerging as promising electrocatalysts for the CO_2RR due to their excellent electronic conductivity, large surface area, tunable surface chemistries, and structural robustness.[227,228] Their surface termination groups can effectively stabilize critical reaction intermediates, facilitating efficient proton-coupled electron transfers essential for CO_2 activation and subsequent reduction pathways. Despite these beneficial properties, the presence of specific surface functionalities, particularly hydrogen-affinity groups (such as –OH or –F), can unintentionally promote the competing hydrogen evolution reaction.[229,230] Specifically, the high density of reactive sites and negatively charged surfaces of MXenes can readily adsorb protons from aqueous electrolytes, thereby enhancing HER activity.[231] This unintended promotion of the HER poses a significant challenge by diverting electrons and protons from CO_2 reduction, thereby reducing selectivity toward valuable carbon products. To address this intrinsic limitation, various structural engineering approaches have been developed. These strategies include controlled surface termination modification, defect and vacancy engineering, single-atom or heteroatom doping, formation of MXene-based heterostructures, and hybrid composite catalysts. These engineering methods are crucial to selectively suppress HER activity while enhancing MXene-based catalysts' performance and selectivity toward desired CO_2RR products.[127,128,232–234]

5.1. Surface termination engineering

The catalytic selectivity of MXenes toward the CO_2RR strongly depends on surface termination groups (*e.g.*, –O, –OH, –F, and –Cl).[235] Table 5 compares the effects of MXene surface terminations on CO_2RR intermediates and product selectivity. For instance, oxygen-terminated MXenes (–O) strongly stabilize key reaction intermediates such as *COOH and *HCOO, reducing the energy barriers for CO_2 conversion reactions and selectively suppressing the HER.[207] Computational studies conducted by Albertus *et al.*[236] demonstrated that oxygen terminations on Ti and Mo-based MXenes significantly enhance CO_2 adsorption and intermediate stabilization, promoting selective CO_2RR towards formic acid.[209] In contrast, MXenes with abundant fluorine (–F) terminations generally exhibit weaker CO_2 adsorption and lower selectivity for carbon-based products due to increased HER activity. Meng *et al.* explicitly found that fluorinated Ti_3C_2 MXenes exhibit a higher HER overpotential (∼0.58 V), indicating their stronger proton affinity and subsequent HER promotion. Additionally, recent studies have explored halogen-terminated MXenes (*e.g.*, –Cl, –Br, and –I), synthesized *via* molten salt or halogen etching methods, that offer potential avenues to adjust the electronic structure of MXenes and weaken proton adsorption, which may reduce HER activity.[237] However, comprehensive experimental validation of HER suppression in halogen-terminated MXenes remains limited and warrants further investigation.

5.2. Defect engineering and heteroatom doping

Engineering defects and doping MXenes with heteroatoms have proven effective strategies for improving CO_2RR selectivity and suppressing the HER by altering electronic structures, modifying intermediate adsorption energies, and enhancing active-site densities.[238–241] Introducing controlled oxygen vacancies, metal vacancies, or edge defects can significantly boost MXene catalytic performance by selectively stabilizing CO_2-derived intermediates. For example, Qian *et al.*[34] employed DFT to investigate dual-oxygen vacancies in $Mo_2TiC_2O_2$ MXenes, revealing enhanced catalytic activity and C–C coupling due to enriched

adsorption of reaction intermediates. Furthermore, heteroatom doping (such as N, P, S, or transition metals) provides another powerful route to tune MXene catalytic properties. Three distinct doping strategies have been identified: The lattice substitution, functional substitution, and surface adsorption. Lattice substitution involves replacing atoms in MXene lattices to alter their electronic structures significantly.[242] Functional substitution adjusts surface-functional groups to improve catalytic selectivity. Surface adsorption involves anchoring active dopants on MXene surfaces, stabilizing CO_2RR intermediates, and selectively inhibiting the HER. For instance, nitrogen-doped MXenes exhibited enhanced electronic modulation, reducing HER selectivity and promoting carbon-based products such as CO and formic acid.[243]

5.3. Hybrids and heterostructures

Forming MXene-based heterostructures or hybrids by integrating MXenes with other 2D materials or active components effectively combines their intrinsic properties, mitigates individual limitations, and significantly enhances CO_2RR selectivity and HER suppression.[244] Heterostructure formation typically involves the *in situ* growth of complementary 2D materials onto MXene surfaces, facilitated by electrostatic interactions or covalent bonding.[245,246]

Liu *et al.*[247] demonstrated the synthesis of MXene/metal–organic framework (MOF) heterostructures through electrostatic attraction, where the surface terminations of the $Ti_3C_2T_x$ MXene strongly interacted with MOF precursors, forming well-integrated composites that effectively enhanced CO_2 adsorption and catalytic selectivity. Similarly, a covalent organic framework (COF)–Ti_3C_2 heterostructure achieved >90% CO selectivity at −0.6 V *vs.* RHE due to the synergistic effect of the MXene's large exposed surface area and the COF's catalytic functionalities, substantially suppressing the HER.[248] This significant performance was primarily attributed to the large, exposed surface of the MXene, which effectively disperses the COF, endows the heterojunction with more active sites, and facilitates efficient transport channels. The 3D MXene/graphene oxide/perylene diimide aerogel heterostructure was synthesized *via* impregnation and freeze-drying for the photocatalytic CO_2RR.[233] The resulting heterostructure featured a large surface area, an enhanced photogenerated carrier, and an electron transfer network facilitated by π–π stacking *via* electrostatic attraction. This structural configuration, interconnecting the faces of the heterostructure, promotes the efficient transfer of photogenerated electron–hole pairs, enabling rapid carrier movement and separation. Additionally, perylene diimide functions as an electron donor, activating catalytic sites for enhanced photocatalytic CO_2RR.

5.4. Single-atom catalysts

The size of metal particles in metal-based heterogeneous catalysis is intricately linked to catalytic activity.[249] Catalytic activity increases as the size of metal nanoparticles decreases until they reach an optimal size. Understanding this fundamental concept has played a significant role in advancing SACs,

which display high catalytic activity and maximize metal utilization due to the significantly larger surface area and quantum size effects of metal nanoparticles compared to their bulk counterparts.[250–252] Based on this well-established principle, extensive studies have demonstrated that controlling the structure and size of metal nanoparticles at the atomic level maximizes metal utilization and enhances electrocatalytic performance.[253] The choice of support material for dispersing single metal atoms plays a crucial role in determining the activity and stability of single atoms under reaction conditions. Therefore, strong metal–support interactions are essential for maintaining catalyst performance.[254]

Computational and experimental studies have highlighted the potential of MXenes as promising support materials for facilitating strong metal–support interactions in CO_2RR catalysts. The abundant surface-functional groups and metal vacancy defects in MXenes serve as ideal anchoring sites for single metal atoms, primarily due to the high surface energy, adjustable electronic structure, and uniform atomic arrangement of MXenes.[214,255–257] The synthesis of MXene-based SACs can be achieved using three strategies: surface adsorption, metal vacancy anchoring, and anchoring at surface-functional group vacancies.[258] According to a computational study, the adsorption of single metal atoms is possible on the top, hollow (hcp and fcc), and bridge sites.

Chen *et al.*[259] employed electrostatic adsorption and *in situ* reduction to synthesize a Co-$Ti_3C_2T_x$ SAC for photocatalytic CO_2 reduction. Co-cations are initially adsorbed onto the negatively charged functional groups on the MXene surface during synthesis, forming ionic bonds facilitated by electrostatic attraction. The ionic bond formation is followed by reducing Co cations on the MXene, leading to covalent bonds between the metal atoms and surface-functional groups (–F and –O). Sodium borohydride was employed as a reducing agent for Co^{2+} ions and as an oxidation inhibitor of MXenes to overcome its fast oxidation.

Zhou *et al.*[248] designed and synthesized the MXene@Por-COF-Co heterostructure. The dispersed COF structures and exposed MXene nanosheets offer more accessible reactive sites and quicker ion transfer channels to the heterostructure because the covalent interactions between the aldehyde groups in the COF structures and the amino groups of MXene can facilitate the *in situ* formation of COFs on the surface of amino-functionalized MXene nanosheets. TEM images of MXene@-Por-COF-Co-7 reveal a homogeneous distribution of COF nanosheets across the surface of the MXene nanosheets. Furthermore, MXene@Por-COF-Co-7 exhibits a remarkable CO FE of 97.28% at −0.6 V, significantly higher than that of Por-COF-Co (0%) at the same potential. In addition, MXene@-Por-COF-Co-7 also maintains a high FE in the potential range of −0.5 to −1 V *vs.* RHE, suggesting its good selectivity for CO formation. The bias current density of CO increased with a rise in voltage.

Zhao *et al.*[260] employed self-reduction stabilization to anchor platinum (Pt) single atoms onto Ti vacancies of Ti_3C_2 for CO_2 activation with amines and silane, producing formamides. The single Pt atoms on the $Ti_{3-x}C_2T_y$ support exhibited
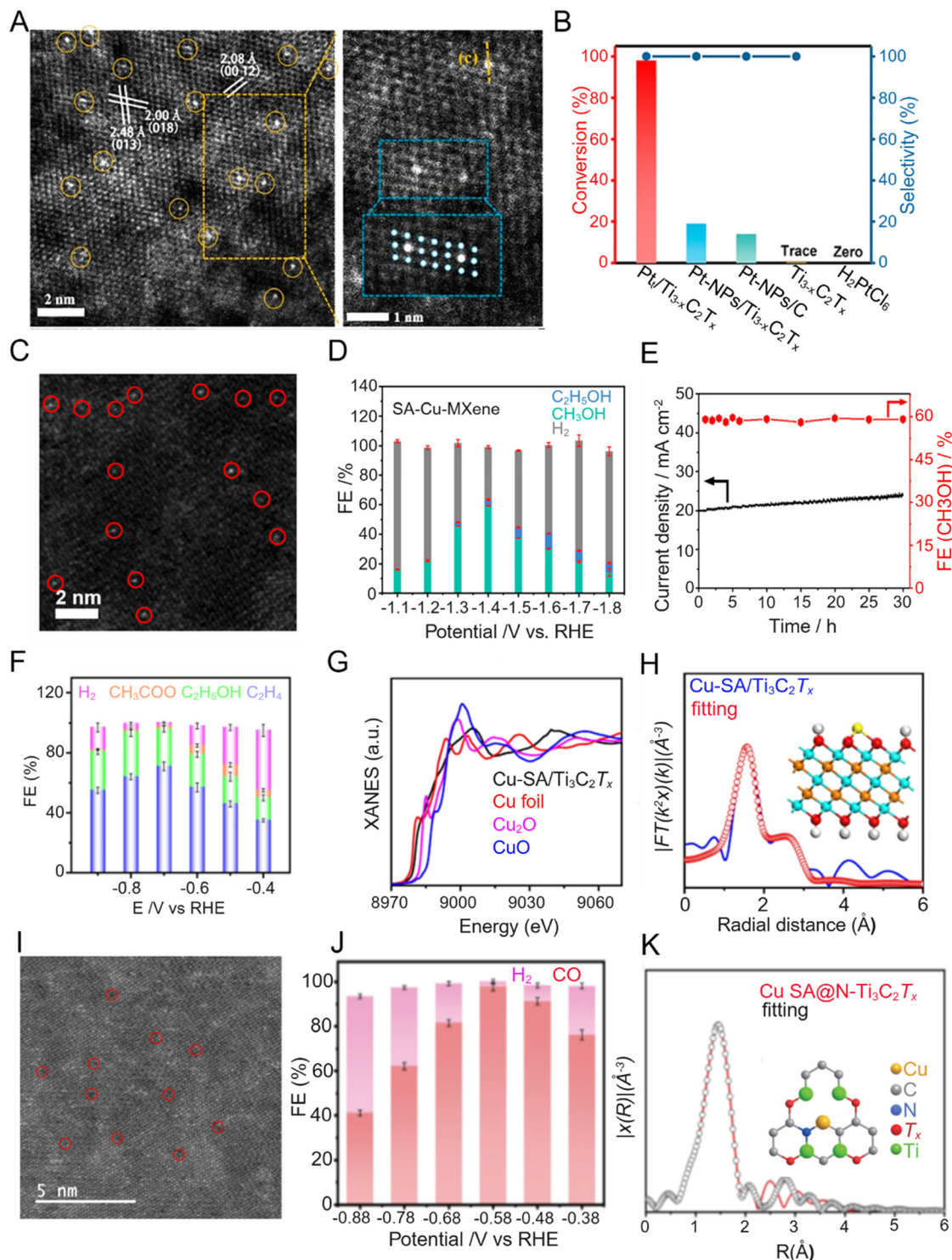
Fig. 10 (A) High-angle annular dark-field (HAADF) scanning transmission electron microscopy (STEM) image of Pt/Ti$_{3-x}$C$_2$T$_x$. (B) Catalytic performance of catalyst systems. (A) and (B) Reprinted with permission from *J. Am. Chem. Soc.* 2019, 141, 9, 4086–4093. Copyright [2019] American Chemical Society). (C) Aberration-corrected (AC) HAADF-STEM image of the SA-Cu-MXene. (D) Faradaic efficiency (FE) of product formation on the SA-Cu-MXene. (E) Current stability and corresponding FE for CH$_3$OH formation on the SA-Cu-MXene. (C)–(E) Reprinted with permission from *ACS Nano* 2021, 15, 3, 4927–4936. Copyright [2021] American Chemical Society). (F) FE of Cu-SA–Ti$_3$C$_2$T$_x$. (G) X-ray absorption near-edge structure spectra at the Cu K-edge with CuO, Cu$_2$O, and Cu foil as a reference. (H) Extended X-ray absorption fine structure (EXAFS) fitting curve of Cu-SA/Ti$_3$C$_2$T$_x$; inset illustrates the Cu-SA–Ti$_3$C$_2$T$_x$ structure. Yellow, blue, dark yellow, red, and white balls represent Cu, Ti, C, O, and H, respectively. (F)–(H) Reproduced from ref. 261 with permission from Springer Nature, Copyright [2021]). (I) AC HAADF-STEM of Ti$_3$C$_2$T$_x$ demonstrating Ti vacancies.[262] (J) Potential-dependent FE of H$_2$ and CO on Cu SA@N-Ti$_3$C$_2$T$_x$ at applied potentials. (K) EXAFS fitting of Cu SA@N-Ti$_3$C$_2$T$_x$; inset presents the atomic interface structure model. (I)–(K) Reproduced from ref. 262 with permission from Springer Nature, Copyright [2024]).

partial positive charges and atomic dispersion. Adsorbing and reducing Pt^{4+} simultaneously were successful without adding a reductant. Moreover, HAADF imaging revealed that the Pt single atoms were anchored at the Ti site in Ti_3C_2 rather than at the lattice gap (Fig. 10A). These Ti vacancies strongly correlate with the etching conditions during MXene synthesis, especially the etchant. Fig. 10B reveals that $Pt_1/Ti_{3-x}C_2T_y$ SAC displayed superior catalytic performance for converting CO_2 compared to that of Pt nanoparticles (NPs).

Zhao et al.[106] developed single-atom Cu loaded on MXene layers by selectively etching Al layers from quaternary MAX phases $[Ti_3(Al_{1-x}Cu_x)C_2]$ for CH_3OH synthesis, applying easy sublimation of $AlCl_3$ and leaving unreacted Cu on the MXene. The improved selectivity for CH_3OH arises from the capacity of atomically dispersed Cu sites to impede the C–C coupling of *CO, facilitating the formation of CH_3OH (Fig. 10C). This coordination lowers the energy barrier for converting HCOOH* into an absorbed CHO* intermediate, enhancing electrocatalytic activity for CO_2 conversion. The SA-Cu–MXene catalyst exhibited an increased FE of 59.1% for CH_3OH production with high stability and a low energy barrier for the rate-determining step (HCOOH* to CHO*; Fig. 10D and E).

Bao et al.[261] synthesized a Cu SAC anchored on $Ti_3C_2T_x$ nanosheets via chemical reduction, followed by freeze-drying. The resulting Cu-NP/$Ti_3C_2T_x$ SAC reduced CO well, achieving over 98% selectivity toward C_{2+} products with a high C_2H_4 selectivity of 71% (Fig. 10F). The catalyst promotes the formation of the *CO–CHO intermediate, facilitating C–C coupling. The XANES analysis revealed that the Cu valence state in the Cu-NP/$Ti_3C_2T_x$ SAC lies between that of metallic Cu and Cu^+, indicating the presence of O coordination and formation of $Cu–O_3$ species (Fig. 10G and H).

Similarly, Liu et al.[262] reported a monoatomic Cu catalyst featuring $Cu–N_1C_1$ coordination anchored on the N-doped $Ti_3C_2T_x$ MXene for the efficient CO_2 reduction to CO. This catalyst achieved over 97% selectivity toward CO at an applied potential of -0.58 V vs. RHE (Fig. 10J). The excellent performance was attributed to a potential-dependent valence transition of the Cu species. Aberration-corrected HAADF imaging indicated a high density of Ti vacancies in the MXene lattice, serving as preferential anchoring sites for immobilizing isolated Cu atoms (Fig. 10I). The XANES analysis revealed a negative shift in the Cu absorption edge relative to the pristine $Ti_3C_2T_x$, which is indicative of strong electronic interactions between Cu single atoms and the MXene support (Fig. 10K).

In developing SACs, a primary consideration is their stability because several factors, such as decomposition, dissolution, and atom migration, can promote cluster formation and morphological degradation. The high surface energy and mobility of isolated atoms drive these transformations.[263] Instability of SACs often results in diminished current density and FE.[264,265] Although many studies on MXene-based SACs for the CO_2RR have emphasized activity and selectivity, the stability of the single atoms under reaction conditions remains underexplored.

Future investigations should prioritize evaluating catalyst stability by conducting detailed post-reaction analyses. Such efforts could provide crucial insight into the structural and chemical evolution of catalysts, facilitating the rational design of MXene–single-atom interactions for enhanced catalytic activity, durability, and selectivity.

DFT has been pivotal in advancing 2D material-based electrocatalysis by predicting performance under several atomic configurations.[82,266,267] This theory has been critical in developing SAC-supported 2D material-based electrocatalysts. Numerous studies have employed the DFT to design SAC-MXene-based catalysts for the CO_2RR. For instance, Li et al.[258] demonstrated the high catalytic activity of single-atom scandium (Sc), Ti, and V-supported Ti_2CN_2 to produce CO with a low overpotential of 0.37, 0.27, and 0.23 eV, respectively. In contrast, Mn and Fe supported on Ti_2CN_2 primarily produce HCOOH with a low overpotential of 0.32 and 0.43 eV. The high catalytic activity of single atoms on Ti_2CN_2 can be attributed to N-functionalization, stabilizing SACs effectively by anchoring TM atoms. This functionalization also lowers the energy barrier for CO_2 reduction and improves catalytic selectivity. These SACs on Ti_2CN_2 exhibit high catalytic activity with much lower overpotentials.

Similarly, Athawale et al.[234] explored the feasibility of MXenes serving as an anchoring site for isolating TM SACs for the CO_2RR. Several SAC systems containing 3d (Sc, Ti, V, Cr, and Mn), 4d (yttrium [Y], zirconium [Zr], niobium [Nb], and Mo), and 5d (hafnium [Hf]) transition metals, supported on an O-terminated MXene (TM@Ti_2CO_2), were designed using DFT calculations. The findings indicate that TMs anchored on top of the C atom of Ti_2CO_2 (hollow-C site) present the most stable configuration. The hollow-C site, primarily for Nb, Mo, Zr, V, Cr, and Ti atoms, exhibits the most negative E_b values, indicating higher stability and better suitability for the CO_2RR.

5.5. MXene–metal/metal-oxide hybrids

Metal and metal oxide (MMO) catalysts have demonstrated notable potential in the CO_2RR; however, their application is often limited by intrinsic drawbacks such as low electrical conductivity, poor long-term stability, and limited product selectivity.[268–270] To overcome these challenges, use of hybrid electrocatalysts that integrate MMOs with conductive and chemically tunable materials, such as MXenes, have emerged as an effective strategy.[271–273] MXenes offer high electrical conductivity, a two-dimensional architecture, and versatile surface terminations, collectively making them ideal supports for enhancing the performance of MMO-based systems. The integration of MMOs with MXenes generates synergistic interfacial interactions that modulate the electronic structure of active sites, improve charge transport, and promote favorable binding of CO_2RR intermediates. Specifically, the surface terminations of MXenes (e.g., –O, –OH, and –F) can attract metal cations from the MMO phase and facilitate oxygen vacancy formation at the interface, enhancing catalytic activity and electron transfer efficiency.[224,234,274] These vacancies serve as additional active sites and improve the adsorption and activation of CO_2 molecules. For example, Wu et al.[232] developed an Fe_2O_3@MXene hybrid photocatalyst in which the introduction of $Ti_3C_2T_x$ increased oxygen vacancy concentration and formed Fe–O–Ti

bonds at the interface. These interfacial sites enhanced *COOH intermediate formation and improved CO production. Although this system was used for photocatalytic CO_2 reduction, the findings highlighted the general importance of MXene–MMO synergy, which is also transferable to electrocatalytic applications.[41,232,275]

In the electrocatalytic domain, Liu *et al.*[276] reported a hybrid composed of TiO_2 and SnO_2 nanowires self-assembled onto the Ti_3C_2 MXene *via* van der Waals interactions. The MXene suppressed MMO aggregation provided efficient electron

pathways and improved structural integrity. This integration enhanced CO_2 adsorption and activation, significantly improving CO_2RR activity.[277]

Hao *et al.*[224] fabricated an Ag–ZnO/$Ti_3C_2T_x$ hybrid catalyst *via* a cation exchange and self-assembly method—the MXene-regulated interface featured undercoordinated sites and mesoporous nanostructures. The catalyst achieved nearly 100% CO FE and a partial current density of 22.59 mA cm^{-2} at -0.87 V *vs.* RHE (Fig. 11A). DFT calculations confirmed that MXene addition shifted the d-band center, enhanced *COOH binding, and
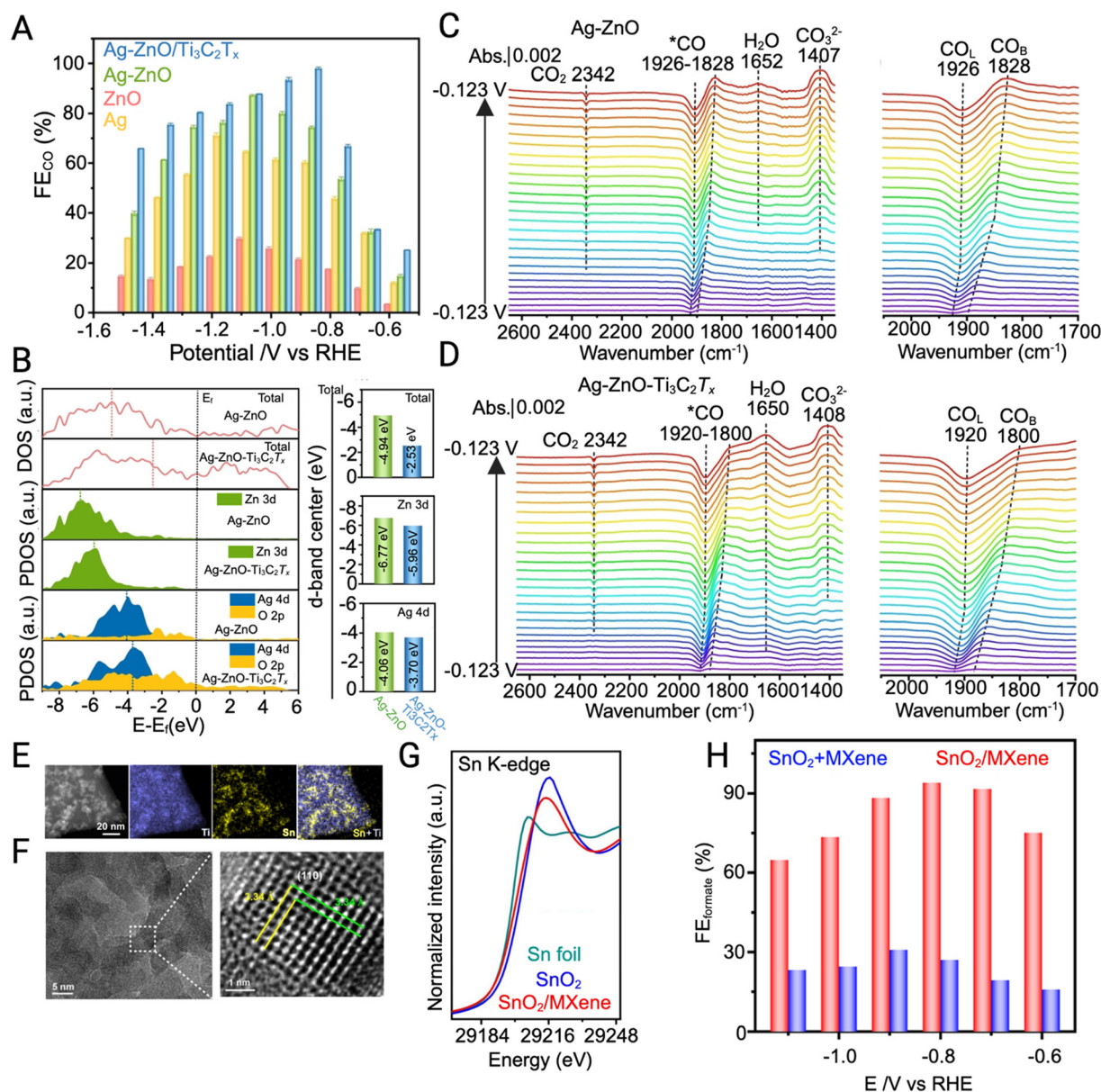

Fig. 11 (A) Faradaic efficiency (FE) of CO on Ag–ZnO–$Ti_3C_2T_x$. (B) Density of states (DOS) for Zn 3d, Ag 4d, and O 2p orbitals of Ag–ZnO and Ag–ZnO/$Ti_3C_2T_x$ (left pane) and the corresponding d-band center (right pane). (C) and (D) *In situ* attenuated total reflectance infrared spectra while stepping the potential from -0.123 to -1.423 V on (C) Ag–ZnO and D) Ag–ZnO/$Ti_3C_2T_x$. (A)–(D) Reproduced from ref. 224 with permission from Wiley and Sons, Copyright [2023]. (E) Low-magnification high-angle annular dark-field scanning transmission electron microscopy image and corresponding electron-dispersive spectroscopy element images of SnO_2/MXene. (F) High-resolution transmission electron microscopy image and lattice plane. (G) Sn K-edge X-ray absorption near-edge structure spectra of the SnO_2/MXene catalyst, Sn foil, and SnO_2 references. (H) Potential-dependent FE of formate. (E)–(H) Reproduced from ref. 121 with permission from PNAS, Copyright [2022].

lowered the energy barrier for intermediate formation (Fig. 11B). *In situ* attenuated total reflectance infrared spectroscopy offered valuable insight into the reaction intermediates, elucidating the origin of CO selectivity (Fig. 11C and D). Within the applied potential window of −0.123 to −1.423 V, the attenuated total reflectance infrared spectra revealed characteristic signals corresponding to CO_2, CO_3^{2-}, and adsorbed *CO species. The *CO bands exhibited a bipolar profile, indicative of Fano line shape modulation. For the Ag–ZnO/$Ti_3C_2T_x$ catalyst, the inverted band observed at 1920 cm^{-1} was attributed to linearly bonded CO (CO_L), whereas the positive band at 1800 cm^{-1} was assigned to bridge-bonded CO (CO_B). These observations suggest that forming *CO intermediates from CO_2 is more favorable on Ag–ZnO/$Ti_3C_2T_x$ than on Ag–ZnO. DFT revealed that adding the MXene facilitated stronger binding abilities of *COOH compared to Ag–ZnO. Moreover, the MXene regulated the Ag–ZnO interface by reducing the electron filling of antibinding sites and optimizing the electronic structure by lowering the formation energy barrier of the intermediate.

Similarly, Cao *et al.*[232] reported a ZnO/N–$Ti_3C_2T_x$ catalyst that achieved an FE exceeding 96% for CO production. ZnO provided the primary active sites for CO_2 conversion, while the N-doped MXene improved textural properties and conductivity, facilitating PCET. Similarly, SnO_2 quantum dots grown on ultrathin $Ti_3C_2T_x$ MXene sheets (*via* hydrothermal synthesis) delivered a 94% FE and a partial current density of 57.8 mA cm^{-2} for formate production. *In situ* XANES measurements revealed that SnO_2 was partially reduced to metallic Sn during operation, which acted as the true catalytic site. Coordination environment changes observed *via* EXAFS confirmed strong Sn–Ti interfacial coupling unique to the MXene-based hybrid (Fig. 11F–H).[121] In addition, the absorption edge position of the Sn K-edge XANES spectrum of the SnO_2/MXene is situated between that of metallic Sn foil (Sn^0) and SnO_2 (Sn^{4+}; Fig. 11G). The extended X-ray absorption fine structure spectra of SnO_2/MXene in the *R*-space and *K*-space differ from those of pure SnO_2, suggesting that the local coordination environment of Sn in SnO_2/MXene is unlike that in pristine SnO_2.

In a similar study, Yu *et al.*[210] synthesized a TiO_2/Ti_3C_2 MXene photocatalyst *via* thermal calcination. By adjusting the temperature (350–650 °C), TiO_2 nanoparticle loading was modulated, influencing CH_4 production. Though photocatalysis, this system again underscores the broader relevance of MXene–MMO interactions across catalytic modalities.

Recently, a Cu_2O/MXene 0D/2D hybrid catalyst demonstrated excellent selectivity for propane (C_3H_8) production at −1.3 V *vs.* RHE.[278] The interface between Cu_2O and the MXene created cooperative binding sites; the MXene favored *CO adsorption while Cu_2O stabilized *C_2 intermediates, facilitating C–C–C coupling and efficient hydrogenation to C_3 products. This hybrid highlights the unique potential of MXene–MMO heterostructures in enabling multicarbon product formation, which is rarely achieved using either component alone. These examples illustrate how electronic coupling, vacancy engineering, and interfacial coordination at the MXene–MMO boundary promote enhanced CO_2 adsorption, intermediate stabilization

(*e.g.*, *COOH and *CHO), and improved selectivity. Moreover, MXenes can help suppress competing hydrogen evolution reactions due to their hydrophilicity and binding site modulation, thereby further enhancing CO_2RR selectivity. Future work should focus on understanding how the oxidation states, vacancy density, and structural morphology of MXenes and MMOs evolve under electrochemical operating conditions, and how these changes influence catalytic stability and product distribution. In particular, quantifying the role of MXenes in HER suppression and tailoring interfaces for selective multi-electron/multicarbon pathways are promising directions for designing next-generation MXene-based hybrid electrocatalysts.

6. Challenges and outlook

MXene-based electrocatalysts show exceptional promise for the electrochemical reduction of CO_2 due to their high conductivity, tunable surface chemistry, and structural versatility. Despite significant progress, several interconnected challenges must be addressed to transition these materials from fundamental research to practical, large-scale implementation. A key challenge is balancing catalytic activity, selectivity, and energy efficiency, particularly the selective formation of higher-value multicarbon products such as ethylene, ethanol, and propanol. Currently, MXenes predominantly yield simpler products like CO and formate due to limitations in intermediate stabilization and the competing HER. Future strategies involving advanced surface engineering, controlled doping, and precise defect management are essential to overcome these scaling limitations and direct reaction pathways toward desired multicarbon products.

Beyond intrinsic catalyst design, the practical implementation of MXene-based electrocatalysts is significantly influenced by reactor-level constraints inherent to industrial electrolyzer systems (as discussed in Section 2.1). Industrial electrolyzers require operation under stringent conditions, including continuous high current densities (>200 mA cm^{-2}), efficient heat and water management, effective control of CO_2 crossover, and stable long-term performance. Traditional laboratory-scale H-cell reactors, which dominate fundamental studies, fail to replicate these conditions due to inherent limitations such as low CO_2 solubility (∼34 mM), diffusion-controlled mass transport, large electrode spacing, and dilute electrolytes, resulting in low achievable current densities (<100 mA cm^{-2}). Consequently, performance metrics derived from H-cells rarely translate effectively to industrial-scale systems. These reactor designs significantly enhance CO_2 transport through direct gas-phase delivery, minimize ohmic losses, control reaction interfaces more effectively, and offer improved electrolyte management, addressing many limitations of conventional H-cell setups.

Nevertheless, a lack of standardized evaluation protocols hinders widespread adoption and advancement in the MXene-based CO_2RR. Variations in cell designs, electrode materials, electrolyte compositions, gas flow conditions, and performance metrics currently impede meaningful comparison between

studies. Establishing community-wide benchmarking guidelines and uniform testing standards will enhance performance evaluation reproducibility, transparency, and reliability.

Moreover, the catalytic performance of MXenes remains closely tied to their synthesis routes, which influence structural characteristics such as flake size, surface termination chemistry (–O, –OH, –F), and defect density. Oxygen-terminated MXenes have demonstrated promising catalytic properties by lowering reaction barriers and stabilizing critical reaction intermediates. However, achieving reproducible and controlled termination profiles is challenging. To address this, scalable, cost-effective, and precisely controllable synthesis methods must be developed. Additionally, defect engineering and doping offer strategic routes to optimize the catalytic properties of MXenes. Introducing oxygen vacancies or doping with heteroatoms (N, P, or transition metals) can modify the electronic structure, enhance active site densities, and tune intermediate binding energies. However, excessive defects may negatively affect structural stability and induce undesired side reactions. Therefore, careful optimization and systematic evaluation of doping strategies under realistic electrochemical conditions are necessary.

Significant gaps remain between computational predictions and experimental outcomes. Many theoretical studies utilize idealized MXene structures without realistic surface heterogeneities and defects. Experimentally synthesized MXenes typically feature mixed terminations, variable flake sizes, and structural imperfections. Future theoretical efforts should incorporate realistic structural models that account for these variations to enhance predictive accuracy, thereby more effectively guiding experimental development.

Currently, most experimental CO_2RR studies focus on $Ti_3C_2T_x$ MXenes. Exploring under-investigated MXene compositions such as Mo_2CT_x, Nb_2CT_x, and V_2CT_x could uncover unique catalytic properties, improved stability, and enhanced activity. Leveraging machine learning and high-throughput computational screening methods may accelerate the discovery of promising MXene candidates and guide targeted experimental validation.

The operational stability of MXenes under realistic electrochemical conditions remains relatively unexplored. Prolonged exposure to negative potentials, variable pH environments, and continuous gas flow can induce oxidation, structural deformation, and changes in surface termination composition. To address this, in situ and operando characterization techniques such as transmission electron microscopy (TEM), X-ray absorption spectroscopy (XAS), and Raman spectroscopy should be employed to monitor catalyst evolution under reaction conditions. Such insights are crucial for designing MXenes with enhanced durability and reliable long-term performance. Finally, emerging fabrication technologies, particularly additive manufacturing and 3D printing, offer novel opportunities for transitioning MXene catalysts into practical, scalable electrode architectures. Printable MXene inks, already successfully demonstrated in energy storage and electronics, could facilitate customized, high-surface-area electrode designs, enhancing

mass transport and reaction interface stability. Combining MXenes with complementary materials through advanced printing techniques further opens new possibilities for scalable integration into commercial CO_2RR systems. In summary, the successful industrial deployment of MXene-based electrocatalysts for the CO_2RR demands a comprehensive approach that integrates advanced material synthesis and surface engineering, optimized reactor design, standardized evaluation methods, and scalable fabrication techniques.

6.1. Economic viability and cost reduction

While MXenes offer significant advantages of catalytic performance, tunability, and selectivity, their current production costs remain a nontrivial challenge for commercial adoption. Laboratory-scale synthesis protocols, often involving high-purity MAX-phase precursors, hazardous etching agents (e.g., HF or LiF/HCl), and multi-step purification, contribute to relatively high per-gram costs, often ranging from 100 to 1000 USD, depending on scale and quality. However, recent advances in scalable and safer synthesis actively address this limitation. Alternative fluoride-free etching strategies, including electrochemical, alkaline, and molten-salt routes, eliminate the need for hazardous chemicals while improving yield and environmental safety. Continuous-flow production methods have demonstrated multi-gram scale fabrication with excellent reproducibility and are being increasingly optimized for cost-effectiveness. For example, Anasori et al.[41] conducted a life-cycle analysis demonstrating reduced environmental and financial costs when replacing HF-based synthesis with alternative etching processes. Another critical factor in cost reduction lies in material efficiency. Due to their high intrinsic conductivity and activity, MXenes often require lower loadings to achieve catalytic performance than conventional catalysts. In hybrid systems, such as MXene–metal oxide composites or single-atom-doped MXenes, the synergy between active sites allows for minimized MXene usage while maintaining or enhancing selectivity and stability. Long-term durability further enhances economic feasibility. Stable MXene-based catalysts reduce the need for frequent replacement, lowering operational expenses over extended use cycles. Moreover, enhanced selectivity for high-value CO_2RR products, such as C_{2+} compounds, increases the overall value of the catalytic process. As interest grows, industrial integration and shared manufacturing infrastructure (e.g., with battery or supercapacitor industries) may further lower precursor costs and streamline production. Techno-economic assessments of MXene-based membrane electrode assemblies (MEAs) and gas-diffusion electrodes (GDEs) are beginning to demonstrate promising cost-performance trade-offs at the device level. Finally, it's worth mentioning that while $Ti_3C_2T_x$ MXenes currently cost approximately 20–100 USD per g, this is still considerably lower than that of noble-metal catalysts (e.g., Pt/C at ∼156 USD per g) besides, MXenes offer additional value through superior tunability, conductivity, and durability. In conclusion, although MXenes are currently more expensive than traditional transition-metal-based electrocatalysts, ongoing innovations in synthesis, material design, and system

integration are rapidly closing the gap. With continued improvements in low-cost, scalable production methods, reduced catalyst loading requirements, and enhanced operational lifetimes, MXene-based materials are increasingly positioned as cost-effective and high-performance candidates for the industrial CO_2RR.

Conflicts of interest

There are no conflicts to declare.

Data availability

The data will be available upon request to the authors.

Acknowledgements

References

1 X. Q. Tan, W. Mo, X. Lin, J. Y. Loh, A. R. Mohamed and W. J. Ong, *Nanoscale*, 2023, **15**, 6536–6562.

2 L. J. R. Nunes, *Environments*, 2023, **10**(4), 66.

3 K. Wang, M. A. Rehman, S. Fahad and Z. Linzhao, *Resour. Policy*, 2023, **81**, 103384.

4 Z. K. Dijoo and R. Khurshid, *Environ. Biotechnol.*, 2022, 39–56.

5 S. Fang, M. Rahaman, J. Bharti, E. Reisner, M. Robert, G. A. Ozin and Y. H. Hu, *Nat. Rev. Methods Primers*, 2023, **3**, 1–21.

6 A. S. Joel and Y. M. Isa, *J. Chem. Technol. Biotechnol.*, 2023, **98**, 838–855.

7 H. Lee and J. Romero, Core Writing Team, IPCC, Climate Change 2023: Synthesis Report – Summary for Policymakers, *Intergovernmental Panel on Climate Change*, Geneva, Switzerland, 2023, p. SPM–5, DOI: **10.59327/IPCC/AR6-9789291691647.001**.

8 T. M. Gür, *Prog. Energy Combust. Sci.*, 2022, **89**, 100965.

9 T. Patil, S. Dharaskar, M. Sinha and S. S. Jampa, *Environ. Sci. Pollut. Res.*, 2022, **29**, 35723–35745.

10 N. Shreyash, M. Sonker, S. Bajpai, S. K. Tiwary, M. A. Khan, S. Raj, T. Sharma and S. Biswas, *Energies*, 2021, **14**, 4978.

11 V. Kumaravel, J. Bartlett and S. C. Pillai, *ACS Energy Lett.*, 2020, 486–519.

12 M. Ozkan and R. Custelcean, *MRS Bull.*, 2022, **47**, 390–394.

13 J. A. Garcia, M. Villen-Guzman, J. M. Rodriguez-Maroto and J. M. Paz-Garcia, *J. Environ. Chem. Eng.*, 2022, **10**, 108470.

14 Y. Zhang, L. Yu, K. Cui, H. Wang and T. Fu, *Chem. Eng. J.*, 2023, **455**, 140552.

15 R. Shaw and S. Mukherjee, *Carbon Capture Sci. Technol.*, 2022, **2**, 100036.

16 W. J. Lee, C. Li, H. Prajitno, J. Yoo, J. Patel, Y. Yang and S. Lim, *Catal. Today*, 2021, **368**, 2–19.

17 K. Fernández-Caso, G. Díaz-Sainz, M. Alvarez-Guerra and A. Irabien, *ACS Energy Lett.*, 2023, **8**, 1992–2024.

18 S. Fang, M. Rahaman, J. Bharti, E. Reisner, M. Robert, G. A. Ozin and Y. H. Hu, *Nat. Rev. Methods Primers*, 2023, **3**, 1–21.

19 C. Song, Z. Wang, Z. Yin, D. Xiao and D. Ma, *Chem. Catal.*, 2022, **2**, 52–83.

20 J. Zhou, H. Liu and H. Wang, *Chin. Chem. Lett.*, 2023, **34**, 107420.

21 S. Zong, A. Chen, M. Wiśniewski, L. Macheli, L. L. Jewell, D. Hildebrandt and X. Liu, *Carbon Capture Sci. Technol.*, 2023, **8**, 100133.

22 Z. Masoumi, M. Tayebi, M. Tayebi, S. A. Masoumi Lari, N. Sewwandi, B. Seo, C. S. Lim, H. G. Kim and D. Kyung, *Int. J. Mol. Sci.*, 2023, **24**, 9952.

23 Z. Chen, X. Wang, J. P. Mills, C. Du, J. Kim, J. Wen and Y. A. Wu, *Nanoscale*, 2021, **13**, 19712–19739.

24 M. Salehi, H. Al-Mahayni, A. Farzi, M. McKee, S. Kaviani, E. Pajootan, R. Lin, N. Kornienko and A. Seifitokaldani, *Appl. Catal., B*, 2024, **353**, 124061.

25 M. Li, S. Garg, X. Chang, L. Ge, L. Li, M. Konarova, T. E. Rufford, V. Rudolph and G. Wang, *Small Methods*, 2020, **4**, 2000033.

26 Z. Wang, Y. Zhou, P. Qiu, C. Xia, W. Fang, J. Jin, L. Huang, P. Deng, Y. Su, R. Crespo-Otero, X. Tian, B. You, W. Guo, D. Di Tommaso, Y. Pang, S. Ding and B. Y. Xia, *Adv. Mater.*, 2023, **35**, 2303052.

27 L. Xiao, Q. Zheng, S. Luo, Y. Ying, R. Zhou, S. Zhou, X. Li, X. Ye, Z. Yu, Q. Xu, H. Liao and J. Xu, *Sci. Adv.*, 2024, **10**, 2707.

28 C. Long, X. Liu, K. Wan, Y. Jiang, P. An, C. Yang, G. Wu, W. Wang, J. Guo, L. Li, K. Pang, Q. Li, C. Cui, S. Liu, T. Tan and Z. Tang, *Sci. Adv.*, 2023, **9**(43), 6119.

29 B. Peng, H. She, Z. Wei, Z. Sun, Z. Deng, Z. Sun and W. Chen, *Nat. Commun.*, 2025, **16**, 1–11.

30 W. Ma, S. Xie, T. Liu, Q. Fan, J. Ye, F. Sun, Z. Jiang, Q. Zhang, J. Cheng and Y. Wang, *Nat. Catal.*, 2020, **3**, 478–487.

31 L. Fan, F. Li, T. Liu, J. E. Huang, R. K. Miao, Y. Yan, S. Feng, C. W. Tai, S. F. Hung, H. J. Tsai, M. C. Chen, Y. Bai, D. Kim, S. Park, P. Papangelakis, C. Wu, A. Shayesteh Zeraati, R. Dorakhan, L. Sun, D. Sinton and E. Sargent, *Nat. Synth.*, 2024, **4**, 262–270.

32 H. Bin Yang, S. F. Hung, S. Liu, K. Yuan, S. Miao, L. Zhang, X. Huang, H. Y. Wang, W. Cai, R. Chen, J. Gao, X. Yang, W. Chen, Y. Huang, H. M. Chen, C. M. Li, T. Zhang and B. Liu, *Nat. Energy*, 2018, **3**, 140–147.

33 A. D. Handoko, H. Chen, Y. Lum, Q. Zhang, B. Anasori and Z. W. Seh, *iScience*, 2020, **23**, 101181.

34 X. Qian, L. Li, Y. Li, Z. Liu, Z. Tian, C. Zhan and L. Chen, *Phys. Chem. Chem. Phys.*, 2021, **23**, 12431–12438.

35 Z. Li, Y. Wu, Z. Li and Y. Wu, *Small*, 2019, **15**, 1804736.

36 A. K. Worku, M. A. Alemu, D. W. Ayele, M. Z. Getie and M. A. Teshager, *Green Chem. Lett. Rev.*, 2024, **17**, 2325983.

37 B. Anasori and Y. Gogotsi, Introduction to 2D transition metal carbides and nitrides (MXenes), *2D Metal Carbides and Nitrides (MXenes): Structure, Properties and Applications*, Springer, 2019, pp. 3–12, DOI: 10.1007/978-3-030-19026-2_1.

38 H. M. A. Sharif, M. Rashad, I. Hussain, A. Abbas, O. F. Aldosari and C. Li, *Appl. Catal., B*, 2024, **344**, 123585.

39 T. Amrillah, A. R. Supandi, V. Puspasari, A. Hermawan and Z. W. Seh, *Trans. Tianjin Univ.*, 2022, **28**(4), 307–322.

40 J. Heo, N. Her, M. Jang, C. M. Park, A. Son, J. Han and Y. Yoon, *Crit. Rev. Environ. Sci. Technol.*, 2023, **53**(9), 987–1008.

41 W. Wang, J. Wu, X. Chen, X. Shen, X. Jin, Y. Sun, C. Yan, Y. Li and P. Zhang, *Chem. – Asian J.*, 2025, **20**, e202500086.

42 X. Q. Tan, W. Mo, X. Lin, J. Y. Loh, A. R. Mohamed and W. J. Ong, *Nanoscale*, 2023, **15**(14), 6536–6562.

43 B. Chang, H. Pang, F. Raziq, S. Wang, K. W. Huang, J. Ye and H. Zhang, *Energy Environ. Sci.*, 2023, **16**, 4714–4758.

44 K. Chan, *Nat. Commun.*, 2020, **11**, 1–4.

45 J. Yu, J. Wang, Y. Ma, J. Zhou, Y. Wang, P. Lu, J. Yin, R. Ye, Z. Zhu, Z. Fan, J. Yu, J. Wang, Y. Ma, J. Zhou, Y. Wang, P. Lu, J. Yin, R. Ye, Z. Zhu, Z. Fan and Z. Fan Hong Kong Branch, *Adv. Funct. Mater.*, 2021, **31**, 2102151.

46 Y. Y. Birdja, E. Pérez-Gallent, M. C. Figueiredo, A. J. Göttle, F. Calle-Vallejo and M. T. M. Koper, *Nat. Energy*, 2019, **4**, 732–745.

47 W. Zhang, Y. Hu, L. Ma, G. Zhu, Y. Wang, X. Xue, R. Chen, S. Yang and Z. Jin, *Adv. Sci.*, 2018, **5**, 1700275.

48 X. Zhi, A. Vasileff, Y. Zheng, Y. Jiao and S. Z. Qiao, *Energy Environ. Sci.*, 2021, **14**, 3912–3930.

49 X. Zhi, A. Vasileff, Y. Zheng, Y. Jiao and S. Z. Qiao, *Energy Environ. Sci.*, 2021, **14**, 3912–3930.

50 R.-B. Song, W. Zhu, J. Fu, Y. Chen, L. Liu, J.-R. Zhang, Y. Lin, J.-J. Zhu, R.-B. Song, J. Fu, Y. Chen, L. Liu, J.-R. Zhang, J.-J. Zhu, W. Zhu and Y. Lin, *Adv. Mater.*, 2020, **32**, 1903796.

51 K. P. Kuhl, E. R. Cave, D. N. Abram and T. F. Jaramillo, *Energy Environ. Sci.*, 2012, **5**, 7050–7059.

52 X. Li, X. Wu, X. Lv, J. Wang and H. Bin Wu, *Chem. Catal.*, 2022, **2**, 262–291.

53 Y. Yang, J. Wang, Y. Shu, Y. Ji, H. Dong and Y. Li, *Phys. Chem. Chem. Phys.*, 2022, **24**(15), 8591–8603.

54 A. Ozden, F. P. García de Arquer, J. E. Huang, J. Wicks, J. Sisler, R. K. Miao, C. P. O'Brien, G. Lee, X. Wang, A. H. Ip, E. H. Sargent and D. Sinton, *Nat. Sustainability*, 2022, **5**, 563–573.

55 D. Wakerley, S. Lamaison, J. Wicks, A. Clemens, J. Feaster, D. Corral, S. A. Jaffer, A. Sarkar, M. Fontecave, E. B. Duoss, S. Baker, E. H. Sargent, T. F. Jaramillo and C. Hahn, *Nat. Energy*, 2022, **7**, 130–143.

56 B. Anasori and M. Naguib, *MRS Bull.*, 2023, **48**, 238–244.

57 A. D. Handoko, K. H. Khoo, T. L. Tan, H. Jin and Z. W. Seh, *J. Mater. Chem. A*, 2018, **6**, 21885–21890.

58 D. M. Feng, Y. P. Zhu, P. Chen and T. Y. Ma, *Catalysts*, 2017, **7**, 373.

59 J. He, N. J. J. Johnson, A. Huang and C. P. Berlinguette, *ChemSusChem*, 2018, **11**, 48–57.

60 G. Marcandalli, M. C. O. Monteiro, A. Goyal and M. T. M. Koper, *Acc. Chem. Res.*, 2022, **55**, 1900–1911.

61 Y. Kang, S. M. João, R. Lin, K. Liu, L. Zhu, J. Fu, W. C. Cheong, S. Lee, K. Frank, B. Nickel, M. Liu, J. Lischner and E. Cortés, *Nat. Commun.*, 2024, **15**, 1–13.

62 J.-J. Lv, R. Yin, L. Zhou, J. Li, R. Kikas, T. Xu, Z.-J. Wang, H. Jin, X. Wang and S. Wang, *Angew. Chem.*, 2022, **134**, e202207252.

63 C. D. Koolen, W. Luo and A. Züttel, *ACS Catal.*, 2023, **13**, 948–973.

64 B. Deng, M. Huang, X. Zhao, S. Mou and F. Dong, *ACS Catal.*, 2022, **12**, 331–362.

65 L. Dong, W. Ge, Y. Fan, W. Zhang, H. Jiang, Y. Zhao and C. Li, *AIChE J.*, 2024, **70**, e18271.

66 Y. J. Sa, C. W. Lee, S. Y. Lee, J. Na, U. Lee and Y. J. Hwang, *Chem. Soc. Rev.*, 2020, **49**, 6632–6665.

67 J. Hou, B. Xu and Q. Lu, *Nat. Commun.*, 2024, **15**, 1–10.

68 T. Luo, K. Liu, J. Fu, S. Chen, H. Li, H. Pan and M. Liu, *Adv. Energy Sustainability Res.*, 2023, **4**, 2200148.

69 R. Gholizadeh, M. Pavlin, M. Huš and B. Likozar, *ChemSusChem*, 2025, **18**, e202400898.

70 Y. Liu, Y. Song, L. Huang, J. Su, G. Li, Q. Zhang, Y. Xin, X. Cao, W. Guo, Y. Dou, M. He, T. Feng, Z. Jin and R. Ye, *ACS Nano*, 2024, **18**, 14020–14028.

71 X. Zhang, S. X. Guo, K. A. Gandionco, A. M. Bond and J. Zhang, *Mater. Today Adv.*, 2020, **7**, 100074.

72 B. Miao, T. Bashir, H. Zhang, T. Ali, S. Raza, D. He, Y. Liu and J. Bai, *Renewable Sustainable Energy Rev.*, 2024, **199**, 114506.

73 K. J. Harris, M. Bugnet, M. Naguib, M. W. Barsoum and G. R. Goward, *J. Phys. Chem. C*, 2015, **119**, 13713–13720.

74 Y. Cheng, X. Xu, Y. Li, Y. Zhang and Y. Song, *Comput. Mater. Sci.*, 2022, **202**, 110971.

75 C. Y. J. Lim, A. D. Handoko and Z. W. Seh, *Diamond Relat. Mater.*, 2022, **130**, 109461.

76 K. Eid, Q. Lu, S. Abdel-Azeim, A. Soliman, A. M. Abdullah, A. M. Abdelgwad, R. P. Forbes, K. I. Ozoemena, R. S. Varma and M. F. Shibl, *J. Mater. Chem. A*, 2022, **10**, 1965–1975.

77 Y. Li, Y. Chen, Z. Guo, C. Tang, B. Sa, N. Miao, J. Zhou and Z. Sun, *Chem. Eng. J.*, 2022, **429**, 132171.

78 Z. Xie, Q. Wang, R. Yang, J. Zhang, S. Ou, G. Ouyang, M. Li, J. Shi and Y. Tong, *Appl. Catal., B*, 2025, **362**, 124727.

79 Y. Zhang and Z. Cao, *J. Phys. Chem. C*, 2021, **125**, 13331–13342.

80 S. Lu, Y. Zhang, F. Lou and Z. Yu, *J. CO2 Util.*, 2022, **62**, 102069.

81 H. Bao, Y. Qiu, X. Peng, J. Wang, Y. Mi, S. Zhao, X. Liu, Y. Liu, R. Cao, L. Zhuo, J. Ren, J. Sun, J. Luo and X. Sun, *Nat. Commun.*, 2021, **12**, 1–9.

82 S. Cao, H. Chen, Y. Hu, J. Li, C. Yang, Z. Chen, S. Wei, S. Liu, Z. Wang, D. Sun and X. Lu, *Chem. Eng. J.*, 2023, **461**, 141936.

83 S. Krishnan, S. Marimuthu, M. K. Singh and D. K. Rai, *Energy Adv.*, 2023, **2**, 1166–1175.

84 Z. Otgonbayar, C. M. Yoon and W. C. Oh, *Chem. Eng. J.*, 2023, **464**, 142716.

85 D. Qu, X. Peng, Y. Mi, H. Bao, S. Zhao, X. Liu and J. Luo, *Nanoscale*, 2020, **12**, 17191–17195.

86 F. Zhang and A. C. Co, *Angew. Chem., Int. Ed.*, 2020, **59**, 1674–1681.

87 M. Dunwell, X. Yang, B. P. Setzler, J. Anibal, Y. Yan and B. Xu, *ACS Catal.*, 2018, **8**, 3999–4008.

88 A. S. Varela, M. Kroschel, T. Reier and P. Strasser, *Catal. Today*, 2016, **260**, 8–13.

89 X. Liu, P. Schlexer, J. Xiao, Y. Ji, L. Wang, R. B. Sandberg, M. Tang, K. S. Brown, H. Peng, S. Ringe, C. Hahn, T. F. Jaramillo, J. K. Nørskov and K. Chan, *Nat. Commun.*, 2019, **10**, 1–10.

90 J. Shen, R. Kortlever, R. Kas, Y. Y. Birdja, O. Diaz-Morales, Y. Kwon, I. Ledezma-Yanez, K. J. P. Schouten, G. Mul and M. T. M. Koper, *Nat. Commun.*, 2015, **6**, 1–8.

91 M. López, K. S. Exner, F. Viñes and F. Illas, *Adv. Theory Simul.*, 2023, **6**, 2200217.

92 G. Gao, A. P. O'Mullane and A. Du, *ACS Catal.*, 2017, **7**, 494–500.

93 L. R. Johnson, S. Sridhar, L. Zhang, K. D. Fredrickson, A. S. Raman, J. Jang, C. Leach, A. Padmanabhan, C. C. Price, N. C. Frey, A. Raizada, V. Rajaraman, S. A. Saiprasad, X. Tang and A. Vojvodic, *ACS Catal.*, 2020, **10**, 253–264.

94 L. D. Chen, M. Urushihara, K. Chan and J. K. Nørskov, *ACS Catal.*, 2016, **6**, 7133–7139.

95 M. R. Singh, Y. Kwon, Y. Lum, J. W. Ager and A. T. Bell, *J. Am. Chem. Soc.*, 2016, **138**, 13006–13012.

96 A. Murata and Y. Hori, *Bull. Chem. Soc. Jpn.*, 1991, **64**, 123–127.

97 S. Li, X. Dong, Y. Zhao, J. Mao, W. Chen, A. Chen, Y. Song, G. Li, Z. Jiang, W. Wei and Y. Sun, *Angew. Chem., Int. Ed.*, 2022, **61**, e202210432.

98 I. T. McCrum, S. A. Akhade and M. J. Janik, *Electrochim. Acta*, 2015, **173**, 302–309.

99 J. J. Masana, B. Peng, Z. Shuai, M. Qiu and Y. Yu, *J. Mater. Chem. A*, 2022, **10**, 1086–1104.

100 Y. J. Ko, J. Y. Kim, W. H. Lee, M. G. Kim, T. Y. Seong, J. Park, Y. J. Jeong, B. K. Min, W. S. Lee, D. K. Lee and H. S. Oh, *Nat. Commun.*, 2022, **13**, 1–9.

101 W. Ni, Y. Xue, X. Zang, C. Li, H. Wang, Z. Yang and Y. M. Yan, *ACS Nano*, 2020, **14**, 2014–2023.

102 D. Gao, F. Scholten and B. Roldan Cuenya, *ACS Catal.*, 2017, **7**, 5112–5120.

103 R. A. Vaia, A. Jawaid, A. Hassan, G. Neher, D. Nepal, R. Pachter, W. Joshua Kennedy and S. Ramakrishnan, *ACS Nano*, 2021, **15**, 2771–2777.

104 T. Zhang, L. Chang, X. Zhang, H. Wan, N. Liu, L. Zhou and X. Xiao, *Nat. Commun.*, 2022, **13**, 1–9.

105 Y. Li, H. Shao, Z. Lin, J. Lu, L. Liu, B. Duployer, P. O. Å. Persson, P. Eklund, L. Hultman, M. Li, K. Chen, X. H. Zha, S. Du, P. Rozier, Z. Chai, E. Raymundo-Piñero, P. L. Taberna, P. Simon and Q. Huang, *Nat. Mater.*, 2020, **19**, 894–899.

106 Q. Zhao, C. Zhang, R. Hu, Z. Du, J. Gu, Y. Cui, X. Chen, W. Xu, Z. Cheng, S. Li, B. Li, Y. Liu, W. Chen, C. Liu, J. Shang, L. Song and S. Yang, *ACS Nano*, 2021, **15**, 4927–4936.

107 A. Gennaro, A. A. Isse and E. Vianello, *J. Electroanal. Chem.*, 1990, **289**, 203–215.

108 A. D. Handoko, H. Chen, Y. Lum, Q. Zhang, B. Anasori and Z. W. Seh, *iScience*, 2020, **23**, 101181.

109 N. H. Attanayake, H. R. Banjade, A. C. Thenuwara, B. Anasori, Q. Yan and D. R. Strongin, *Chem. Commun.*, 2021, **57**, 1675–1678.

110 X. Liao, K. Zheng, G. Wang, Y. Yang, Y. Li and M. O. Coppens, *Ind. Eng. Chem. Res.*, 2022, **61**, 14364–14373.

111 Z. Lin, D. Barbara, P. L. Taberna, K. L. Van Aken, B. Anasori, Y. Gogotsi and P. Simon, *J. Power Sources*, 2016, **326**, 575–579.

112 Q. Fan, R. Zhao, M. Yi, P. Qi, C. Chai, H. Ying and J. Hao, *Chem. Eng. J.*, 2022, **428**, 131107.

113 Z. Wang, J. Chen, Y. Li, K. Dong and Y. Yu, *Phys. Chem. Chem. Phys.*, 2022, **24**, 5903–5913.

114 X. Sun, Y. Li, Y. Wang, Z. Liu, K. Dong and S. Zhang, *Langmuir*, 2024, **40**, 2220–2229.

115 Z. Gu, H. Shen, L. Shang, X. Lv, L. Qian, G. Zheng, Z. Gu, H. Shen, L. Shang, X. Lv, L. Qian and G. Zheng, *Small Methods*, 2018, **2**, 1800121.

116 H. Xie, T. Wang, J. Liang, Q. Li and S. Sun, *Nano Today*, 2018, **21**, 41–54.

117 X. Ma, Y. Zhang, T. Fan, D. Wei, Z. Huang, Z. Zhang, Z. Zhang, Y. Dong, Q. Hong, Z. Chen, X. Yi, X. Ma, T. Fan, D. Wei, Z. Huang, Q. Hong, X. Yi, Y. Zhang, Z. Zhang, Z. Chen and Y. Dong, *Adv. Funct. Mater.*, 2023, **33**, 2213145.

118 H. Luo, B. Li, J. G. Ma and P. Cheng, *Angew. Chem., Int. Ed.*, 2022, **61**, e202116736.

119 G. L. De Gregorio, T. Burdyny, A. Loiudice, P. Iyengar, W. A. Smith and R. Buonsanti, *ACS Catal.*, 2020, **10**, 4854–4862.

120 N. Li, X. Chen, W. J. Ong, D. R. Macfarlane, X. Zhao, A. K. Cheetham and C. Sun, *ACS Nano*, 2017, **11**, 10825–10833.

121 L. Han, X. Peng, H. T. Wang, P. Ou, Y. Mi, C. W. Pao, J. Zhou, J. Wang, X. Liu, W. F. Pong, J. Song, Z. Lin, J. Luo and H. L. Xin, *Proc. Natl. Acad. Sci. U. S. A.*, 2022, **119**, e2207326119.

122 B. Govindan, R. Madhu, M. Abu Haija, F. V. Kusmartsev and F. Banat, *Catalysts*, 2022, **12**, 1180.

123 J. Lin, Y. Zhang, P. Xu and L. Chen, *MRE*, 2023, **3**, 100194.

124 S. Varhade, A. Guruji, C. Singh, G. Cicero, M. García-Melchor, J. Helsen and D. Pant, *ChemElectroChem*, 2025, **12**, e202400512.

125 M. Gao, Y. Sun, K. Zhao, M. Zhang, X. Wang and W. Wang, *J. Environ. Chem. Eng.*, 2024, **12**, 111802.

126 Z. Han, Y. Chang, H. Liu, Y. Wei, S. Hao, M. Y. Cong, Y. Gao and J. Gao, *Adv. Energy Mater.*, 2025, 2501761.

127 M. Abdinejad, S. Subramanian, K. Motlagh, M. Noroozifar, S. Duangdangchote, I. Neporozhnii, D. Ripepi, D. Pinto, M. Li, K. Tang, J. Middelkoop, A. Urakawa, O. Voznyy,

H.-B. Kraatz, T. Burdyny, M. Abdinejad, S. Subramanian, D. Ripepi, D. Pinto, M. Li, J. Middelkoop, A. Urakawa, T. Burdyny, M. K. Motlagh, M. Noroozifar, S. Duangdangchote, I. Neporozhnii, K. Tang, O. Voznyy and H.-B. Kraatz, *Adv. Energy Mater.*, 2023, **13**, 2300402.

128 M. Krishnan, A. Vijayaprabhakaran and M. Kathiresan, *Nanoscale*, 2024, **16**, 16218–16226.

129 M. Naguib, M. W. Barsoum, Y. Gogotsi, M. Naguib, M. W. Barsoum, Y. Gogotsi and A. Y. J. Gogotsi, *Adv. Mater.*, 2021, **33**, 2103393.

130 R. Khaledialidusti, M. Khazaei, S. Khazaei and K. Ohno, *Nanoscale*, 2021, **13**, 7294–7307.

131 M. Dahlqvist, A. Petruhins, J. Lu, L. Hultman and J. Rosen, *ACS Nano*, 2018, **12**, 7761–7770.

132 A. Thakur, Y. Zhang, Y. Gogotsi and B. Anasori, *MRS Energy Sustain.*, 2025, 1–13.

133 C. E. Shuck, A. Sarycheva, M. Anayee, A. Levitt, Y. Zhu, S. Uzun, V. Balitskiy, V. Zahorodna, O. Gogotsi and Y. Gogotsi, *Adv. Eng. Mater.*, 2020, **22**, 1901241.

134 T. S. Mathis, K. Maleski, A. Goad, A. Sarycheva, M. Anayee, A. C. Foucher, K. Hantanasirisakul, C. E. Shuck, E. A. Stach and Y. Gogotsi, *ACS Nano*, 2021, **15**, 6420–6429.

135 J. Peng, X. Chen, W. J. Ong, X. Zhao and N. Li, *Chem*, 2019, **5**, 18–50.

136 P. P. Michałowski, M. Anayee, T. S. Mathis, S. Kozdra, A. Wójcik, K. Hantanasirisakul, I. Jóźwik, A. Piątkowska, M. Możdżonek, A. Malinowska, R. Diduszko, E. Wierzbicka and Y. Gogotsi, *Nat. Nanotechnol.*, 2022, **17**, 1192–1197.

137 C. E. Shuck, M. Han, K. Maleski, K. Hantanasirisakul, S. J. Kim, J. Choi, W. E. B. Reil and Y. Gogotsi, *ACS Appl. Nano Mater.*, 2019, **2**, 3368–3376.

138 M. Naguib, M. Kurtoglu, V. Presser, J. Lu, J. Niu, M. Heon, L. Hultman, Y. Gogotsi and M. W. Barsoum, *Adv. Mater.*, 2011, **23**, 4248–4253.

139 Y. J. Kim, S. J. Kim, D. Seo, Y. Chae, M. Anayee, Y. Lee, Y. Gogotsi, C. W. Ahn and H. T. Jung, *Chem. Mater.*, 2021, **33**, 6346–6355.

140 K. Hantanasirisakul, Y. Gogotsi, K. Y. Hantanasirisakul and A. J. Gogotsi, *Adv. Mater.*, 2018, **30**, 1804779.

141 J. L. Hart, K. Hantanasirisakul, A. C. Lang, B. Anasori, D. Pinto, Y. Pivak, J. T. van Omme, S. J. May, Y. Gogotsi and M. L. Taheri, *Nat. Commun.*, 2019, **10**, 1–10.

142 M. Anayee, N. Kurra, M. Alhabeb, M. Seredych, M. N. Hedhili, A. H. Emwas, H. N. Alshareef, B. Anasori and Y. Gogotsi, *Chem. Commun.*, 2020, **56**, 6090–6093.

143 N. Driscoll, A. G. Richardson, K. Maleski, B. Anasori, O. Adewole, P. Lelyukh, L. Escobedo, D. K. Cullen, T. H. Lucas, Y. Gogotsi and F. Vitale, *ACS Nano*, 2018, **12**, 10419–10429.

144 M. R. Lukatskaya, J. Halim, B. Dyatkin, M. Naguib, Y. S. Buranova, M. W. Barsoum, Y. Gogotsi, M. R. Lukatskaya, J. Halim, B. Dyatkin, M. Naguib, Y. S. Buranova, M. W. Barsoum and A. Y. J. Gogotsi, *Angew. Chem., Int. Ed.*, 2014, **53**, 4877–4880.

145 S. Y. Pang, Y. T. Wong, S. Yuan, Y. Liu, M. K. Tsang, Z. Yang, H. Huang, W. T. Wong and J. Hao, *J. Am. Chem. Soc.*, 2019, **141**, 9610–9616.

146 W. Sun, S. A. Shah, Y. Chen, Z. Tan, H. Gao, T. Habib, M. Radovic and M. J. Green, *J. Mater. Chem. A*, 2017, **5**, 21663–21668.

147 J. Chen, M. Chen, W. Zhou, X. Xu, B. Liu, W. Zhang and C. Wong, *ACS Nano*, 2022, **16**, 2461–2470.

148 M. Shen, W. Jiang, K. Liang, S. Zhao, R. Tang, L. Zhang and J. Q. Wang, *Angew. Chem. Int. Ed.*, 2021, **60**, 27013–27018.

149 L. Li, G. Li, L. Tan, Y. Zhang and B. Wu, *Langmuir*, 2017, **33**, 9000–9006.

150 T. Li, L. Yao, Q. Liu, J. Gu, R. Luo, J. Li, X. Yan, W. Wang, P. Liu, B. Chen, W. Zhang, W. Abbas, R. Naz and D. Zhang, *Angew. Chem., Int. Ed.*, 2018, **57**, 6115–6119.

151 M. Sun, A. Staykov and M. Yamauchi, *ACS Catal.*, 2022, **12**, 14856–14863.

152 M. Luo, Z. Wang, Y. C. Li, J. Li, F. Li, Y. Lum, D. H. Nam, B. Chen, J. Wicks, A. Xu, T. Zhuang, W. R. Leow, X. Wang, C. T. Dinh, Y. Wang, Y. Wang, D. Sinton and E. H. Sargent, *Nat. Commun.*, 2019, **10**, 1–7.

153 M. A. Z. G. Sial, M. Abbas, Z. M. Bhat, S. Ligani, M. Furquan, U. Alam, A. Hussain, X. Cai and M. Qamar, *Next Energy*, 2024, **4**, 100139.

154 M. Ghidiu, M. R. Lukatskaya, M. Q. Zhao, Y. Gogotsi and M. W. Barsoum, *Nature*, 2014, **516**, 78–81.

155 F. Liu, A. Zhou, J. Chen, J. Jia, W. Zhou, L. Wang and Q. Hu, *Appl. Surf. Sci.*, 2017, **416**, 781–789.

156 X. Wang, Y. Shi, J. Qiu, Z. Wang and R. Li, *Chem. Commun.*, 2023, **59**, 5063–5066.

157 M. Li, J. Lu, K. Luo, Y. Li, K. Chang, K. Chen, J. Zhou, J. Rosen, L. Hultman, P. Eklund, P. O. Å. Persson, S. Du, Z. Chai, Z. Huang and Q. Huang, *J. Am. Chem. Soc.*, 2019, **141**, 4730–4737.

158 Y. Li, H. Shao, Z. Lin, J. Lu, L. Liu, B. Duployer, P. O. Å. Persson, P. Eklund, L. Hultman, M. Li, K. Chen, X. H. Zha, S. Du, P. Rozier, Z. Chai, E. Raymundo-Piñero, P. L. Taberna, P. Simon and Q. Huang, *Nat. Mater.*, 2020, **19**, 894–899.

159 V. Kamysbayev, A. S. Filatov, H. Hu, X. Rui, F. Lagunas, D. Wang, R. F. Klie and D. V. Talapin, *Science*, 2020, **369**, 979–983.

160 D. Wang, C. Zhou, A. S. Filatov, W. Cho, F. Lagunas, M. Wang, S. Vaikuntanathan, C. Liu, R. F. Klie and D. V. Talapin, *Science*, 2023, **379**, 1242–1247.

161 M. Xiang, Z. Shen, J. Zheng, M. Song, Q. He, Y. Yang, J. Zhu, Y. Geng, F. Yue, Q. Dong, Y. Ge, R. Wang, J. Wei, W. Wang, H. Huang, H. Zhang, Q. Zhu and C. J. Zhang, *Innovation*, 2024, **5**, 100540.

162 L. Liu, E. Raymundo-Piñero, P. L. Taberna and P. Simon, *Electrochem. Commun.*, 2023, **148**, 107453.

163 C. Wang, H. Shou, S. Chen, S. Wei, Y. Lin, P. Zhang, Z. Liu, K. Zhu, X. Guo, X. Wu, P. M. Ajayan, L. Song, C. Wang, H. Shou, S. Chen, S. Wei, Y. Lin, P. Zhang, Z. Liu, K. Zhu, X. Guo, L. Song, X. Wu and P. M. Ajayan, *Adv. Mater.*, 2021, **33**, 2101015.

164 D. Chowdhury, S. Moolayadukkam, P. Datta and I. K. Puri, *J. Mater. Chem. B*, 2025, **13**(25), 7269–7279.

165 F. N. M. Azlan, M. A. A. M. Abdah, Y. S. Tan, M. N. Mustafa, R. Walvekar and M. Khalid, *J. Energy Storage*, 2023, **72**, 108620.

166 A. Numan, S. Rafique, M. Khalid, H. A. Zaharin, A. Radwan, N. A. Mokri, O. P. Ching and R. Walvekar, *Mater. Chem. Phys.*, 2022, **288**, 126429.

167 C. Xu, L. Wang, Z. Liu, L. Chen, J. Guo, N. Kang, X. L. Ma, H. M. Cheng and W. Ren, *Nat. Mater.*, 2015, **14**, 1135–1141.

168 S. Joshi, Q. Wang, A. Puntambekar and V. Chakrapani, *ACS Energy Lett.*, 2017, **2**, 1257–1262.

169 X. Xiao, H. Yu, H. Jin, M. Wu, Y. Fang, J. Sun, Z. Hu, T. Li, J. Wu, L. Huang, Y. Gogotsi and J. Zhou, *ACS Nano*, 2017, **11**, 2180–2186.

170 Z. Zhang, F. Zhang, H. Wang, C. Ho Chan, W. Lu and J. Y. Dai, *J. Mater. Chem. C*, 2017, **5**, 10822–10827.

171 A. Thakur, N. Chandran, K. Davidson, A. Bedford, H. Fang, Y. Im, V. Kanduri, B. C. Wyatt, S. K. Nemani, V. Poliukhova, R. Kumar, Z. Fakhraai and B. Anasori, *Small Methods*, 2023, **7**, 2300030.

172 Y. Wei, P. Zhang, R. A. Soomro, Q. Zhu, B. Xu, Y. Wei, P. Zhang, R. A. Soomro, Q. Zhu and B. Xu, *Adv. Mater.*, 2021, **33**, 2103148.

173 O. Mashtalir, M. Naguib, V. N. Mochalin, Y. Dall'Agnese, M. Heon, M. W. Barsoum and Y. Gogotsi, *Nat. Commun.*, 2013, **4**, 1–7.

174 M. Naguib, R. R. Unocic, B. L. Armstrong and J. Nanda, *Dalton Trans.*, 2015, **44**, 9353–9358.

175 F. Han, S. Luo, L. Xie, J. Zhu, W. Wei, X. Chen, F. Liu, W. Chen, J. Zhao, L. Dong, K. Yu, X. Zeng, F. Rao, L. Wang and Y. Huang, *ACS Appl. Mater. Interfaces*, 2019, **11**, 8443–8452.

176 K. Montazeri, H. Badr, K. Ngo, K. Sudhakar, T. Elmelegy, J. Uzarski, V. Natu and M. W. Barsoum, *J. Phys. Chem. C*, 2023, **127**, 10391–10397.

177 O. Mashtalir, M. R. Lukatskaya, M.-Q. Zhao, M. W. Barsoum, Y. Gogotsi, O. Mashtalir, M. R. Lukatskaya, M. Zhao, M. W. Barsoum and Y. Gogotsi, *Adv. Mater.*, 2015, **27**, 3501–3506.

178 T. Zhang, K. Shevchuk, R. J. Wang, H. Kim, J. Hourani and Y. Gogotsi, *Chem. Mater.*, 2024, **36**, 1998–2006.

179 L. Liu, M. Orbay, S. Luo, S. Duluard, H. Shao, J. Harmel, P. Rozier, P. L. Taberna and P. Simon, *ACS Nano*, 2022, **16**, 111–118.

180 M. Ghidiu, J. Halim, S. Kota, D. Bish, Y. Gogotsi and M. W. Barsoum, *Chem. Mater.*, 2016, **28**, 3507–3514.

181 H. Song, Y. Ma, Q. Yao, C. Liu, X. Li and X. Tao, *Chem. Eng. J.*, 2024, **491**, 151909.

182 D. D. Kruger, H. García and A. Primo, *Adv. Sci.*, 2024, **11**, 2307106.

183 Z. Zhang, Y. Ji, Q. Jiang and C. Xia, *Chem. Phys. Rev.*, 2024, **5**(3), 031301.

184 D. Gandla, Z. Zhuang, V. V. Jadhav and D. Q. Tan, *Energy Storage Mater.*, 2023, **63**, 102977.

185 X. Shi, Z. Yu, Z. Liu, N. Cao, L. Zhu, Y. Liu, K. Zhao, T. Shi, L. Yin and Z. Fan, *Angew. Chem.*, 2025, **137**, e202418420.

186 K. R. G. Lim, M. Shekhirev, B. C. Wyatt, B. Anasori, Y. Gogotsi and Z. W. Seh, *Nat. Synth.*, 2022, **1**, 601–614.

187 C. E. Shuck, A. Sarycheva, M. Anayee, A. Levitt, Y. Zhu, S. Uzun, V. Balitskiy, V. Zahorodna, O. Gogotsi and Y. Gogotsi, *Adv. Eng. Mater.*, 2020, **22**, 1901241.

188 M. Shekhirev, J. Busa, C. E. Shuck, A. Torres, S. Bagheri, A. Sinitskii and Y. Gogotsi, *ACS Nano*, 2022, **16**, 13695–13703.

189 P. D. Kolubah, H. O. Mohamed, A. R. Hari, Y. Ping, M. Ben Hassine, P. Dally, M. Obaid, X. Xu, J. K. El-Demellawi, P. E. Saikaly, M. Lanza, N. Ghaffour and P. Castaño, *Small*, 2024, 2406223.

190 W. Cao, J. Nie, Y. Cao, C. Gao, M. Wang, W. Wang, X. Lu, X. Ma and P. Zhong, *Chem. Eng. J.*, 2024, **496**, 154097.

191 G. Murali, J. K. Reddy Modigunta, Y. H. Park, J. H. Lee, J. Rawal, S. Y. Lee, I. In and S. J. Park, *ACS Nano*, 2022, **16**, 13370–13429.

192 C. Rong, T. Su, Z. Li, T. Chu, M. Zhu, Y. Yan, B. Zhang and F. Z. Xuan, *Nat. Commun.*, 2024, **15**, 1–8.

193 A. Lipatov, S. Bagheri and A. Sinitskii, *ACS Mater. Lett.*, 2024, **6**, 298–307.

194 Z. Ling, C. E. Ren, M. Q. Zhao, J. Yang, J. M. Giammarco, J. Qiu, M. W. Barsoum and Y. Gogotsi, *Proc. Natl. Acad. Sci. U. S. A.*, 2014, **111**, 16676–16681.

195 Y. Z. Zhang, J. K. El-Demellawi, Q. Jiang, G. Ge, H. Liang, K. Lee, X. Dong and H. N. Alshareef, *Chem. Soc. Rev.*, 2020, **49**, 7229–7251.

196 C. Rong, T. Su, Z. Li, T. Chu, M. Zhu, Y. Yan, B. Zhang and F.-Z. Xuan, *Nat. Commun.*, 2024, **15**, 1566.

197 A. Lipatov, H. Lu, M. Alhabeb, B. Anasori, A. Gruverman, Y. Gogotsi and A. Sinitskii, *Sci. Adv.*, 2018, **4**(6), eaat0491.

198 B. C. Wyatt, S. K. Nemani, K. Desai, H. Kaur, B. Zhang and B. Anasori, *J. Phys.: Condens. Matter*, 2021, **33**, 224002.

199 Y. Xie and P. R. C. Kent, *Phys. Rev. B: Condens. Matter Mater. Phys.*, 2013, **87**, 235441.

200 R. A. Soomro, P. Zhang, B. Fan, Y. Wei and B. Xu, *Nano-micro Lett.*, 2023, **15**, 1–18.

201 X. Liu, L. Yao, S. Zhang, C. Huang and W. Yang, *Inorg. Chem.*, 2024, **63**, 6305–6314.

202 K. Huang, P. Qu, Y. Wang, C. Lian, J. Li, H. Su and H. Liu, *Ind. Eng. Chem. Res.*, 2023, **62**, 20716–20726.

203 H. Chen, A. D. Handoko, T. Wang, J. Qu, J. Xiao, X. Liu, D. Legut, Z. Wei Seh and Q. Zhang, *ChemSusChem*, 2020, **13**, 5690–5698.

204 C. Y. J. Lim, A. D. Handoko and Z. W. Seh, *Diamond Relat. Mater.*, 2022, **130**, 109461.

205 H. Chen, A. D. Handoko, J. Xiao, X. Feng, Y. Fan, T. Wang, D. Legut, Z. W. Seh and Q. Zhang, *ACS Appl. Mater. Interfaces*, 2019, **11**, 36571–36579.

206 A. Parui, P. Srivastava and A. K. Singh, *ACS Appl. Mater. Interfaces*, 2022, **14**, 40913–40920.

207 L. Meng, L. K. Yan, F. Viñes and F. Illas, *J. Mater. Chem. A*, 2024, **12**, 7856–7874.

208 A. D. Handoko, K. D. Fredrickson, B. Anasori, K. W. Convey, L. R. Johnson, Y. Gogotsi, A. Vojvodic and Z. W. Seh, *ACS Appl. Energy Mater.*, 2018, **1**, 173–180.

209 A. D. Handoko, H. Chen, Y. Lum, Q. Zhang, B. Anasori and Z. W. Seh, *iScience*, 2020, **23**, 101181.

210 J. Low, L. Zhang, T. Tong, B. Shen and J. Yu, *J. Catal.*, 2018, **361**, 255–266.

211 V. Parey, B. M. Abraham, M. V. Jyothirmai and J. K. Singh, *Catal. Sci. Technol.*, 2022, **12**, 2223–2231.

212 A. D. Handoko, K. H. Khoo, T. L. Tan, H. Jin and Z. W. Seh, *J. Mater. Chem. A*, 2018, **6**, 21885–21890.

213 Y. Sun, R. Yu, J. Sun, D. Legut, J. S. Francisco and R. Zhang, *J. Mater. Chem. A*, 2025, **13**(16), 11703–11716.

214 S. Cao, Y. Liu, Y. Hu, J. Li, C. Yang, Z. Chen, Z. Wang, S. Wei, S. Liu and X. Lu, *J. Colloid Interface Sci.*, 2023, **642**, 273–282.

215 X. Wu, Y. Wang and Z. S. Wu, *iScience*, 2024, **27**, 108906.

216 Y. Zhou, Y. Wang, Y. Wang and X. Li, *Anal. Chem.*, 2020, **92**, 16033–16042.

217 B. Miao, T. Bashir, H. Zhang, T. Ali, S. Raza, D. He, Y. Liu and J. Bai, *Renewable Sustainable Energy Rev.*, 2024, **199**, 114506.

218 E. Rems, Y. J. Hu, Y. Gogotsi and R. Dominko, *Chem. Mater.*, 2024, **36**, 10295–10306.

219 A. Miranda, J. Halim, A. Lorke and M. W. Barsoum, *Mater. Res. Lett.*, 2017, **5**, 322–328.

220 L. Meng, L. K. Yan, F. Viñes and F. Illas, *J. Mater. Chem. A*, 2024, **12**, 7856–7874.

221 Y. Shi, B. Wei, D. Legut, S. Du, J. S. Francisco and R. Zhang, *Adv. Funct. Mater.*, 2022, **32**, 2210218.

222 Y. Wang, R. Du, Z. Li, H. Song, Z. Chao, D. Zu, D. Chong, N. Gao and C. Li, *Ceram. Int.*, 2021, **47**, 28321–28327.

223 M. H. Sliem, K. Kannan, M. R. Maurya, K. Jlassi, K. K. Sadasivuni, B. Kumar and A. M. Abdullah, *Top. Catal.*, 2022, **1**, 1–16.

224 Y. Hao, F. Hu, S. Zhu, Y. Sun, H. Wang, L. Wang, Y. Wang, J. Xue, Y. F. Liao, M. Shao and S. Peng, *Angew. Chem. Int. Ed.*, 2023, **62**, e202304179.

225 K. Kannan, M. H. Sliem, A. M. Abdullah, K. K. Sadasivuni and B. Kumar, *Catalysts*, 2020, **10**, 549.

226 P. K. Jiwanti, A. M. Alfaza, G. T. M. Kadja, S. A. C. Natalya, F. Sagita, Y. Einaga, A. Purwaningsih, I. Amalina and I. N. Rizki, *Energies*, 2023, **16**, 4537.

227 Z. Li, N. H. Attanayake, J. L. Blackburn and E. M. Miller, *Energy Environ. Sci.*, 2021, **14**, 6242–6286.

228 Y. Wang, J. Shui, Y. Jia, H. Zhang, W. Cen, S. Tang and Y. Han, *Chem. Eng. J.*, 2025, **507**, 160716.

229 Z. W. Seh, K. D. Fredrickson, B. Anasori, J. Kibsgaard, A. L. Strickler, M. R. Lukatskaya, Y. Gogotsi, T. F. Jaramillo and A. Vojvodic, *ACS Energy Lett.*, 2016, **1**, 589–594.

230 J. Zhang, Y. Zhao, X. Guo, C. Chen, C. L. Dong, R. S. Liu, C. P. Han, Y. Li, Y. Gogotsi and G. Wang, *Nat. Catal.*, 2018, **1**, 985–992.

231 J. Yu, Y. Zeng, J. Chen, K. Tan and W. Lin, *J. Colloid Interface Sci.*, 2025, **697**, 137961.

232 H.-H. Cao, Z.-H. He, P.-P. Guo, Y. Tian, X. Wang, K. Wang, W. Wang, H. Wang, Y. Yang and Z.-T. Liu, *ChemCatChem*, 2025, **17**, e202401133.

233 W. Wu, H. Bi, Z. Zhang, L. Sun, R. Wei, L. Gao, X. Pan, J. Zhang and G. Xiao, *Colloids Surf., A*, 2023, **657**, 130486.

234 A. Athawale, B. M. Abraham, M. V. Jyothirmai and J. K. Singh, *J. Phys. Chem. C*, 2023, **127**, 24542–24551.

235 B. Miao, T. Bashir, H. Zhang, T. Ali, S. Raza, D. He, Y. Liu and J. Bai, *Renewable Sustainable Energy Rev.*, 2024, **199**, 114506.

236 L. Meng, L. K. Yan, F. Viñes and F. Illas, *J. Mater. Chem. A*, 2023, **11**, 6886–6900.

237 D. D. Kruger, J. J. Delgado, F. J. Recio, S. Goberna-Ferron, A. Primo and H. Garcia, *J. Mater. Chem. A*, 2024, **12**, 25291–25303.

238 X. An and D. Yang, *Nanoscale*, 2025, **17**, 4212–4225.

239 E. J. Jelmy, N. Thomas, D. T. Mathew, J. Louis, N. T. Padmanabhan, V. Kumaravel, H. John and S. C. Pillai, *React. Chem. Eng.*, 2021, **6**, 1701–1738.

240 H. Jin, T. Song, U. Paik and S. Z. Qiao, *Acc. Mater. Res.*, 2021, **2**, 559–573.

241 X. Chia and M. Pumera, *Nat. Catal.*, 2018, **1**, 909–921.

242 S. Xiao, Y. Zheng, X. Wu, M. Zhou, X. Rong, L. Wang, Y. Tang, X. Liu, L. Qiu and C. Cheng, *Small*, 2022, **18**, 2203281.

243 G. Wei, Z. Mao, L. Liu, T. Hao, L. Zhu, S. Xu, X. Wang and S. Tang, *ACS Appl. Mater. Interfaces*, 2024, **16**, 52233–52243.

244 Q. Tang, T. Li, W. Tu, H. Wang, Y. Zhou and Z. Zou, *Adv. Funct. Mater.*, 2024, **34**, 2311609.

245 L. Li, *Comput. Mater. Sci.*, 2016, **124**, 8–14.

246 C. Lu, L. Yang, B. Yan, L. Sun, P. Zhang, W. Zhang, Z. Sun, C. Lu, L. Yang, B. Yan, P. Zhang, W. Zhang, Z. M. Sun and L. Sun, *Adv. Funct. Mater.*, 2020, **30**, 2000852.

247 C. Liu, Y. Bai, W. Li, F. Yang, G. Zhang and H. Pang, *Angew. Chem. Int. Ed.*, 2022, **61**, e202116282.

248 L. Zhou, Q. Tian, X. Shang, Y. Zhao, W. Yao, H. Liu and Q. Xu, *Green Chem.*, 2024, **26**, 1454–1461.

249 F. Yang, D. Deng, X. Pan, Q. Fu and X. Bao, *Nat. Sci. Rev.*, 2015, **2**, 183–201.

250 A. Wang, J. Li and T. Zhang, *Nat. Rev. Chem.*, 2018, **2**, 65–81.

251 L. Zhang, K. Doyle-Davis and X. Sun, *Energy Environ. Sci.*, 2019, **12**, 492–517.

252 X. F. Yang, A. Wang, B. Qiao, J. Li, J. Liu and T. Zhang, *Acc. Chem. Res.*, 2013, **46**, 1740–1748.

253 S. Ding, M. J. Hülsey, J. Pérez-Ramírez and N. Yan, *Joule*, 2019, **3**, 2897–2929.

254 R. Gusmão, M. Veselý and Z. Sofer, *ACS Catal.*, 2020, **10**, 9634–9648.

255 Y. Sun, X. Tan, X. Zhang, Y. Wang, Z. Ju and Q. Kang, *Mater. Lett.*, 2025, **391**, 138467.

256 Y. Lin, F. Yu, L. Li, Y. Li, R. Huang and Y. Wen, *ACS Catal.*, 2024, **14**, 16423–16433.

257 H. Wang, X. Li, Y. Deng, J. Jiang, H. Ma and J. Zou, *Coord. Chem. Rev.*, 2025, **529**, 216462.

258 F. Li, H. Ai, C. Shi, K. H. Lo and H. Pan, *Int. J. Hydrogen Energy*, 2021, **46**, 12886–12896.

259 Y. H. Chen, M. Y. Qi, Y. H. Li, Z. R. Tang, T. Wang, J. Gong and Y. J. Xu, *Cell Rep. Phys. Sci.*, 2021, **2**, 100371.

260 D. Zhao, Z. Chen, W. Yang, S. Liu, X. Zhang, Y. Yu, W. C. Cheong, L. Zheng, F. Ren, G. Ying, X. Cao, D. Wang, Q. Peng, G. Wang and C. Chen, *J. Am. Chem. Soc.*, 2019, **141**, 4086–4093.

261 H. Bao, Y. Qiu, X. Peng, J. Wang, Y. Mi, S. Zhao, X. Liu, Y. Liu, R. Cao, L. Zhuo, J. Ren, J. Sun, J. Luo and X. Sun, *Nat. Commun.*, 2021, **12**, 1–9.

262 Z. Liu, Y. Liu, J. Zhang, T. Cao, Z. Sun, J. Liu and H. Shang, *Nano Res.*, 2024, **17**, 3911–3918.

263 H. Hu, J. Wang, P. Tao, C. Song, W. Shang, T. Deng and J. Wu, *J. Mater. Chem. A*, 2022, **10**, 5835–5849.

264 H. Yang, Q. Lin, C. Zhang, X. Yu, Z. Cheng, G. Li, Q. Hu, X. Ren, Q. Zhang, J. Liu and C. He, *Nat. Commun.*, 2020, **11**, 1–8.

265 N. Li, X. Wang, X. Lu, P. Zhang and W. J. Ong, *Chem. – Eur. J.*, 2021, **27**, 17900–17909.

266 N. Li, J. Peng, Z. Shi, P. Zhang and X. Li, *Chin. J. Catal.*, 2022, **43**, 1906–1917.

267 M. A. U. Din, S. S. A. Shah, M. S. Javed, M. Sohail, A. ur Rehman, M. A. Nazir, M. A. Assiri, T. Najam and N. Cheng, *Chem. Eng. J.*, 2023, **474**, 145700.

268 D. Gao, Y. Zhang, Z. Zhou, F. Cai, X. Zhao, W. Huang, Y. Li, J. Zhu, P. Liu, F. Yang, G. Wang and X. Bao, *J. Am. Chem. Soc.*, 2017, **139**, 5652–5655.

269 S. S. A. Shah, M. Sufyan Javed, T. Najam, C. Molochas, N. A. Khan, M. A. Nazir, M. Xu, P. Tsiakaras and S. J. Bao, *Coord. Chem. Rev.*, 2022, **471**, 214716.

270 Y. Sun, Q. Wang, Z. Geng, Z. Liu and R. Yang, *Chem. Eng. J.*, 2021, **415**, 129044.

271 J. C. Yan, F. M. Wang, S. Yin, J. Zhang, W. Jiang and G. G. Liu, *Rare Met.*, 2025, **44**, 2239–2267.

272 T. S. Bui, E. C. Lovell, R. Daiyan and R. Amal, *Adv. Mater.*, 2023, **35**, 2205814.

273 Z. Cai, Y. Wu, Z. Wu, L. Yin, Z. Weng, Y. Zhong, W. Xu, X. Sun and H. Wang, *ACS Energy Lett.*, 2018, **3**, 2816–2822.

274 L. Yang, J. Du, J. Deng, N. H. M. Sulaiman, X. Feng, C. Liu and X. Zhou, *Small*, 2024, **20**, 2307007.

275 S. Li, H. Chai, L. Zhang, Y. Xu, Y. Jiao and J. Chen, *J. Colloid Interface Sci.*, 2023, **642**, 235–245.

276 Y.-T. Liu, P. Zhang, N. Sun, B. Anasori, Q.-Z. Zhu, H. Liu, Y. Gogotsi, B. Xu, Y. Liu, P. Zhang, N. Sun, Q. Zhu, H. Liu, B. Xu, B. Anasori and Y. Gogotsi, *Adv. Mater.*, 2018, **30**, 1707334.

277 Z. Otgonbayar, C. M. Yoon and W. C. Oh, *Chem. Eng. J.*, 2023, **464**, 142716.

278 J. Y. Kim, W. T. Hong, T. K. C. Phu, S. C. Cho, B. Kim, U. Baeck, H. S. Oh, J. H. Koh, X. Yu, C. H. Choi, J. Park, S. U. Lee, C. H. Chung and J. K. Kim, *Adv. Sci.*, 2024, **11**, 2405154.